UNIVERSITY OF
BIRMINGHAM

Experimental Low-THz Imaging Radar for Automotive Applications

by

Donya Jasteh

A thesis submitted to the University of Birmingham

for the degree of

DOCTOR OF PHILOSOPHY

School of Electronic, Electrical and System Engineering
College of Engineering and Physical Sciences
University of Birmingham
September 2016

Abstract

This thesis reports initial experimental results that provide the foundation for low-THz radar imagery for outdoor scenarios as expected in automotive sensing. The requirements for a low-THz single imaging radar sensor are outlined. The imaging capability of frequency-modulated continuous-wave (FMCW) radar operating at 150 GHz is discussed. A comparison of experimental images of on-road and off- road scenarios made by a 150 GHz FMCW radar and a reference 30 GHz stepped frequency radar is made, and their performance is analysed.

To my wonderful parents

Akram & Jamshid

Acknowledgments

I am really humbled and grateful for all the support I have received during the course of my PhD research and I would like to thank;

First and foremost my supervisors Dr Marina Gashinova and Prof Mike Cherniakov for the opportunity of working on such an interesting project. I would like to thank Marina for inspiring me throughout my PhD and for what I have learned from her. I would like to thank Mike for bringing the Microwave Integrated Systems Laboratory (MISL) together and making it a team.

Dr Edward Hoare for all he has thought me and for his support and encouragement during the write up stage of my thesis.

Mr Alan Yates for his continuous support during my experiments.

My industrial supervisors Mrs Thuy Yung Tran and Mr Nigel Clarke for their advice and support.

The Jaguar Land Lover research department for funding this project.

My fellow PhD students and researchers in the MISL group for their friendship and support; Dr Manuel Crespo, Dr Kalin Kabakchiev, Dr Liam Daniel, Mr Ben willets, Dr Aleksandr Bystrov, Mr Alessandro De Luca, Mr Emidio Merchetti, Dr Ma Hui, Dr Micaela Contu and Mr Sukhjit Puni.

My wonderful parents Akram and Jamshid, for their endless love and for providing me with the most fantastic childhood. I have dedicated this thesis to them.

My brother Sina, who is my best friend.

Last but not least, my loving husband John, for his endless support and encouragement especially during the write up stage of the thesis.

Contents

Abbreviations

2D	Two Dimensional
ACC	Adaptive cruise Control
ADAS	Advanced Driver Assistance Systems
ADC	Analogue to Digital Converter
CW	Continuous Wave
DFT	Discrete Fourier Transform
DSP	Digital Signal Processor
DUT	Device Under Test
EESE	Electronic, Electrical and Systems Engineering
EM	Electromagnetic
FCC	Federal Communications Commission
FFT	Fast Fourier Transform
FIR	Far Infra-Red
FMCW	Frequency Modulated Continuous Wave
ICC	Intelligent cruise Control
IF	Intermediate Frequency
IFFT	Inverse Fast Fourier Transform
ISAR	Inverse Synthetic Aperture Radar
InSAR	Interferometric Synthetic Aperture Radar
LIDAR	Light Detection and Ranging
LLR	Long Range Radar
LOS	Line of Sight
MDS	Minimum detectable signal

MISL	Microwave Integrated Systems Laboratory
MRR	Medium Range Radar
MTI	moving target indication
MMIC	Monolithic Microwave Integrated Circuit
PBM	Physical Beam Mapping
PEC	Perfect Electric Conductor
RADAR	Radio Detection and Ranging
RCS	Radar Cross Section
RF	Radio Frequency
Rx	Receive
SAR	Synthetic Aperture Radar
SCR	Signal to Clutter Ratio
SFW	Stepped Frequency Waveform
SLAR	Side-Looking Airborne Radar
SNR	Signal to Noise Ratio
SRR	Short Range Radar
STC	Sensitivity Time Control
TOF	Time Of Flight
Tx	Transmit
UDP	User Datagram Protocol
VNA	Vector Network Analyzer

1. Introduction

1.1 Motivation and background

Autonomous driving is one of the hot topics of the automotive industry at the moment. Most automotive manufacturers and suppliers are currently focusing their research and development in this area, and it is leading to more mature levels of autonomy in cars every year. In the near future, cars will be highly automated [1].

In order to fulfil the requirements of a highly automated car, the intelligent vehicle should be able to "sense" the environment. The more useful data that it can gather, the more it would allow it to make better decisions in different on- and off-road scenarios. Automotive remote sensing sensors are currently using a wide range of technologies. The data collection takes place through different types of sensors on the vehicles such as radars, stereo video cameras, mono video cameras, ultrasonic sensors, LIDARs (Light Detection and Ranging) and thermographic cameras. As the level of autonomy increases, more driver tasks are transferred to the vehicle. Robust, reliable systems are thus required. A fusion of different sensors can improve the system performance and robustness. However, new types of sensor technology that can offer a different type of data set should also be explored. This study proposes a new type of radar technology for automotive applications.

The images produced by LIDAR and stereo camera contain a vast amount of information about the environment that can be used for object detection and feature extraction. At present, many of the safety critical features on vehicles rely on a stereo video camera to detect and classify objects. However, the performance of optical systems (camera/LIDAR) may be

hampered by rain, smoke, fog, snow, spray and etc. It would fail to deliver a usable image under severe weather and lighting conditions. This is because the light is scattered by small particles, causing significant attenuation of the transmitted signal whilst it is travelling through the volume of scatterers. Microwave frequency waves (radars) overcomes this problem because they are able to penetrate through the volume of scattering particles without significant attenuation, with the caveat that the microwave signal wavelength is much larger than the effective size of the individual scatterers. This means that radar systems are robust to such conditions. Moreover, radars fundamentally offer the following advantages in comparison to other sensor technologies:

1. Direct measurement of relative velocities
2. The detection performance is not influenced by lighting conditions
3. The sensors can be mounted behind radar transparent materials (e.g. plastic vehicle bumper) with low reduction of sensitivity if needed for design aspects.

Therefore, this study proposes to use radars to make images in road environments. Fig 1.1 shows radar images from a road scenario with typical road features and objects such as vehicles, kerbs and trees. A Celsius Tech radar operating at 77 GHz is used to demonstrate the imaging capabilities of conventional Adaptive Cruise Control (ACC) automotive radars [2]. Fig.1.1 (b) and (c) shows the resulting images using the Celsius Tech radar operating at 77 GHz with the sweep bandwidth of 280 MHz which results in 0.5 m range resolution. The antenna is a mechanically scanning antenna with an azimuth beamwidth of 3°. It is evident that the range resolution is not sufficient for medium range high resolution imaging. In order to achieve a high range resolution, wide bandwidths are required, though at standard automotive radar frequencies, the availability of wide bandwidths is limited.

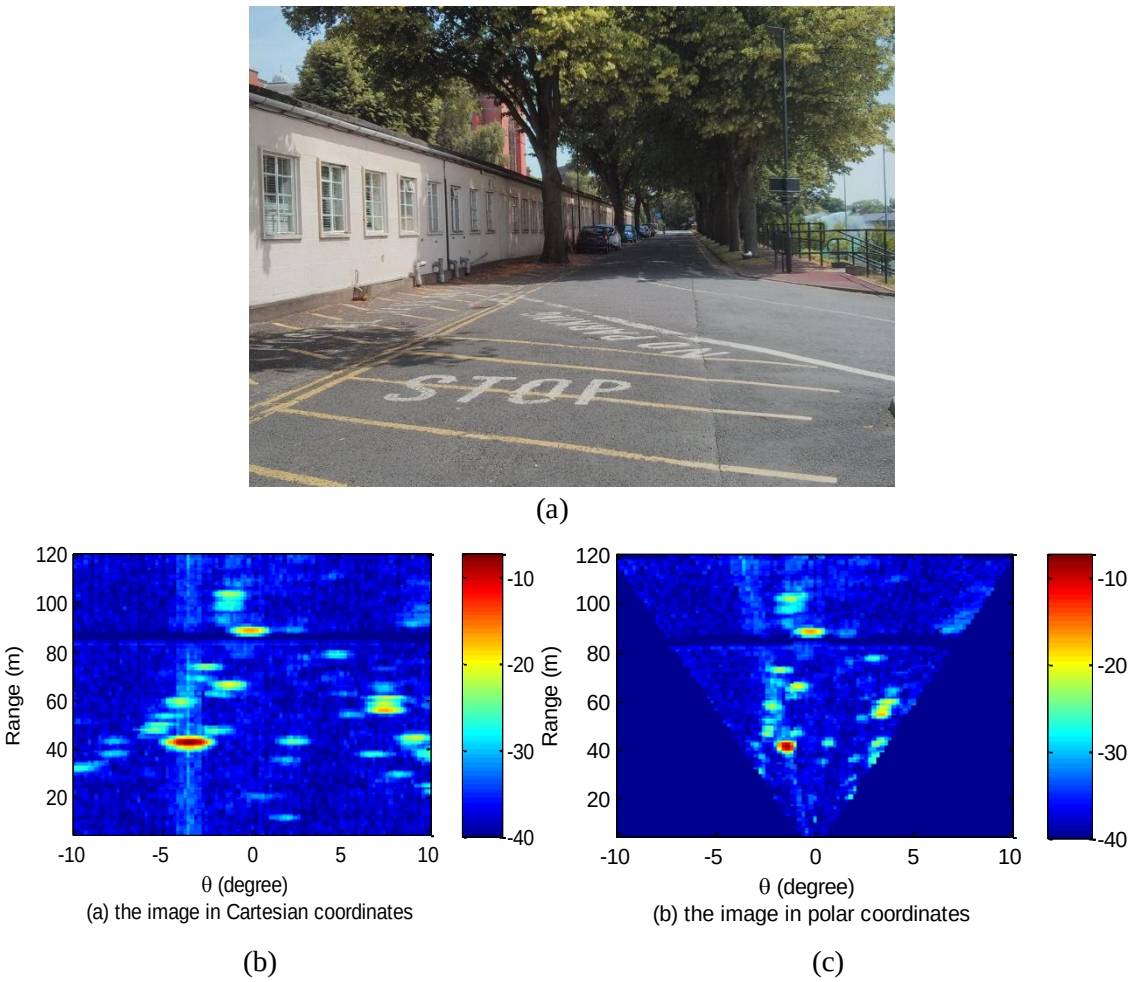

Figure 1.1 (a) Road Scenario with potential features to be detected such as trees, vehicles, kerb and etc. (b) Image of the road scenario of (a) in Cartesian coordinates using a Frequency Modulated Continuous Wave (FMCW) radar operating at 77 GHz (c) Image of the road scenario of (a) in polar coordinates [2].

The proposed solution is a radar system operating at low-THz frequencies with high resolution imaging capabilities. High resolution imaging radar is proposed as a complementary solution to stereo video cameras, as the backbone of remote sensing for autonomous driving. The information-rich radar images can be interpreted for on-road and off-road object and feature detection for further classification. The fusion of radar and camera image data increases the robustness of the systems and reliability of the provided data. This leads to a higher performance of the systems based on these sensors. This is the subject of the current research and development work taking place at the University of Birmingham [3].

In this PhD study, "low-THz" is specified as the portion of the electromagnetic spectrum from 0.1 to 1 THz. The performance of the system operating in the low-THz frequency band may be compared to LIDAR and FIR (Far Infra-Red) spectra [4]. There are several potential advantages of using low-THz frequency bands for automotive applications, as opposed to the lower frequency microwave and mm-wave bands, and on the other side of the spectrum, the infra-red and optical band (see Fig 1.2) [4]. Low-THz frequency band provides:

- Feasibility of compact apertures for a given azimuth beamwidth (i.e. angular resolution). The smaller the wavelength, the smaller the aperture sizes for a given azimuth resolution (see equation (5.14) in section 5.6.3).
- Waveforms with wavelengths of the order of 1 mm and less are more sensitive to the surface roughness and texture of objects than waveforms operating in microwave frequencies ($\lambda \approx 10$ mm). Surfaces which appear smooth to conventional automotive waveforms would be rough in comparison to low-THz wavelengths resulting in larger backscattering from these surfaces. This would provide additional data on the images for the detection and classification of objects and surfaces.
- In addition to optical imaging, the radar can potentially provide additional classification features, such as depth of shadow, spectral patterns, and resonances in the backscatter signal that will imbue the image with texture, object curvature, and motion parameter estimation. Enhanced resolution of the low-THz imagery allows exploitation of the vast legacy of optical image processing algorithms [2].
- There is an additional advantage of using the portion of the spectrum which is not in use or licensed for other applications; the hardware technology at these frequencies allows wider bandwidths to become available. Wider bandwidths enable high range resolution measurements.

The idea is to develop a sensor technology with capabilities that are a trade-off between microwave frequencies and optical frequencies (See Fig. 1.2). An optimum operating frequency should be found with wavelengths that are small enough to provide a fine resolution and texture sensitive images, but large enough to see through scatterers in the air caused by precipitation and obscurants. The characteristics of low-THz signal attenuation in road environments is the subject of current research [5].Thus the optimal microwave frequency range must be found in order to simultaneously provide relatively high resolution, small attenuation losses by using a sensor with a compact size.

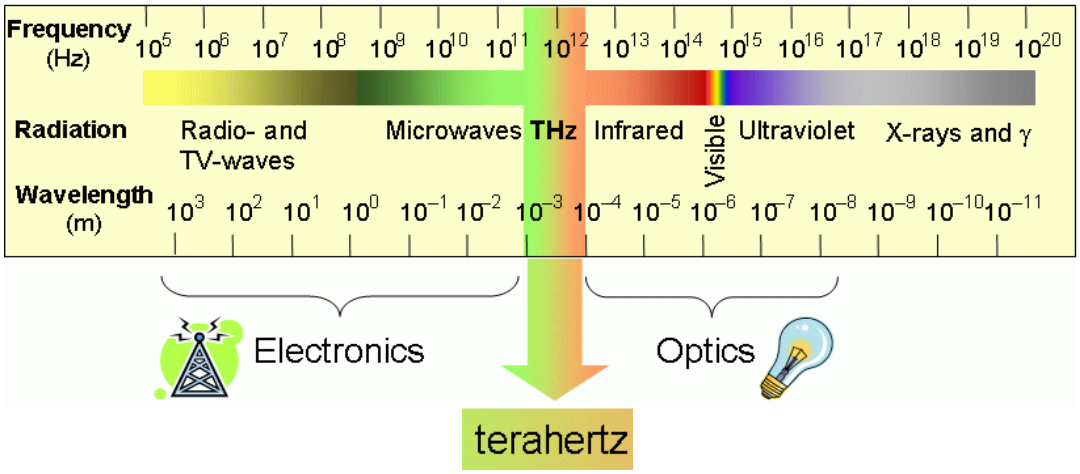

Figure 1.2: The terahertz frequency band with capabilities which is a trade-off between microwaves and infrared and optical frequencies [6].

Table 1.1 compares the characteristics of stereo video camera, Medium Range Radar (MRR) used for Adaptive Cruise Control (ACC) and the proposed imaging radar operating at Low-THz frequencies. The MRR and stereo video camera are considered as they are the existing sensor technologies used for forward sensing.

Table 1.1: A summary of comparison of characteristics of the medium range radar used for Adaptive Cruise Control, the proposed imaging radar operating at Low-THz frequencies and of stereo video camera [7].

Sensor Technology	**Medium Range Radar**	**Radar (Low THz imaging)**	**Stereo video camera [8]**
Frequency (Bandwidth)	77 GHz (~300 kHz) [9]	150 GHz-670 GHz (4 GHz -30 GHz)	430-790 THz (380-750 nm)
Maximum Operational Range	150 m	~100 m	~ 50 m
Range resolution	Poor (0.5 m)	High (0.03 m-0.005 m)	poor (range dependent)
Azimuth resolution (for a given aperture size)	Poor	High (achievable but challenging)	High
Direct Velocity measurement	Ideally suited	Ideally suited	Not possible (only range rate measurement)
Texture sensitivity	Not suited	Ideally suited	Possible (dependent on lighting)
Operation in rain, fog, snow, smoke and dust	Good performance	Good performance	Disrupted performance
Dirt on sensor	Operational (within limits)	Operational (within limits)	Non-operational
Sensitivity to lighting conditions	Not sensitive	No sensitive	Performance affected
Highlighted Advantages	Robustness to different weather and lighting conditions and dirt on sensor radome	A. Texture sensitivity due to small wavelengths B. High range resolution due to wide available bandwidth	A. Relatively simple hardware B. High resolution images
Limitations	Not intended for imaging	Attenuation higher than conventional automotive radars in precipitation	A. Not robust to severe weather and lighting conditions, dirt and dust. B. not suitable for accurate velocity and range measurements at long range [10]
Technology maturity	Available	In development (maturing)	Available

1.2 Aims and Objectives

The objective of this study is to explore the feasibility of producing forward looking radar sensors operating at low-THz frequencies capable of high-resolution imaging in automotive environments for medium range applications. The medium range is specified according to conventional automotive radar range definition (Table 2.1). This thesis reports initial experimental results that provide the foundation for low-THz radar imagery for outdoor scenarios as expected in automotive sensing. The imaging capability of Frequency Modulated Continuous Wave (FMCW) radar operating at 150 GHz is discussed. A comparison of experimental images of on-road and off-road scenarios made by a 150 GHz FMCW radar and a reference 30 GHz stepped frequency radar is made, and their performance is analysed [4].

In this study, the 150 GHz operating frequency at the lower end of low-THz frequencies is explored as the first step in defining the feasibility of the proposed solution. The next operating frequencies of 300 GHz and 670 GHz are the subject of current research within the THz systems laboratory at the University of Birmingham [5, 11].

The resulting high resolution images may be processed for object and road feature detection and classification. Enhanced resolution of low-THz imagery allows exploitation of the vast legacy of optical image processing algorithms for feature extraction [2]. The objects to be imaged consist of road objects and features such as kerbs, lamp posts, road humps, trees, road markings and etc. Off-road obstructions and features such as potholes, puddles, ditches and rocks. Other potential targets are dynamic road actors such as vehicles, bicycles, pedestrians and animals, which however are not the subject of this study.

1.3 Methodology

1.3.1 High resolution imaging

Physical beam mapping is the imaging method used in this study. In this method, a two dimensional (Range, Azimuth) intensity image-map of a scene is generated by producing range profiles over a series of frequency modulated pulses. The profiles are then placed next to one another in the order they were collected. This is realised by using forward looking radars operating at 150 GHz as the first step in exploring low-THz frequencies. The radar in this case consists of a mechanically scanning antenna so that the antenna illuminates a slightly different portion of the scene from scan to scan. Electronically scanning or alternatively multi- beam array antennas can also be used.

In order to verify the methodology, a radar system operating at 7.5 GHz was built from available instruments and components in house. The initial images were formed using this radar, and this is discussed in chapter 3. The methodology was then transferred to a 30 GHz operating frequency with the intention of benchmarking the proposed solution against the conventional microwave frequencies. This radar is discussed in chapter 4 and the resulting images are compared to the 150 GHz radar images in chapter 6.

1.3.2 Fundamental system requirements for high resolution imaging radar

Top level requirements that should be met in designing a scanning high resolution imaging radar system for medium range automotive applications are: 1. compact antennas with narrow beam in azimuth plane to provide high angular resolution; 2. the ability to scan the area to be imaged; and 3. wide operational bandwidth to deliver fine range resolution [4]. While the latter is an inherent feature of low-THz devices with up-converted frequencies, effort is

needed in the antenna design to satisfy desired performance requirements [12]. The antennas are required to have a wide E-plane (elevation) beam, Θ_E (notations are shown in Fig. 1.3), to provide the required wide illuminated footprint along the path for medium range applications and a narrow H-plane (azimuth) beam, Θ_H, to provide a fine angular resolution. The intended range of operation for the radar discussed in this study is defined from 4 m to 100 m medium range) to the transceiver. Fig.1.3 shows the monostatic radar configuration and the antenna footprint on the ground [4].

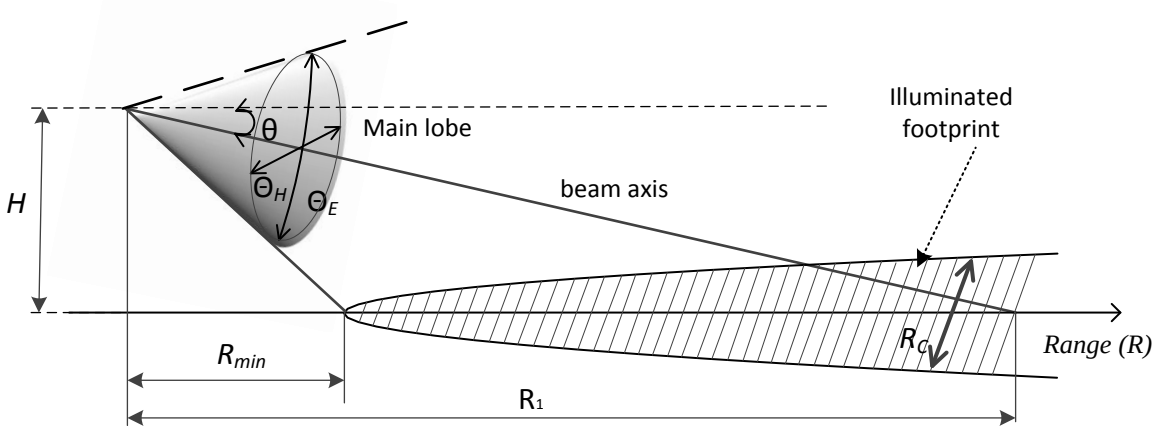

Figure 1.3: Single beam monostatic configuration for imaging radar. H is the antenna elevation; Θ_E and Θ_H are beamwidths of antenna pattern in E-plane and H- plane accordingly. R_1 is the distance to the centre of the footprint, defined by beam axis direction; R_c is the linear angular resolution at the distance R.

In order to deliver fine range resolution, a wide operational bandwidth is required. In this study, the wide bandwidth is achieved by using a Stepped Frequency Waveform (discussed in chapters 3 and 4) and a FMCW waveform (discussed in chapters 5 and 6).

1.3.3 Basic steps of imaging

Fig.1.4 shows the three basic steps in forming a radar image map. The first step is to collect data, which is achieved with the prototype radar systems operating at 7.5 GHz, 30 GHz and 150 GHz. The second stage is the processing of the obtained data in order to form a 2D image map. This step is discussed in chapter 3. In this study, the signals processing and image formation has been done using MATLAB. The third stage is image interpretation which

involves processing the images for feature and object extraction and classification. The first and second steps are explored in this thesis. Image interpretation has only been done visually. This is a topic of further research. A variety of image processing methods and algorithms that are reported in literature can be explored [13-15].

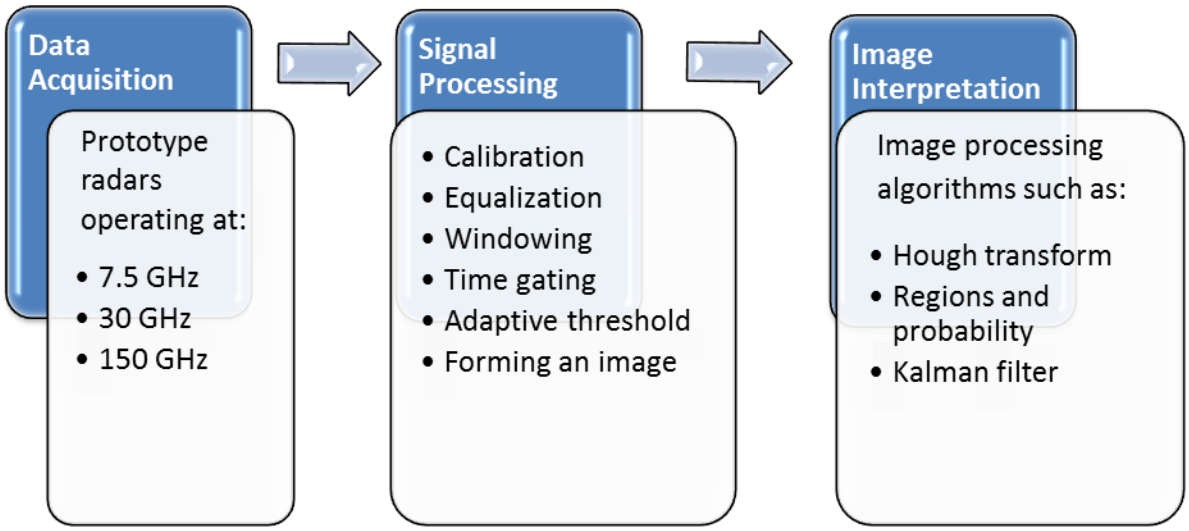

Figure 1.4: The three basic stages of imaging

Fig. 1.5 is a preliminarily impression of the concept of the proposed system. It shows the drawing of a vehicle with antennas mounted at the front. The multi-beam or scanning antenna is sweeping the area in front of the moving vehicle. The collected data is processed nearly real-time (very high speed) in order to produce a 2D [azimuth, range] (or even 3D) image map of the scene. The image is used for road object and feature extraction. The image used on the screen of Fig. 1.5 is a LIDAR produced image and is only used to convey the idea.

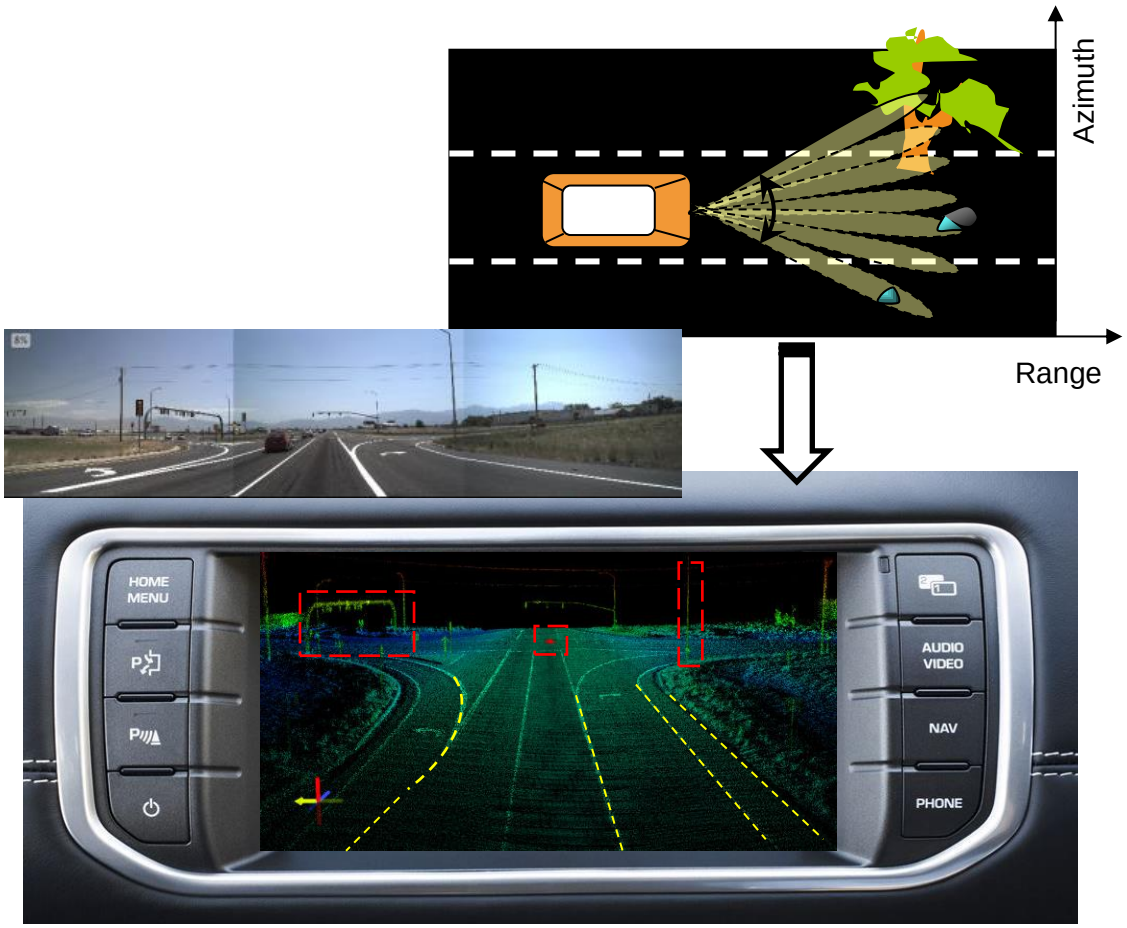

Figure 1.5: Preliminary presentation of the system concept

1.4 Thesis Outline

Chapter 2 is a brief review of the reported literature in four broad topics. The topics are as follows: 1. Basic relevant principles of radar system. 2. An overview of existing imaging radar technologies. 3. THz frequencies and a brief review of the applications to date. 4. The automotive radar, development history, trends and the future directions are discussed in this chapter.

Chapter 3 discusses the method of *Physical Beam Mapping* for producing a two dimensional image map using a forward looking radar system. The three stages of data acquisition signal processing and image formation are explained in this chapter. The waveform used for

achieving high range resolution is the Stepped Frequency Waveform (SFW). To exercise the methodology, measurements have been taken using a prototype radar system operating at 7.5 GHz.

Chapter 4 discusses a prototype radar system assembled using in house available components and instruments operating at 30 GHz. A radar system operating at microwave frequencies is developed in order to create images which will be used as a benchmark for the 150 GHz radar imaging.

Chapter 5 provides an overview of the laboratory prototype radar system operating at 150 GHz. Parameters affecting radar design are reviewed through the radar equation. FMCW waveform generation and an overall block diagram of the radar system are reviewed. Finally, a specification table for the radar system under study is presented.

Chapter 6: demonstrates the imaging results of the low-THz FMCW radar discussed in chapter 5 for outdoor scenarios which are expected in automotive environments. The focus is on the initial interpretation of radar images by analysing features of imaged environments and comparing them with microwave radar images. Images of the specific on-road and off-road scenarios have been made at 150 GHz. They are compared to the radar images made by the stepped frequency radar operating at microwave frequencies (30 GHz) introduced in chapter 4. The images in this chapter are presented without any significant image processing [4].

In **Chapter 7** conclusions are drawn and further research topics are discussed.

2. Literature Review

Overview-*This chapter consists of four main sections. First the basic relevant principles of radar systems are reviewed. The second section is an overview of imaging radar. In the third section, the THz frequency range is discussed. It also includes a brief review of the applications to date. Finally the automotive radar, development history, trends and future directions are discussed.*

2.1 Principles of radar system

2.1.1 About Radar

The radar, as known today, was developed during World War II. However, the basic principles of radio detectionwere by Hertz in 1886 ; he demonstrated that the radio waves could be reflected by metallic and dielectric objects [16]. In April 1904, German engineer Christian Huelsmeyer invented a device called Telemobiloscope using radio waves for detecting the presence of distant objects [17].

A radar in its simplest form consists of a transmitting antenna, emitting electromagnetic radiation generated by an oscillator; a receiving antenna and a receiver module to detect the energy [16]. Only part of the transmitted signal is intercepted by the target and is reradiated in all directions. The energy reradiated towards the receiver antenna would be processed in order to detect the presence of the target, extract the target's location and to gather other information about the target according to the radar application [16].

As is evident by the name Radio Detection and Ranging (Radar) used from early days, detection and location of the targets are the most important uses of radar [18]. No other type of sensor or device is able to measure the range to the remote targets in adverse weather and

poor lighting conditions. Radar can see through conditions impervious to the naked human eye, such as darkness, haze, fog, rain and snow [16].

2.1.2 Range and Doppler measurements

The distance to the target (range) is determined by measuring the time it takes for the signal to travel to the target and back. The angular position (azimuth position) of the target can be determined by the direction of the arrival of the reflected wave front. This can be measured by using narrow beam antennas in azimuth.

In the case of a moving target and/or radar, the relative (radial) velocity between the target and the radar can be determined by measuring the shift in the carrier frequency of the reflected wave (Doppler effect). This also could be used to distinguish moving targets from stationary ones [16]. This study is dedicated to the investigation of imaging capabilities of low-THz radar and at the initial stage of the research only stationary objects are considered.

2.1.3 Waveform choice for range measurements

As mentioned earlier, the target's range is determined by measuring the time taken by the transmitted signal to travel to and from the target. Accurate range measurements can be achieved by having a sharp or distinct timing mark in order to mark the time of transmission and the time of return. Achieving a very sharp timing mark would require a broad transmitted bandwidth. The bandwidth of a Continuous Waveform (CW) could be increased by the application of modulation (amplitude, frequency or phase)[19].

One common waveform modulation for the radar is amplitude modulation. "Pulsed radar" is a special case of amplitude modulation where it transmits a narrow rectangular shape pulse modulating a sinewave carrier. The narrower the pulse, the wider the bandwidth and therefore the more accurate the range measurement would be [20]. CW transmissions use low

continuous power whereas pulsed radars employ high peak powers for short periods of time in order to achieve similar detection performance. The average power over time on the target determines the detection characteristics of the radar system. In order to achieve the same performance, pulsed radars are more expensive in comparison to those using CW waveforms [20]. Pulsed radars would be typically used for applications (such as airborne) that do not need to be mass produced in high volumes and therefore the cost per item would not be an important factor.

Frequency Modulated Continuous Waveform (FMCW)

Range measurement is also possible by frequency modulating the carrier, i.e. using a FMCW signal; which is one of the most popular techniques to broaden the spectrum. The most common method of frequency modulation is linear modulation. In contrast to pulsed radar, it can be produced with solid-state transmitters which define the low cost and high reliability of systems [20]. The transmit power is lower than that of pulsed radars yet demonstrating a similar performance, as power is spread uniformly over a nearly rectangular spectrum. The timing mark is achieved by the changing transmitted frequency over a limited time. In linear modulation, this frequency could linearly increase (Up-chirp) or it could linearly decrease (down-chirp) within a given time interval [21]. The principles of FMCW radar will be discussed in chapter 5 (section 5.5), where the 150 GHz FMCW radar is introduced and design parameters are discussed.

Problems with FMCW

1. In FMCW radars, transmitting and receiving takes place simultaneously. Therefore the leakage from transmitter to receiver could be an issue and it could reduce the dynamic range of the receiver [20]. In the 150 GHz radar introduced in this thesis, the separate transmit and receive antennas are used to enhance the isolation between

them. Clutter cancelation techniques and signal processing methods are used to cancel the leakage power in order to achieve a better performance. This will be discussed further in chapter 3 [20].

2. Another problem with FMCW signals is the range-Doppler coupling. In the case of few moving targets at different ranges, it is tricky to separate the Doppler shift from the beat (ranging) frequency [20]. However, the moving targets are not the concern in this study and this issue is not discussed further.

2.1.4 Mechanisms of propagation

Reflection, diffraction, and scattering are the three basic propagation mechanisms which influence propagation in a radar system [22]. The transmitted and received Electromagnetic (EM) waves interact with matter such as radar's antenna, the atmosphere and, with the target. Reflection is defined with regards to the target. The reflected power back towards the radar receiver is the fundamental principle that makes radar possible. Therefore, it is going to be defined further on in this chapter [23].

2.1.4.1 Diffraction

According to Skolnik [18]: "In free space, EM waves travel in a straight line. In the Earth's atmosphere, EM waves can propagate beyond the geometrical horizon (straight line) due to *diffraction*. Radar waves are diffracted around the curved earth in the same manner that light is diffracted by a straight edge." Diffraction occurs when the EM waves propagate through an aperture or around the edge of an object. Diffraction also explains penetrating of the EM waves in the shadow region behind an opaque object [23].

The amount of diffraction depends on the size and geometry of the objects relative to the wavelength. The EM wave spreads around objects whose size is comparable to the wavelength and bends around the edges of electrically large objects. Therefore for a given

size of object, diffraction is more significant at lower frequencies (larger wavelengths). Stimson et al. [19] describe this with an example; radio broadcast stations (operating at wavelengths of a few hundred metres) can be heard in the shadows of buildings and mountains, whereas TV stations operating at wavelengths of only a few metres cannot. Diffraction depends on the amplitude, phase and polarization of the incident wave at the point of diffraction [22, 23].

It should be mentioned that at the frequencies of 30 GHz and 150 GHz, discussed in this thesis the objects of interest are electrically much larger than the wavelength and therefore diffraction effects are not significant. Therefore, the near optical shadows from the objects will be observed on the images, which can deliver information about the object's heights. This will be demonstrated in chapter 6 imaging results.

2.1.4.2 Reflection

When transmitted EM waves propagating from one medium (consider air) strikes another medium or surface (consider target), it induces an electric charge on the surface, therefore that surface reradiates the EM wave. The re-radiation of the EM wave from the surface of a medium is commonly called reflection of the incident wave [23].

EM waves are partially transmitted through the objects and partially absorbed depending on the electrical properties of the medium or object. If the matter is a conductor, the electric charge is free to move on the surface of the object, therefore all the EM wave energy is reradiated. If the plane wave strikes a dielectric object, part of the energy is transmitted through the object, part of it would be absorbed and transformed to heat and partially it would be reflected back [22, 23]. The *Fresnel reflection coefficient* (Γ) relates the electric field intensity of the transmitted and reflected waves at the target to that of the incident wave in the

medium of the origin (for instance air). The reflection coefficient is a function of the material properties, and it depends on the frequency, polarization and angle of incidence [22].

Reflection: Specular and diffused scattering on the object surface

The power of surface scattering depends on the roughness of the surface relative to the wavelength of the incident wave and the dielectric constant of the material from which scattering occurs [24].

Roughness in this case is defined as the variation of the surface height. According to Richards et al [23]; it is usually quantified by the standard deviation of the surface height. From a smooth surface ($\lambda >>$ roughness) the reflection is mirror like and it is called a *specular scattering*. In such surfaces, the angle of incidence is equal to angle of reflection (see Fig. 2.1 (a)). Usually, scattering from human-made objects, calm water bodies and very smooth soil surfaces is specular [24]. On the other hand, if the surface is rough ($\lambda <<$ roughness), the incident wave is scattered in all directions and it is called *diffuse scattering*. Generally speaking, scattering from natural surfaces and targets especially at higher frequencies (shorter wavelengths) is mostly diffuse. The Rayleigh criterion [23] could be used to describe the surface roughness. In equation (2.1) the critical height (h_c) of surface irregularities is defined for a given incident angle of (θ_i), where λ is the wavelength of the incident wave.

$$h_c = \frac{\lambda}{8\sin\theta_i} \tag{2.1}$$

A surface is considered smooth if its minimum to maximum protuberance h is less than h_c, otherwise it is considered rough [22]. However, for an arbitrary object, both specular and diffuse scattering should be taken into account [23]. The Specular and diffuse scattering will be further discussed in chapter 6.

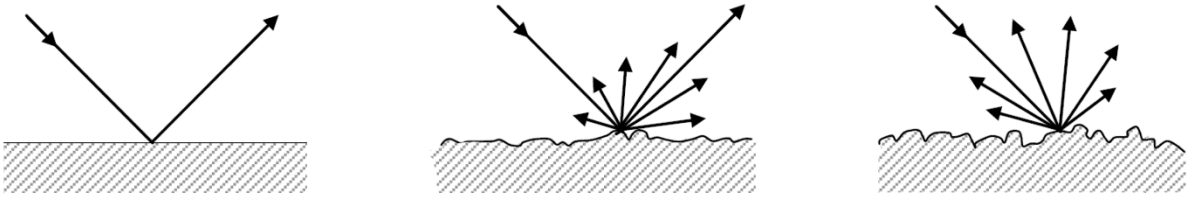

(a) Smooth (b) Slightly rough (c) Very rough

Figure 2.1: Diffused surface scattering increases as roughness increases. (a) specular scattering (b) specular and diffused scattering (c) Strong diffused scattering [24]

Difference between reflection and scattering

It is worth nothing the difference between reflection and scattering as the terms seem to have a very close meaning. According to Rappaport [22], reflection occurs when propagating EM waves impinge upon an object which has very large dimensions relative to the wavelength. The scattering occurs when EM waves travel through a matter which consists of objects that are small relative to the wavelength, and the number of these objects per unit volume is large [22].

2.1.5 Radar Cross Section (RCS)

There is a factor that defines the detectability of a target by arbitrary radar or, in the other words, *visibility* of a target to the radar [16]. This is called the Radar Cross Section (RCS) of a target. "RCS which is also called as echo area, quantifies the scattering phenomenology at the target. RCS that is defined as a far-field parameter, characterises the target rather than the effects of transmitter power, receiver sensitivity and the distance or location between the target, transmitter and receiver" [23] .

The RCS of an object could be described as a comparison of the reflected signal power from an arbitrary target to the received signal reflected from a sphere with a projected area of one square metre (i.e. diameter of about 112 cm) [19]. A sphere is usually used as a calibration target in field experiments or laboratory measurements since the orientation or positioning of

the sphere will not affect radar reflection intensity measurements [25]. This will be discussed further in chapter 3.

There are three basic mechanisms that determine the value of RCS, σ, of a target: 1. *Geometric Cross section* which is the cross sectional silhouette area of the target as seen by radar. This area determines the intercepted power by the target ($Pd_{Intercepted}$) which is defined using equation (2.2) [19]. The size and shape of the target relative to the wavelength and the orientation of it towards the transmitter and receiver define this parameter [19].

$$Pd_{Intercepted} = A \times Pd_{Incident} \tag{2.2}$$

where $Pd_{Incident}$ is the power density of the wave's incident on the target and A is the area.

2. *Reflectivity* is defined as the portion of the intercepted power by the target that is reradiated towards the radar. The reflected power is equal to the intercepted power minus the power absorbed by the target. The more absorbent the surface of a target to the EM waves at the transmitted frequency, the less reflective it is and therefore the smaller the RCS will be [19].

3. *Directivity* is the ratio of the power scattered back, $P_{backscatter}$, in the radar's direction to the isotropic power scattering in all directions, $P_{isotropic}$. This is defined suing equation (2.3).

$$Directivity = \frac{P_{backscatter}}{P_{isotropic}} \tag{2.3}$$

It could be concluded that the visibility of a target to the radar, or its' RCS, depends on the geometry, material properties and shape of the target with regards to the radar point of view. It also depends on other factors such as the position of the transmitter and the receiver relative to the radar, frequency (wavelength) and polarization [23]. The RCS could be defined in a monostatic or bistatic configuration.

Optical, Mie and Rayleigh scattering regions

Scattering mechanisms depends on the object (scattering body) size relative to the wavelength λ. At lower frequencies, when the wavelength is much larger than the object dimension, the scattering is called Rayleigh scattering [16]. In the case where the incident wavelength is comparable to the target size, the phase of the incident wave changes significantly over the length of the scattering body. This region is called resonant or Mie region. The resonant region is normally taken to be the range of wavelengths such that the target effective size varies between λ and 10λ [16]. The first two mechanisms are not the concern of this study. The third, optical region is applicable to the case of this study. For optical scattering the wavelength is much smaller than the target size, i.e. the electrical dimension of the object is larger than 10λ, so that the surface waves effects are insignificant [23].

RCS of a sphere

Fig. 2.2 shows the three scattering regions which are typically calculated for the RCS of a sphere. In the optical region (in farfield), the RCS of a sphere is independent of frequency. In Fig. 2.2, the RCS (σ) has been normalised to the projected area πr^2 (r is the radius) of the sphere, plotted as a function of sphere circumference normalised to wavelength $\left(ka = \frac{2\pi r}{\lambda} \right)$.

When the wavelength is between 1 and 10 times smaller than the sphere circumference, the RCS will be oscillatory due to constructive and destructive interference of specular backscattering and the surface creeping waves. Creeping waves are tangential to a smooth surface and trail the shadow area of the sphere. When the wavelength is much smaller than the sphere's size, the creeping waves are significant, the oscillatory behaviour decays and the specular reflection would be prominent [25]. In the optical region, the RCS is defined only by

the projected area of the sphere ($\sigma=\pi r^2$) and is not frequency dependent [23, 25]. In the case of the objects considered in this study, the RCS is defined in the optical region.

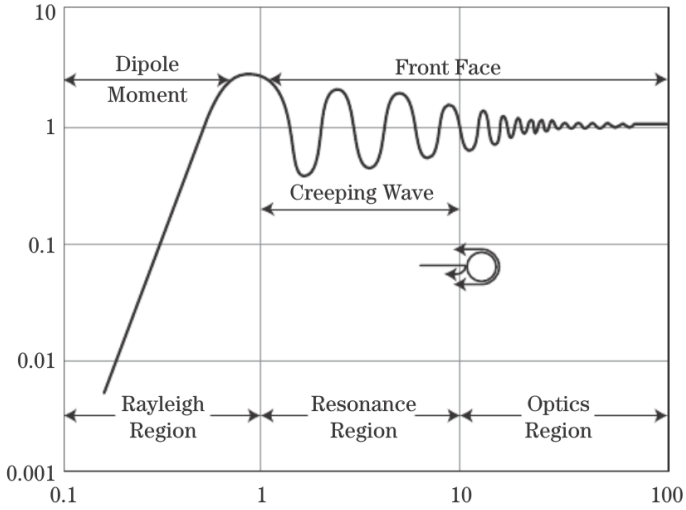

$$ka = \frac{2\pi r}{\lambda}$$

Figure 2.2: Sphere scattering in Rayleigh, resonance, and optical regions [23]

When an object is illuminated by EM waves, it acts like an antenna. Parameters that are defined for antennas may be defined for the target as a secondary antenna in a similar manner: the directivity, far field and near field region etc. are defined for the target as well. Typical values of RCS could vary from 10^{-5} m^2 for insects to 10^{+6} m^2 for large ships [26]. Because of the large dynamic range, a logarithmic power scale is normally used to represent the RCS with reference value of 1 m^2 [23], so that -50 dBm^2 and 60 dBm^2 is used respectively for the above example.

RCS Prediction methods

As a result of the complexities associated with the exact RCS calculation, approximation is the acceptable solution in most cases. The majority of the approximate methods are valid in the optical region, and each has its own strengths and limitations [27]. Most approximate methods can predict RCS within a few dB of the true values. Approximate methods are

usually the main source for estimating RCS of complex and extended targets as well as simple objects. The experimental results are often used to validate the approximations [25, 27]. In this thesis, RCS of a Perfect Electric Conductor (PEC) sphere is simulated using CST Microwave Studio. Approximated RCS of a PEC rectangular flat plate is presented in chapter 6.

In most RCS approximation techniques, the geometrical and directivity aspect of the RCS is considered through the target size, orientation towards the transmitter and receiver and polarization. However, in most cases they are approximated for the perfectly conducting material (PEC). The reflectivity aspect of the RCS which is dictated by material is not usually considered in approximations.

2.2 Imaging radar

2.2.1 Introduction

Most of the literature reporting on imaging radar is focused on active imaging or remote sensing of Earth surfaces using the Synthetic Aperture Radar (SAR) technique. This is to such an extent that the term *remote sensing* or *radar imaging* is automatically associated with SAR imaging. A great deal of the literature on imaging also consists of the very short range medical or airport security imaging using different sensor technologies. The sensors used for such applications consist of ultrasonic, X-ray and recently reported THz frequencies [28].

The term “image” or “imaging” used in this thesis is neither associated with SAR imaging nor very short range medical imaging. In fact this study is concerned with introducing new medium range imaging for applications intended to deliver situational awareness in outdoor environments, such as road scenarios. The imaging method used in this study is called *Physical Beam Mapping* (PBM) and it is going to be discussed in chapter 3, section 3.1. This

basic imaging method is investigated as a proof of concept and other imaging techniques can be used later on to achieve higher resolution.

2.2.2 Image resolution: Angular and Range resolution

The word "resolution" is defined as the smallest interval measurable, or the degree of detail recognisable in an image. The resolution of radar is the minimum distance at which the radar is able to distinguish two targets separately.

Imaging is a broad term that refers to several methods for obtaining detailed information on an individual object or scene. The imaging process consists of two steps: 1. developing a resolution profile of the target in range, and 2. developing a azimuth or cross-range profile of the target [23]. A third dimension can also be considered, in the case of three dimensional imaging. The range resolution is defined by the bandwidth of the transmitted signal. The range resolution is defined using equation (2.4):

$$\Delta R = \frac{c}{2\Delta f} \tag{2.4}$$

where c is the velocity of light in vacuum and Δf is the sweep bandwidth. The range resolution of a radar image could be increased by widening the bandwidth by waveform modulation [29]. This was mentioned earlier in the FMCW waveform section (2.1.3). The finer the range resolution, the more accurate the range measurements will be.

The azimuth beamwidth of the antenna dictates the achievable resolution in azimuth. It should be considered that the azimuthal footprint of the beam on the ground is proportional to range ; therefore the azimuth resolution gets worse as range increases [23] [29]. For a range R and a 3-dB azimuth beamwidth θ_{3dB} (in radians), the azimuth resolution ΔCR is approximated using equation (2.5).

$$\Delta CR \approx R\theta_{3\text{dB}} \tag{2.5}$$

Narrower antenna beamwidths deliver finer resolutions. However, for a given wavelength, in order to achieve a narrow beamwidth, a large antenna aperture is required. For an antenna with the aperture of length *D,* operating at a wavelength λ, an approximate expression for the 3-dB beamwidth in radians is given by equation (2.6):

$$\theta_{3\text{dB}} \approx \frac{\lambda}{D} \tag{2.6}$$

Equation (2.7) is attained by combining the equations (2.5) and (2.6):

$$\Delta CR \approx R\frac{\lambda}{D} \tag{2.7}$$

From equation (2.7) it could be concluded that fine azimuth resolutions at long ranges require large antennas. Sometimes, even at shorter ranges, achieving narrow azimuth beams can require antennas that are too large to be practical for mounting on a vehicle. However, imaging techniques or special antenna design could be used as an alternative solution to the large antenna aperture sizes [23].

2.2.3 Synthetic Aperture Radar (SAR)

Synthetic Aperture Radar (SAR) is a coherent technique which was initially introduced for airborne radar mapping of large areas on the ground. It employs an antenna with a modest aperture size and relatively wide azimuthal beamwidth [23]. The *antenna* would be moved by its platform along a path in space to form the synthetic aperture. The resulting azimuth or cross range resolution may be comparable to what would, in practice, be achieved by a real aperture with a length equal to the path length synthetic aperture (L_{SA}) [18]. Equation (2.8) expresses the cross range resolution (ΔCR) achieved by the synthetic aperture (L_{SA}):

$$\Delta CR = \frac{R\lambda}{2L_{SA}} \approx \frac{\lambda}{2\Delta\theta} \tag{2.8}$$

where λ is the wavelength, R is the range and $\Delta\theta$ is the synthetic aperture angle; the angle subtended by the synthetic aperture as seen from the target position. The factor of two in the denominator is due to the fact that the transmit location moves with the platform, whereas the entire aperture is used on transmit in a real antenna aperture [18, 23]. In some cases, inverse SAR (ISAR) technique is used where the movement of the target rather than the antenna platform would produce the synthetic aperture.

2.2.4 InSAR

Interferometric SAR (InSAR, also called "IFSAR"), which was initially developed by the Jet Propulsion Laboratory (JPL) to detect ocean currents or moving targets, could have two different applications: firstly to be used for moving target indication (MTI) and secondly to be used for target height measurements [19]. The latter is of the interest to this project, especially as an advanced technique in future developments. By using InSAR, variations in height of terrain are measured with very high precision so that it enables the production of three-dimensional maps [19, 23]. For measurements of the terrain variations; elevated and deep parts of the surface, at least two antennas at different altitudes are used to produce images of the same scenario. By coherently comparing the two images, information regarding the height of the targets is obtained. The other method is to use a single platform and antenna and to make two or more passes over the desired terrain at ascending or descending altitudes in order to produce a large synthetic vertical array [18]. One disadvantage of using an interferometric technique is the phase unwrapping, which can be challenging for electrically large targets (large relative to the wavelength).

The basic theory of SAR assumes that the surface of the scenario is flat. The distortions in the SAR image occur as a result of surface variations [19]. The so called distortions could be used in some cases, to measure the height of elevated objects above the flat terrain. One of the simplest methods of measuring the object heights is to observe the length of shadow. The object heights (h) can be calculated using equation (2.9).

$$h = L_{shadow}\frac{H}{R_g} \tag{2.9}$$

where L_{shadow} is the length of shadow, H is the height of the platform and R_g is the range to the target on the ground [18].

2.2.5 Image interpretation

Low return areas

When observing a radar image, sometimes regions with low intensities are seen. In SAR imagery these areas are known as *no return areas*. Instead in this thesis they are referred to as *low return areas*. The objects or surfaces that cause very low intensity areas in an image are categorised as follows:

- Shadow area. This will be discussed in the next section.
- Objects and surfaces that look *smooth* to the radar depending on the frequency of operation (wavelength) of the radar. To low RF frequencies, surfaces such as tarmac (asphalt) might look smooth, but to higher frequencies (mm wave and above) such surfaces would be considered rough. According to the Rayleigh criterion which was discussed in section 2.1.5, the reflection from such smooth surfaces is mostly specular, therefore most of the incident energy would be scattered away from the radar receive antenna. These surfaces appear as areas of very low intensity on the

image. This will be discussed further in chapter 6 when comparing the imaging results at 30 GHz and 150 GHz.

- Still water surfaces, ranging from small ponds, puddles and rivers to lakes, waterways, and finally the ocean. A still water body acts like a mirror; it specularly reflect most of the incident energy from a monostatic radar transceiver away from the transceiver [19].

Shadowing

In the scene illuminated by radar some objects may reflect or absorb practically all of the incident energy, transmitting through little or no energy for the illumination of other targets in range behind them. Therefore, such opaque objects cast radar shadows away from the radar transmitter [23] . Shadows are detectable in images as areas of low intensity down-range from the intervening objects [16]. Fig. 2.3 shows SAR images of an armoured vehicle [23]. The radar was located below the bottom line of the images, and the shadows produced by the vehicle with different orientation from the radar point of view are observed. Usually large, solid objects with significant height (like the vehicle) introduce clear shadow regions on the image [19]. The shadow width on the image is defined by the size of the target in azimuth. For instance, in Fig. 2.3, by comparing the images (a), (b) and (c), it is evident that the width of the shadow created behind the vehicle depends on the orientation of the vehicle with respect to the radar transmitter. The shadow length on the ground is equivalent to the height of the target divided by the tangent of the local grazing angle; so that the shadows created by taller objects and low grazing angles are longer [23].

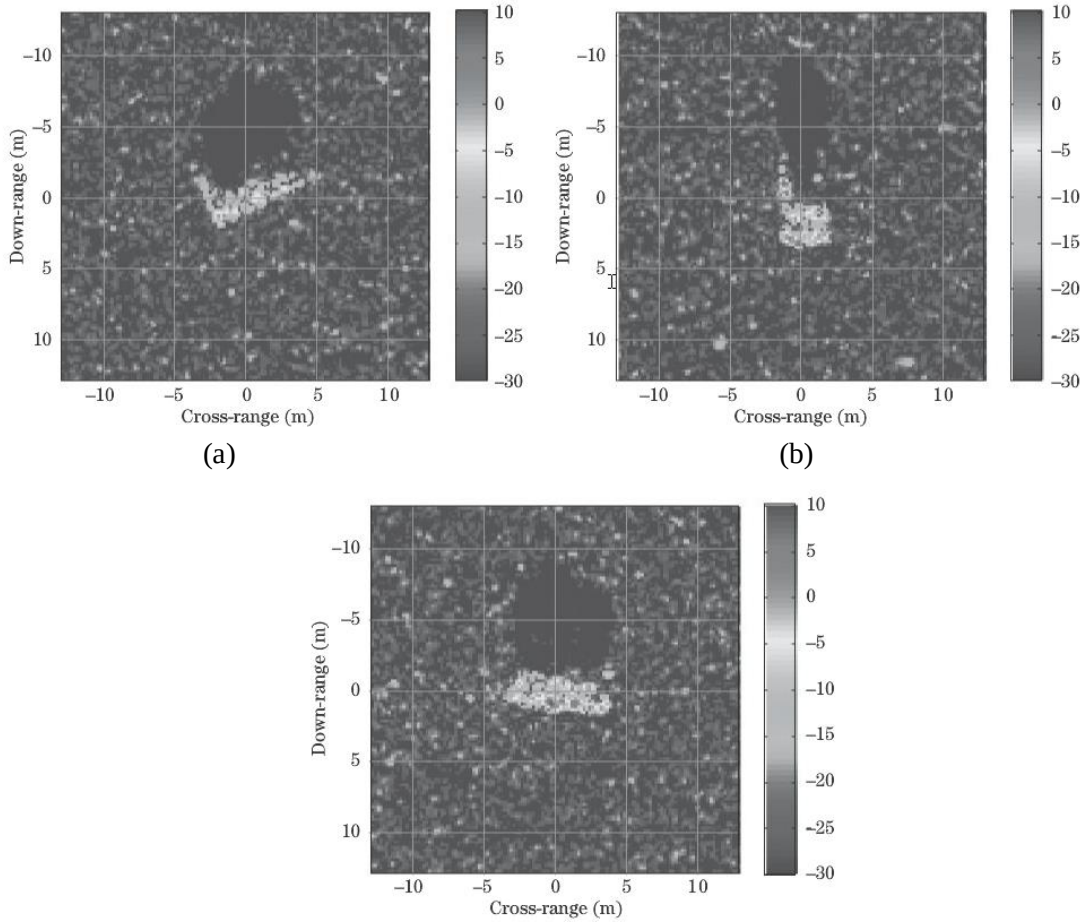

Figure 2.3.Three SAR images of an armoured vehicle with radar at the bottom of each image and the vehicle (a) at a non-cardinal pose angle, (b) broadside to the radar, and(c) end-on to the radar. Pictures are taken from [23] for illustration purposes.

2.3 Terahertz (THz) Sensing

2.3.1 Introduction

Terahertz (THz) technology is currently a research topic of interest, and research into the THz frequency band is receiving growing attention around the world. This is due to technology advancements making high frequency miniaturised components possible in the near future. Initially, there were some obstacles; the range limitation is due to both strong absorption of electromagnetic energy at these frequencies in the atmosphere as well as the relatively low power available from most sources [30]. According to McMillan [31], when the research in THz frequencies started, many systems were passive as it was very difficult to

produce high power transmitters at these frequencies. Nowadays, by rapid increase in developing high power transmitters and Monolithic Microwave Integrated Circuit (MMIC) devices, many new applications have been realised [32].

2.3.2 THz frequency gap

The THz frequency band which lies in the frequency gap between the InfraRed (IR) and MicroWave (MW) frequency regions, has been loosely defined and called differently by various researchers in the field; it is generally defined as frequencies from 300 GHz up to 3 THz [32]. McMillan [31] defines the terahertz (THz) band as the frequencies starting from about 200 GHz to about 30 THz. Whereas Wallace [33] defines the THz band as the frequency range above 100 GHz up through the infrared region.

Most of the research so far has been focussed on the lower part of the THz spectrum as the atmospheric attenuation is less severe and the technology is more mature. As mentioned in chapter 1, In this study the term “low-THz” is used to refer to the portion of the electromagnetic spectrum from 0.1 to 1 THz [4] .

Researches in the field of photonics move in frequency down to THz frequencies to achieve the unique capabilities of THz region in comparison to photonics and visible light. The biggest advantage is the atmospheric attenuation, and the fact that many objects that would look opaque to visible light appear transparent to lower frequencies (THz region). This is an important advantage for surveillance and security applications. RF researchers in the field of radar systems would move up in frequency, to take advantage of higher frequencies in respect to aperture sizes and available bandwidth.

2.3.3 Advantages and limitations of THz frequencies

Advantages

Advantages of use of THz frequencies were briefly mentioned in section 1.1 and are elaborated here. Firstly, the main drive for exploring such high frequencies in the electromagnetic spectrum to be used in radars is the aperture sizes for a given angular resolution. The aperture size is an important factor for some applications such as automotive radars. When considering the complete system however, it must be taken into account that the sensitivity of radar is determined by the aperture of the receiving antenna. Therefore it will be reduced if the antenna is made smaller [34].

Secondly, by using higher frequencies, wider bandwidths are available; therefore the range resolution of the radar can be enhanced. The spectrum is also much less crowded. Thus, there is plenty of room for the wide-band transmissions which are essential to achieve high range resolutions [34].

In synthetic aperture radar (SAR), for a given azimuth (cross-range) resolution, the synthesised aperture is reduced in extent as the frequency increases. This then reduces the requirements for motion compensation [33]. Even though SAR imaging is not applicable to this study, motion compensation could be applicable to other azimuth refinement techniques.

Finally, another important advantage of using THz frequencies is the texture sensitivity. At these frequencies, the wavelengths are rather small in the ranges of 3mm to 30 μm. This will lead to sensitivity of these waves to surface and volume irregularities, and it could potentially be used for surface monitoring and identification. The texture sensitivity will be discussed further in chapter 6.

Limitations

The first significant disadvantage of the THz frequencies is atmospheric attenuation. This has caused many doubts for the use of this frequency band in the past. However, the situation is not that black and white as low attenuation windows are available.

It can be seen from Fig. 2.4 that the clear-air attenuation increases from around 1dB/km at 100 GHz to 100 dB/km at 1 THz, and it increases even further at higher frequencies. While there are some absorption peaks due to presence of atmospheric gases like O_2, CO_2 and water vapour, there are the windows of lower attenuation between these peaks. For instance, the attenuation at 150 GHz in clear air does not exceed 2-3 dB/km, and at 300 GHz it does not exceed 10 dB/km. Attenuation from rain which occurs at all lower frequencies flattens off at higher frequencies. Interestingly, fog and mist, which have a considerable effect at millimetric and infra-red frequencies, have little effect compared to the very high levels of clear-air attenuation [34, 35]. A recent publication [36] demonstrates the experimental results of propagation with minimal distortion and attenuation of broadband THz signals through 137 m of dense fog with an approximate visibility of 7 m.

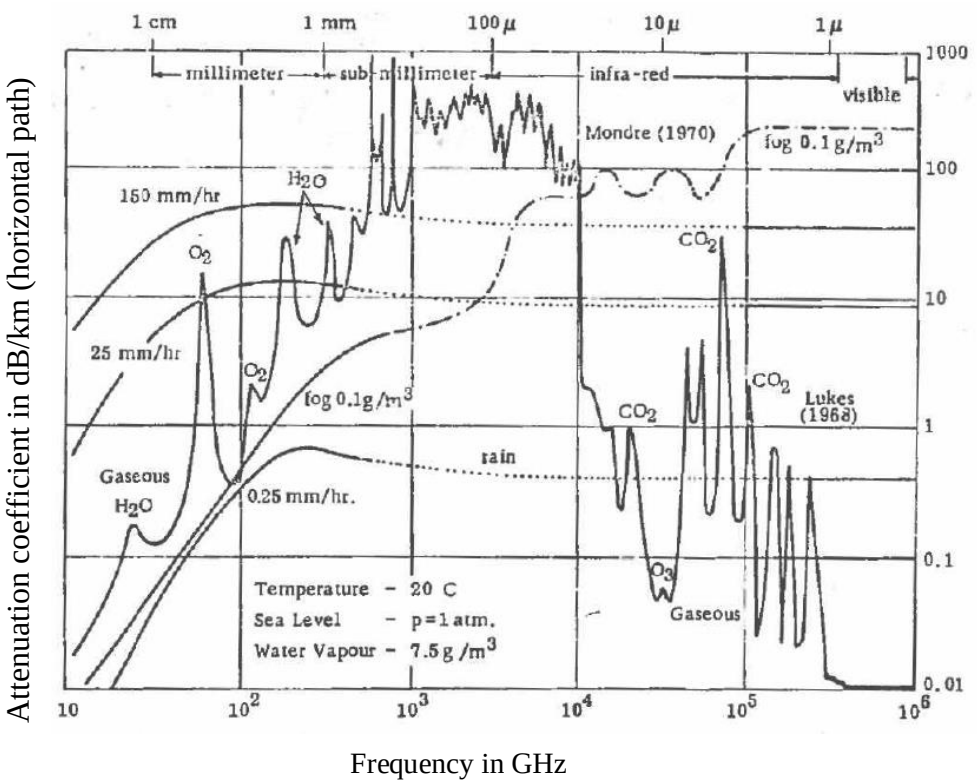

Figure 2.4: Atmospheric attenuation as a function of frequency [34].

It can be concluded that the practical maximum range for THz radar systems is a few hundred metres [34]. Even though the THz band was initially researched for airborne radar applications [34], the attenuation in the atmosphere would not be tolerable over kilometres of distance. However, it is suitable for automotive or security and surveillance applications within the ranges of a few hundred metres. The availability of high power miniaturised components is an issue at the moment, but this is expected to be resolved by the availability of the technology in the next 5-10 years.

2.3.4 Applications to date

For more than a decade, research on low-THz imaging systems has been focused mainly on hidden weapon detection. An example of such systems is the 675 GHz imaging radar for Standoff Personnel Screening developed by Cooper et al. [28]. Recent reviews of the several above 100 GHz technologies for concealed weapon detection are published in [33, 35]. THz imaging arrays made in CMOS technology and several forms of THz active imaging systems

with real time capabilities have been reported in the literature [37, 38]. Some interesting studies have been also reported in chemical sensing and non-destructive testing [39], medical imaging [40], helicopter landing aid [41], as well as in mapping and navigation [42]. However, only short-range body scanners have progressed to the commercial stage of development so far [43] [4].

2.3.5 THz Imaging

The Fraunhofer Institute has published interesting results [44] obtained in 2014-2015 about high resolution SAR and ISAR imaging made at about 300 GHz with the radar system named MIRANDA-300. The FMCW radar operating at 300 GHz provides a bandwidth of more than 40 GHz leading to a range resolution of 3.7 mm. The output power is reported to be around 5 mW over the whole bandwidth. The system is primarily designed for medium range applications up to several hundred metres. Fig. 2.5 shows the ISAR imaging result of a bicycle on a turn-table at a distance of 140 m from the radar, mounted at a height of 5 m. As can be seen, many details such as the spokes, the chain, and the gear wheels are distinguishable. Fig. 2.5(b) shows a zoomed in version of the image which is rich in details [44]. It should be stressed, that a few hours of integration time has been used for producing this image. Even though the presented results are very encouraging, the SAR and ISAR imaging techniques are not suitable for applications that require forward looking radars. An example of this type of application is automotive radars where the direction of motion and antenna beam axis are parallel.

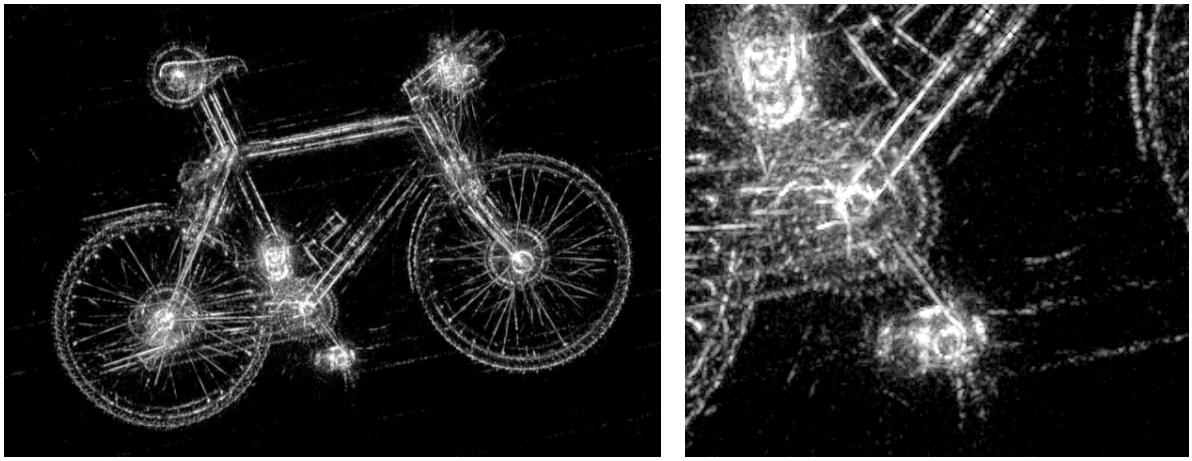

(a) (b)

Figure 2.5 : ISAR measurement of a bicycle at a distance of 140 m [44].

2.4 Automotive radars

Automotive Radars have been the backbone of driver assistance systems for decades [45]. A comprehensive overview on the development of driver assistance and active safety systems is given in [45-47].

2.4.1 Brief History of developments to date

Automotive radar has been under development since the mid 1960's. According to some references, it began to be developed as early as the 1950s though none of the preliminary work led to practical products. The earlier research work on automotive radar in the UK during the 1950s was carried out at the Road Research Laboratory, which is now the Transport and Road Research Laboratory (TRRL) [48]. By the 70s, research into automotive radar development in microwave frequencies began to intensify. Early work by Scott-James and Anderson at the British Aircraft Corporation is an example of the work in the 1970's [49, 50]. They used separate transmit and receive horns mounted on the roof of an old Ford Anglia to measure the range and velocity of the vehicles ahead (see Fig. 2.6). The vehicle

speed was measured using a sensor on the prop shaft. These measurements provided the basic components of an Intelligent Cruise Control system.

Another prototype automotive radar from the 70's was called 'AVOID' [51], and was built by Mullard research laboratories. Even though AVOID was capable of driving without any driver, it was never intended for use on public roads, instead it was used to assist emergency vehicles in finding their way around airports in adverse weather conditions such as dense fog. This project never reached the market because its steep cost did not justify the number of times it would have been used [51].

From the initial stages in automotive radar development, the main drive for all the research has been the idea of collision avoidance [47]. Stove, in his publication in 1991 [48], suggests three main categories for car obstacle radar functions: 1. Crash prediction radar; 2. Headway Measurements radar which is used for Intelligent Cruise Control (ICC) (nowadays this type of radar is known as Adaptive Cruise Control (ACC)) and 3. Obstacle warning radar which was not expected to reach the market up to ten years after the publication date (i.e. 2001).

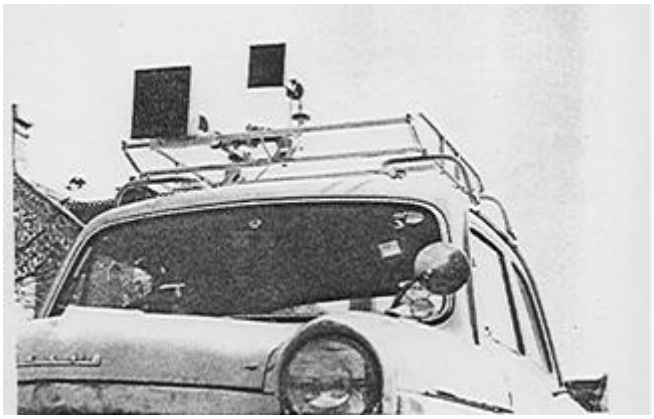

Figure 2.6: Prototype device on experimental car [50]

After a quiet period between the 1970's to 1990's which was at the same time as the Cold War, there were remarkable advancements both in the microwave sensor technologies (i.e.

semiconductor microwave sources like Gunn sources and GaAs MMICs) and signal processing in the form of more powerful microcontrollers and digital signal processors. These advancements made commercialisation of automotive radars feasible in the 90's. For example, collision warning systems were introduced in the US in 90s [47]. In the early 1990's many companies that were initially developing missile seekers, have directed their attention to research in automotive radars. For instance companies such as DASA (The German Aerospace Company), Lucas and Delphi have tried to go into the automotive radar development market but many of them dropped out as they deemed it not profitable enough to go under the strict restrictions of the automotive industry [50]. The companies, such as Delphi, which did not drop out, are still around today. The various constraints of automotive radar are explained in the next section.

According to a publication by Bosch GmbH in 2005 [47], ACC was commercialised for the first time in Japan in 1995. While Japanese automotive developers were more in favour of LIDAR based ACC systems, European and US companies have dedicated their research mainly to radar-based ACC. In 1999, the Mercedes S class was equipped with the 77 GHz "Distronic". This was followed by other luxury car manufacturers such as Jaguar (XKR, XK6), BMW (7 series), Audi (A8), Cadillac (STS, XLR), and VW (Phaeton), providing their vehicles with optional ACC. ACC was also available in the Mercedes E, CL, CLK, SL classes, the BMW 5 and 6 series, Toyota (Harrier, Celsior), Audi A6, Nissan (Cima, Primera), Lexus (LS, GS), and Honda (Accord, Inspire, Odyssey). At this time the ACC was introduced as an optional comfort feature. Japanese car manufacturers like Honda and Toyota went one step further and introduced an active brake assist collision qualification (additionally to ACC) in 2003 based on 77 GHz long range radar (LRR). The active brake assist system offered a breaking system with much higher impact for slowing down in

hazardous situations compared to the smooth deceleration performance of an ACC system [47].

2.4.2 Automotive Constraints

The automotive industry is known for very strict constraints. In order for a sensor to meet an automotive manufacturer's requirements it must have certain size, styling, reliability and environmental performance level [52].

Styling is an important factor in automotive design and no matter how proficient a radar sensor is, it will be unacceptable if it cannot be adapted into the vehicle package. The front bumper area (including the grille area-behind the badge), despite being physically vulnerable to impact, has been the area where the radar is packaged. An accurate, suitably rigid support structure is also required; this must be part of the main body shell.

Radar performance is also an important consideration in the choice of sensor placement. Sensor height affects both multipath performance and additional issues such as aperture obscuration by dirt, water drops, ice and impact damage [52].

In addition to all above, the radar has to withstand temperatures form -40 ° C to 85 °C; meet a target weight ; and be capable of mass production with consistent performance at low cost [52].

2.4.3 77 GHz Automotive Radar

The 76– 77 GHz band was regulated in the 90's for automotive applications followed by a standardisation in Europe (ETSI EN 301 091). Now this band is allocated for Intelligent Transport Services (ITS) in Europe, North America, and Japan [47].

77 GHz radars are currently used for Adaptive Cruise Control (ACC) systems in vehicles in order to automatically increase or decrease the speed of the vehicle to maintain a fixed gap

with other objects or vehicles on the road. As it was reported by [47] in 2005, the main manufacturers of 77 GHz Long Range Radar (LRR) sensors were ADC (subsidiary of Continental Temic in cooperation with M/A-Com), Bosch, Delphi, Denso, Fujitsu Ten, Hitachi and ZF TRW. Fig. 2.8 shows the Bosch 2nd generation ACC radar and Fig 2.8 shows its RF PCB. The packaging size is about 74 x 70 x 58 mm^3. The FMCW modulated 77 GHz waveform [53] feeds four elements (poly-rods) which are directly attached to four patch elements on the RF board, illuminating a dielectric lens. A broad illuminating transmit beam is achieved by a monostatic analogue beamforming approach. Four single overlapping beams at the receiver end produce a total azimuthal coverage of ±8 degrees [47].

Figure 2.7: Bosch ACC radar, 2nd generation [47]

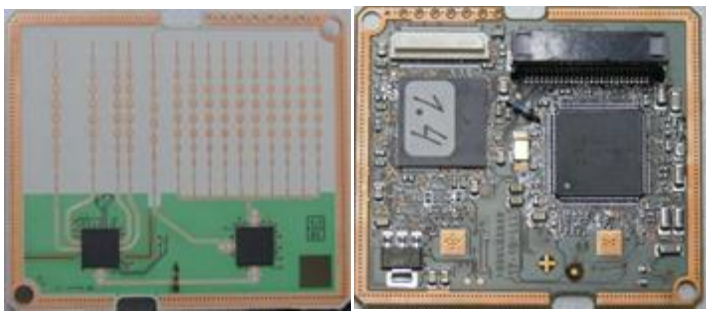

Figure 2.8: RF PCB of the Bosch ACC radar [54]

Table 2.1 summarises the existing automotive radar technologies for short, medium and long range applications. The short, medium and long-range operation of the radar is defined by the application. In automotive radar, measurements of up to 30 m ahead of the vehicle are usually considered short range. The long range application refers to ranges of more than 150 m up to 250 m. The radar under discussion is intended for medium-range application with defined range of 4-100 m. Some of the parameters mentioned in the Table 2.1 can be compared to the FMCW radar parameters introduced in chapter 5.

Table 2.1.1: Existing automotive radar technologies [9]

	Long range radar	Mid range radar	Short range radar
Frequency band	77 GHz	79 GHz	79 GHz
Max. output power EIRP	+55 dBm	-9 dBm/MHz	-9 dBm/MHz
Bandwidth	600 MHz	600 MHz	4 GHz
Distance range	10-250 m	1-100 m	0.15-30 m
Distance resolution	0.5 m	0.5 m	0.1 m
Speed resolution	0.1 m/s	0.1 m/s	0.1 m/s
Angular accuracy	0.1°	0.5°	1°
3 dB Beamwidth Azimuth	±15°	±40°	±80°
3 dB Beamwidth elevation	±5°	±5°	±10°

2.4.4 Present and future trends

Nowadays automotive radar is not anymore a niche sensor for only luxury cars; it is becoming a commercial standard even for mid-range cars. Therefore, the market for automotive radar sensors is expected to significantly increase over the next years [54].

The new six years research plan of the EU includes further reduction of traffic fatalities [46]. 2011-2020 is named as the decade of action for road safety in Europe and automotive radars as well as cameras are considered as the main technology force for this approach in the future [46] . Autonomous driving is the ultimate and long term target of the EU research. However Chinese and Japanese manufacturers are on this track too.

Today many automotive radar manufacturers such as Delphi, ZF TRW and Bosch GmbH, radical car manufacturers such as Tesla Motors [55], traditional manufacturers [56] and even non-automotive companies such as Google [57] are advertising and demonstrating the autonomous (self-driving) capabilities of their vehicles or sensor systems. This seems to be the new trend in driving. Urmson, a roboticist (from Google), who was previously involved in the development of the autonomous vehicle for off road conditions in the 2005 DARPA Grand Challenge [58], has recently discussed the necessity of autonomous driving [59].

In March 2015, Delphi announced the completion of America's first and longest coast-to-coast drive (nearly 3,400 miles) with an autonomous driving vehicle. The vehicle is equipped with six long range radars, four short range radars, three vision based cameras, six LIDAR, a localisation system, intelligent software algorithms and a full suite of Advanced Driver Assistance Systems (ADAS) [60].

On July 2015 Tesla Motors announced that the company is "almost ready" to make its cars go driverless on highways and parallel-park themselves [55]. A list of the functions that radar will have to face and to perfect in the future is discussed in reference [45].

3. High Resolution Imaging Method

Overview- *This chapter explores the feasibility of high resolution two dimensional (2D) imaging for automotive applications. The discussed imaging method is 2D mapping by physical beamforming using forward looking radar.*

The three basic stages of data acquisition, data processing and image formation are explained in this chapter. The waveform used for achieving high range resolution is the Stepped Frequency Waveform (SFW). To exercise the methodology, measurements have been taken at various frequencies starting at 7.5 GHz.

3.1 Physical Beam Mapping

In order to produce a 2D image map of the area in front of a moving vehicle in a road environment, a forward looking radar system is required, where the direction of motion and the radar beam axis are parallel. Fig. 3.1 shows a drawing of a vehicle with antennas mounted at the front. The antenna can be a multi beam or it can be scanning antenna in the azimuth plane with a narrow beam. Scanning can be electronic or mechanical. In the physical beam mapping method , the two dimensional image is produced by generating range profiles over a series of scans and then placing the profiles next to one another in the order they were collected. One scan is defined as signal acquisition when the radar is at one specific angle. The range profile is defined as the two dimensional plot of radar return magnitude in range. Range profile will be shown further in section 3.3.3.3. The narrow-beam antenna (in azimuth) illuminates a different portion of the scene in each scan angle. The radar system used in this study is a mechanically scanned antenna, so that the antenna illuminates a slightly different portion of the scene within each scan angle. The collected data is processed, and a two-dimensional intensity image map as a function of range and azimuth angle is formed. The

map shows the amplitude of reflection from the total scanned road area as a function of azimuth and range. Image formation is discussed in section 3.4.

Top level requirements that should be met in designing a scanning high resolution imaging radar system for automotive applications are discussed in section 1.3.2.

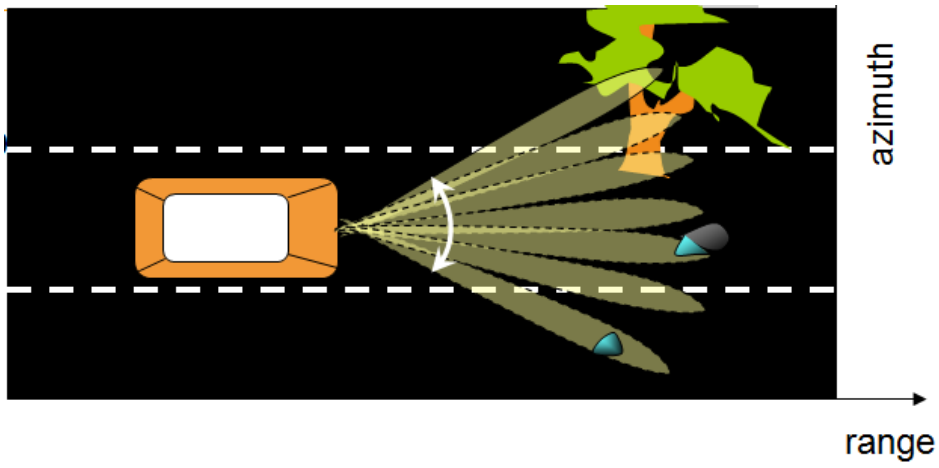

Figure 3.1: Scanning the illuminated area in front of the antennas mounted on the vehicle.

3.2 High range resolution

In order to deliver high range resolution, wide operational bandwidth is required. The wide bandwidth is achieved via one of the three methods [61]:

1. **Pulsed Radar (Impulse)**: The pulse radar operates by transmitting extremely narrow pulses of high power.
2. **Stepped-frequency waveform (SFW)** is defined as successive pulses with linear increase in frequency in discrete steps. This means that modulation occurs across pulses instead of within pulses. The wide effective bandwidth is achieved with narrow instantaneous bandwidth. The required peak transmit power is lower than pulsed radars because the total time on target is longer through successive pulses [62] .

3. **Pulse compression** (e.g. Frequency Modulated Continuous Wave -FMCW); Transmitting modulated pulses instead of reduced time duration; received pulses are processed by correlation with transmitted pulses.

The second and third methods are explored in this thesis. In this chapter, the stepped frequency waveform is introduced. The pulse compression technique is discussed in chapter 5, where the FMCW radar operating at 150 GHz is introduced. The SFW uses a series of pulses to achieve range resolution, whereas the pulse compression technique uses modulation within a single pulse. The stepped frequency waveform can be described as the discrete form of the FMCW waveform.

3.3 Stepped Frequency Radar system

3.3.1 Stepped Frequency Waveform

In this study, the successive coherent pulses with linear increase in frequency are generated and recorded by the Vector Network Analyzer (VNA). The VNA is used as a radar system by connecting two antennas to the transmit and the receive channels. A network analyzer is one of the most complex and versatile pieces of test equipment in the field of RF engineering [63]. It is used in applications in research and development, and for test purposes in production. When combined with one or more antennas, it becomes a radar system (see Fig. 3.2).

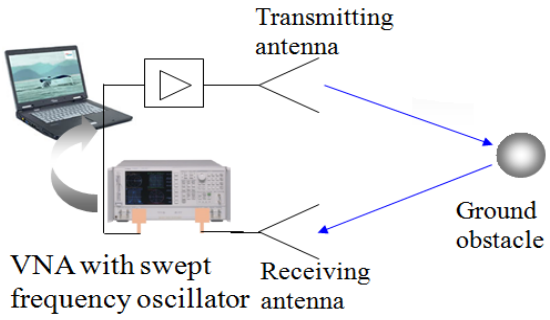

Figure 3.2: Radar Configuration using Vector Network Analyzer (VNA)

The successive coherent pulses with a linear increase in frequency are described using equation (3.1):

$$f_n = f_0 + n\Delta f \tag{3.1}$$

where, f_0 is the starting carrier frequency, Δf is the step size , f_n is the *n-th* carrier frequency, and $n = 1,2,\ldots N$, so that each *sweep* consists of N pulses (frequencies). The effective bandwidth (BW) is defined using equation (3.2):

$$BW = f_N - f_0 = N \cdot \Delta f \tag{3.2}$$

The effective bandwidth does not depend on *instantaneous* bandwidth Δf, and it can be increased by increasing the number of samples ($N \cdot \Delta f$). In this case, it is defined as the number of samples for a chosen bandwidth in the VNA setting menu. Fig. 3.3 shows the stepped frequency waveform.

The generated series of pulses are transmitted via the transmit antenna (Tx) connected to port 1 of the two port VNA (see Fig. 3.3). The transmitted pulses illuminate the scene and a portion of the transmit energy will be reflected back towards the received antenna (Rx), connected to port 2 of the VNA. The transmission coefficients (S_{12} and S_{21}) are measured and logged by VNA. The transmission coefficient (S_{12}) is the ratio of the amplitude of the received voltage (V_1^-) wave to the amplitude of the transmitted voltage wave (V_2^+) as shown in equation (3.3) [64].

$$S_{12} = \frac{V_1^-}{V_2^+} \tag{3.3}$$

A large value of the transmission coefficient measured by the VNA means that a significant amount of transmitted energy is reflected back towards the transceiver. This is a result of large RCS objects being present in the scene. Objects or areas on the ground with a large

value of (S_{12} and S_{21}) appear as areas of high intensity on the map when plotted on the image. This will be demonstrated later with the images presented in this thesis.

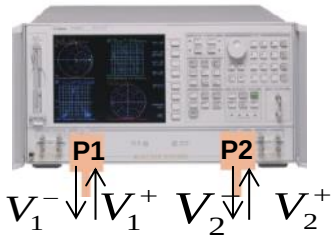

Figure 3.3: Two port Vector Network Analyzer

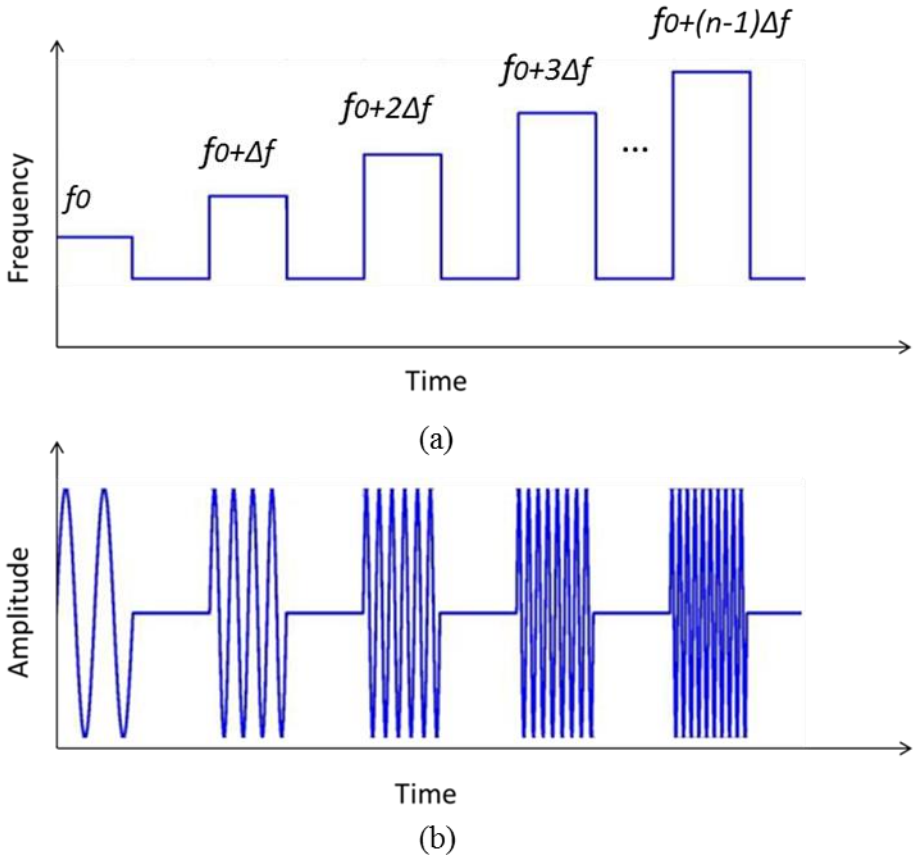

Figure 3.4. Stepped Frequency Waveform [65]. Chirp signal in time (a) and frequency domain (a) versus increasing frequency steps in time versus frequency domain.

The measured transmission coefficient is logged. Fig 3.5(a) shows a rectagular signal in frequency domain with the bandwidth of (f_N - f_0) which is formed of successive coherence

pulses. Fig 3.5(b) shows the Inverse Fourier Transform (IFT) of the rectangular signal in time domain which is a sinc function. According to the the duality property of the Fourier transform, a sinc-shaped pulse in the time domain has a rectangular shape magnitude spectrum [66]. A rectangular pulse is defined using equation (3.4) and its IFT (FT^{-1}) is defined in equation (3.5).

$$rect(f) = \begin{cases} 1 & f_0 \le f \le f_N \\ 0 & otherwise \end{cases} \tag{3.4}$$

$$\mathrm{FT}^{-1}\left[rect(f)\right] = \int_{-\infty}^{\infty} rect(f) e^{j2\pi ft} df = \mathrm{sinc}\left(\pi\left[f_N - f_0\right]t\right) \tag{3.5}$$

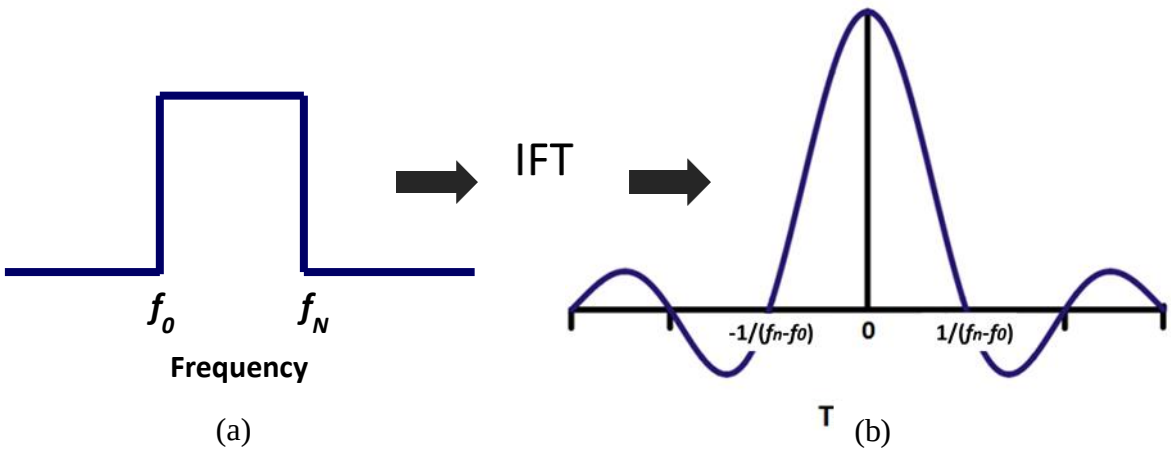

Figure 3.5: (a) Rectangular pulse in frequency domain (b) Sinc function in time domain

The width of the main lobe in the Sinc function defines the pulse duration and corresponds to the *BW* of the frequency domain signal. The Sinc function forms the timing mark for range measurements. Accurate range measurements can be achieved by having a very sharp or distinct timing mark. Achieving a very sharp timing mark would come at the cost of having a broad transmitted bandwidth (spectrum). The wider the bandwidth the narrower the Sinc function. As seen in equation (3.6), the 3-dB pulse duration (τ) is defined by the overall (effective) bandwidth [66]:

$$\tau = \frac{1}{BW} = \frac{1}{(f_N - f_0)} \tag{3.6}$$

The width of the main lobe of the time domain pulse defines the range resolution of the measurement. The range bin size (R_{bin}) is defined from width of one received pulse using equation (3.7), where c is the speed of light in vacuum.

$$R_{bin} = \tau . \frac{c}{2} = \frac{c}{2(f_N - f_0)} \tag{3.7}$$

Fig. 3.6 shows the profile of range bins across the range. Each column represents a return from a particular range bin. The Inverse Discrete Fourier Transform of a column creates the detailed representation of the range bin in range, by dividing it into N finer subdivisions. The width of a range bin (R_{bin}) is defined as ($c\tau/2$), and the width of the finer subdivisions is ($c\tau/2N$) [61].

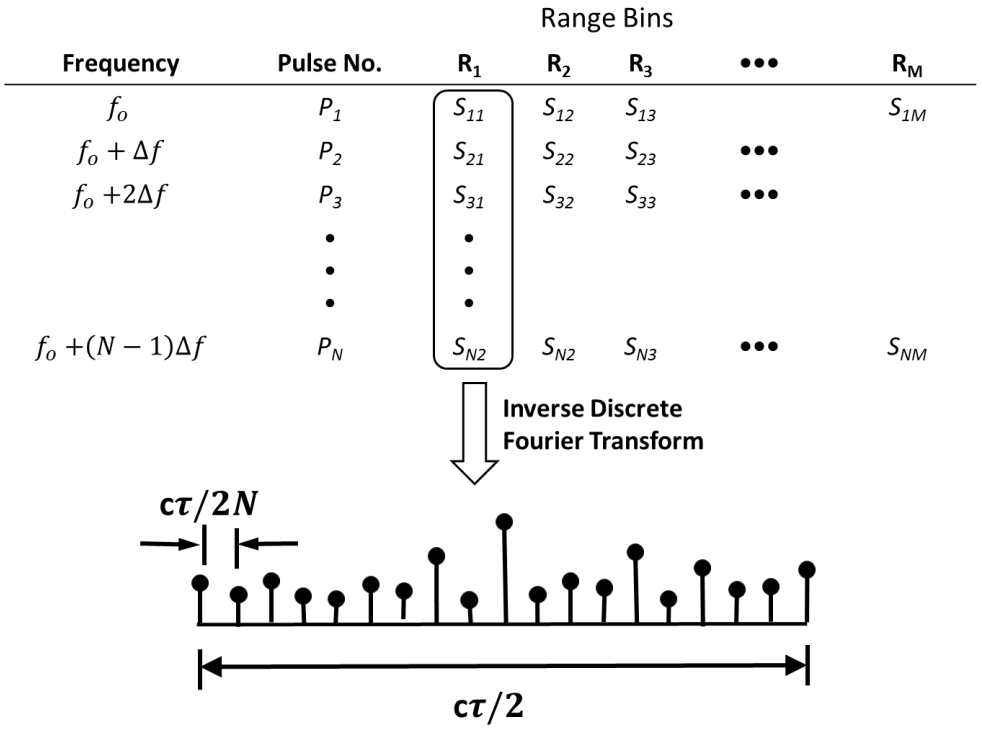

Figure 3.6: High resolution profile of a range bin [61].

The high level of side lobes in a Sinc function can result in masking of the response from objects with smaller RCS in the scene of interest. This means that in the case of two close-by objects in range, the side lobes of the pulse reflected by the object with large RCS can mask the reflection from the object with smaller RCS. It is therefore important to reduce the side lobes in the Sinc pulse. In order to do so, different window functions were investigated. The optimum results were achieved with a Gaussian window. It is important to find the optimum width of Gaussian window in order to avoid losing information in the main lobe as well as suppressing the side lobes. Fig. 3.7 (a) shows a Sinc function with high levels of sidelobes. Fig. 3.7 (b) and Fig. 3.7 (c) show the side lobes of the Sinc function suppressed with Gaussian windows with different widths.

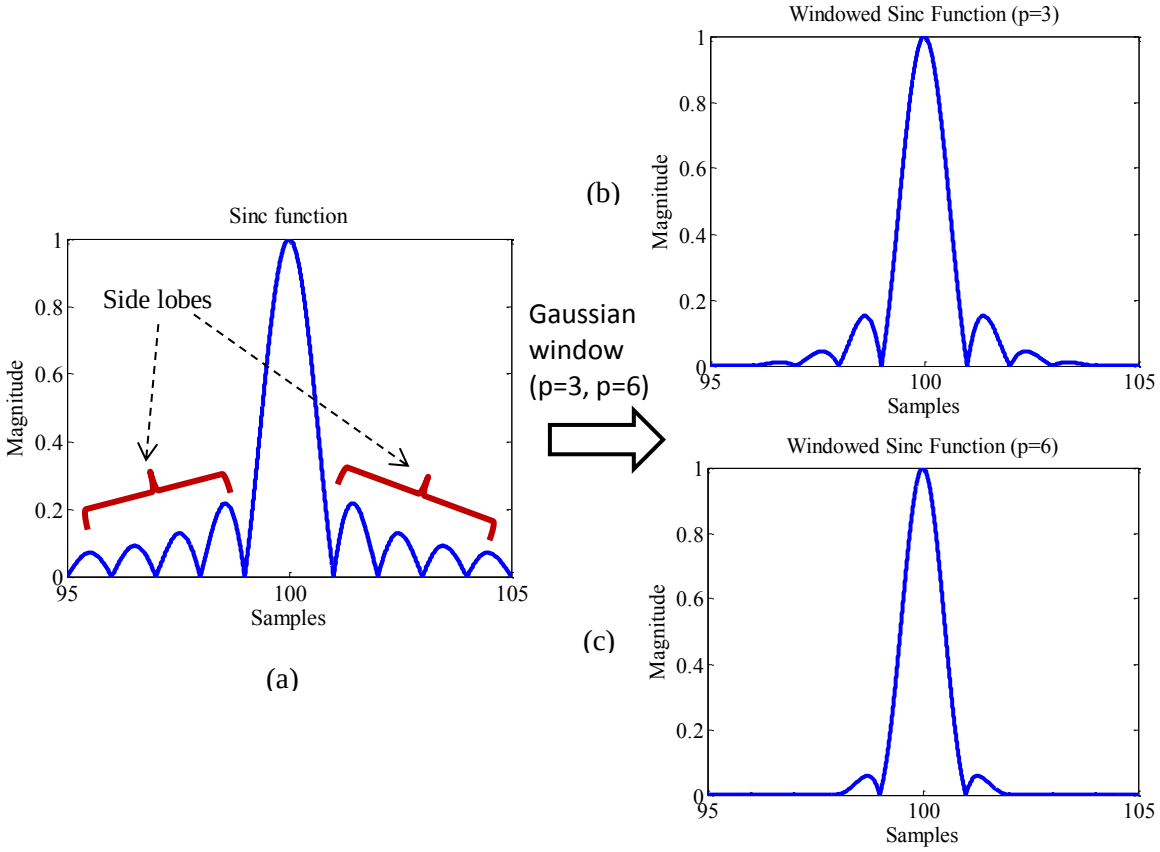

Figure 3.7: (a) Sinc function with high level of side lobes. (b) and (c) suppressed side lobes with Gaussian windows with different widths.

For the rest of this chapter, the methodology is verified by analysis of the received waveform passing through different propagation media.

3.3.2 Propagation medium I: Cable

In order to examine the methodology, the first propagation medium is chosen to be a cable. A cable is a more predictable and controlled propagation medium than free space. Fig. 3.8 (a) shows a standard 50 Ω coaxial cable that is connected to port 1 and port 2 of the VNA. The rectangular pulse (in the frequency domain) generated by the VNA is transmitted from port 1 to port 2 via the 50 Ω cable. The transmission coefficient (S_{12}) is measured and plotted in Fig. 3.8 (b). The pulse width is calculated according to equation (3.6). The width of the main lobe in the time domain pulse corresponds to the bandwidth, which in turn corresponds to range resolution. Two different *BW*s of 1.5 GHz and 3 GHz have been calculated using equations (3.6) and (3.7).

The 3 GHz *BW* correspond to: $\frac{1}{3(GHz)} = 0.33ns$ pulse, therefore $R_{bin} \approx 5$ cm

The 1.5 GHz *BW* correspond to: $\frac{1}{1.5(GHz)} = 0.66ns$ pulse, therefore $R_{bin} \approx 10$ cm

A wider *BW* provides the advantage of finer range resolution and better separation between the obstacles but leads to a greater value of noise in the system. According to Skolnik [18] noise is unwanted electromagnetic energy which interferes with the ability of the receiver to detect the wanted signal. Noise may originate within the receiver itself, or it may enter via the receiving antenna along with the desired signal [16]. The optimum *BW* is the one which provides a fine resolution as well as an acceptable level of noise in the receiver. Fig. 3.8 (c) shows the response of the cable with the suppressed side lobes using a Gaussian window.

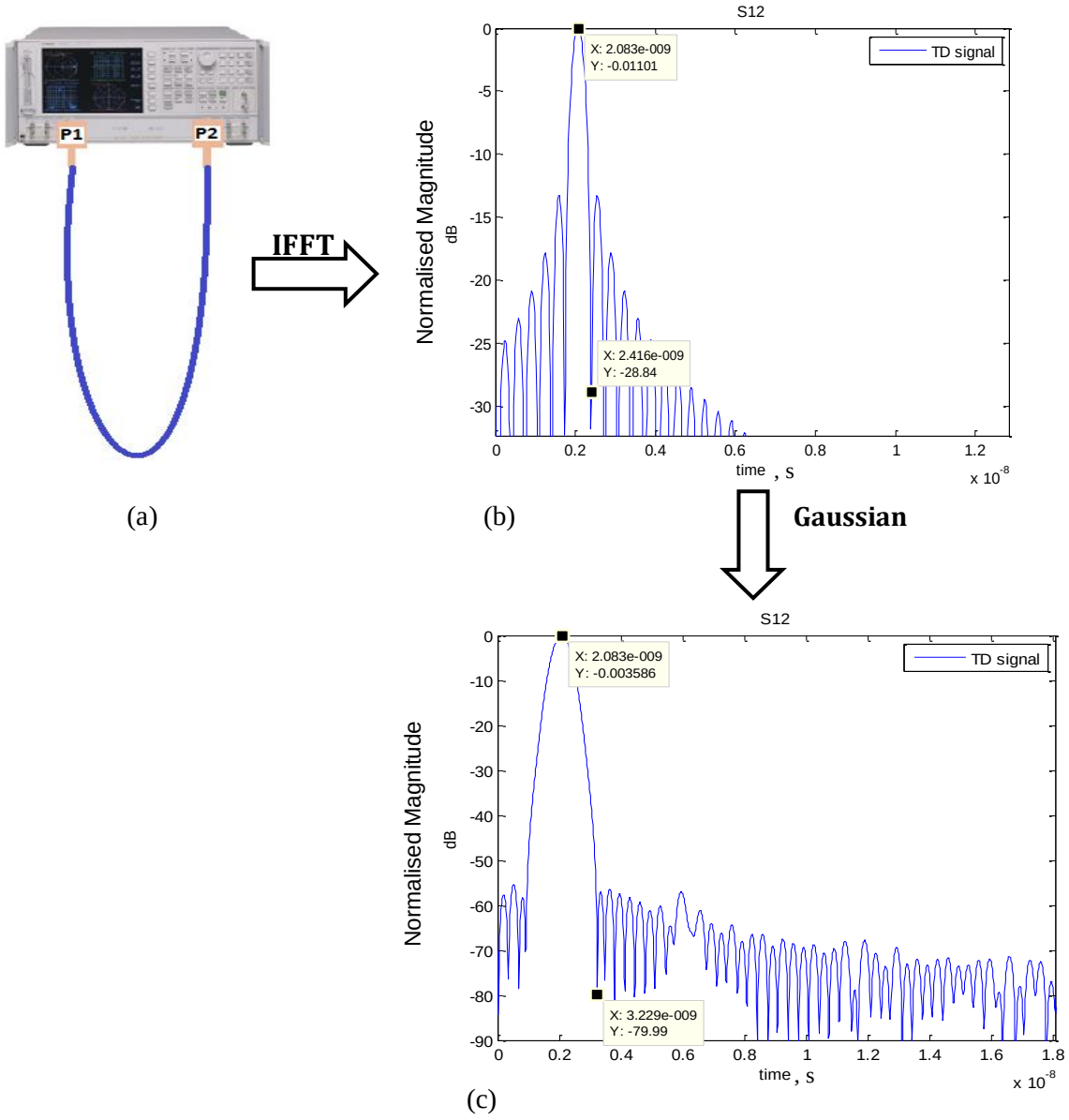

Figure 3.8: (a) Measured transmission coefficient of a standard 50 Ω cable (b) Time domain response of the cable (c) The side lobes of the Sinc pulse are suppressed after applying a Gaussian window.

3.3.3 Propagation environment II: Anechoic chamber

After measuring the transmission coefficient of a cable, the next stage is to move to a controlled propagation environment. The initial experiments have been done in an anechoic chamber. The centre operating frequency is 7.5 GHz and the *BW* is 1.5 GHz. Two UWB (1-18 GHz) Q-par Angus antennas were used as transmit (Tx) and receive (Rx) antennas. One connected to port 1 of the VNA and the other to port 2 of the VNA. Fig.3.9 (a) shows the

picture of the Q-par Angus horn antenna with 40° azimuth beamwidth. Fig. 3.9(b) shows the measurement setup. Tx is above Rx and they are isolated by an absorber that is placed between them. The midpoint between the apertures of the antennas is 90 cm above the ground. The VNA is an HP 8722D 50 MHz - 40 GHz. A metallic sphere with a 16 cm radius is used as a reference target. The sphere is placed at distances of 1.6 m and 3.8 m from the reference plane of the VNA.

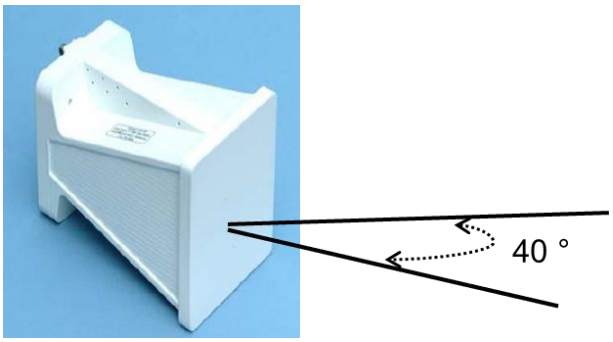

(a)

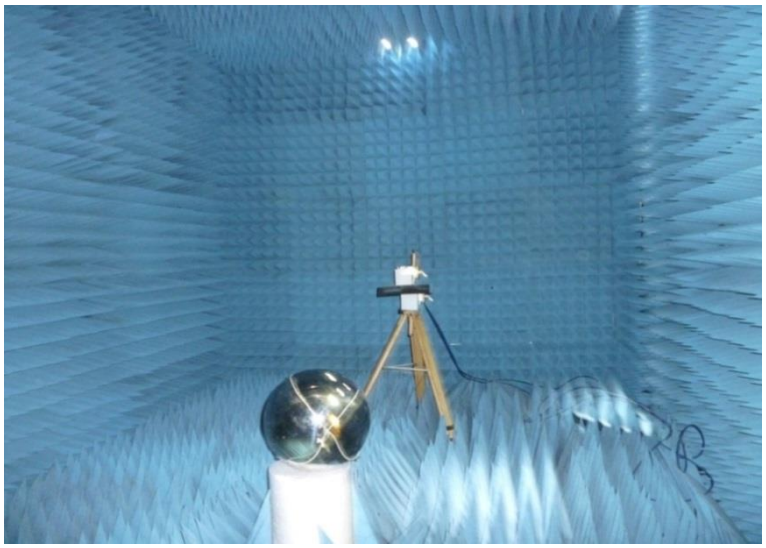

(b)

Figure 3.9: (a) UWB Q-par Angus horn antenna with 40° azimuth beamwidth. (b) Measurement set-up in anechoic chamber with a sphere used as a target

3.3.3.1 Signal Equalization

Fig. 3.10 shows the measured transmission coefficient magnitude spectrum of the scene of Fig. 3.9 (b).

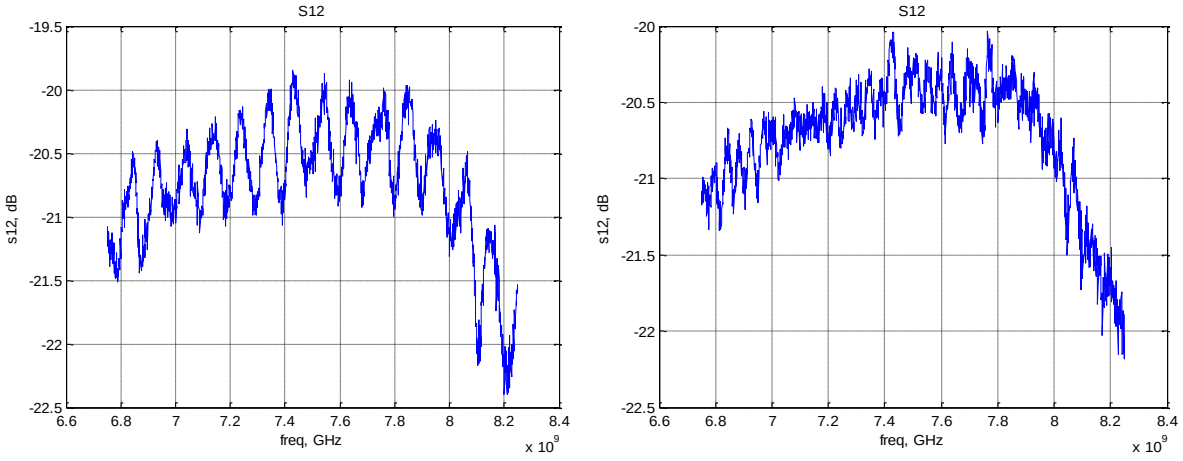

(a) (b)

Figure 3.10: Measured transmission coefficient (S_{12}), at the operating frequency of 7.5 GHz with the *BW* of 1.5 GHz; sphere is at (a) 1.6 m and (b) 3.8 m from the transceiver reference plane

In order to equalize the signal and reduce the clutter, the background signal is subtracted from the signal (with obstacle) [67]. This means that the transmission coefficient (S_{12}) of the illuminated area in front of the antennas is measured without the object of interest and it is called background signal (S_{bck}). The transmission coefficient (S_{12}) of the illuminated area containing the objects of interest (in this case the sphere) is measured and called (S_{sig}). Subtracting the measured background signal from the desired signal in frequency domain equalizes the signal. Equation (3.8) describes the equalized signal (S_{equ}).

$$S_{equ} = S_{sig} - S_{bck} \tag{3.8}$$

In other words, it consists of the response from the only change in the scene of interest which is the target (the sphere). Fig. 3.11 shows the equalized transmission coefficient of the sphere

at two different distances, which are presented in Fig. 3.10. It can be seen that the envelope of the signals is almost like a rectangular pulse.

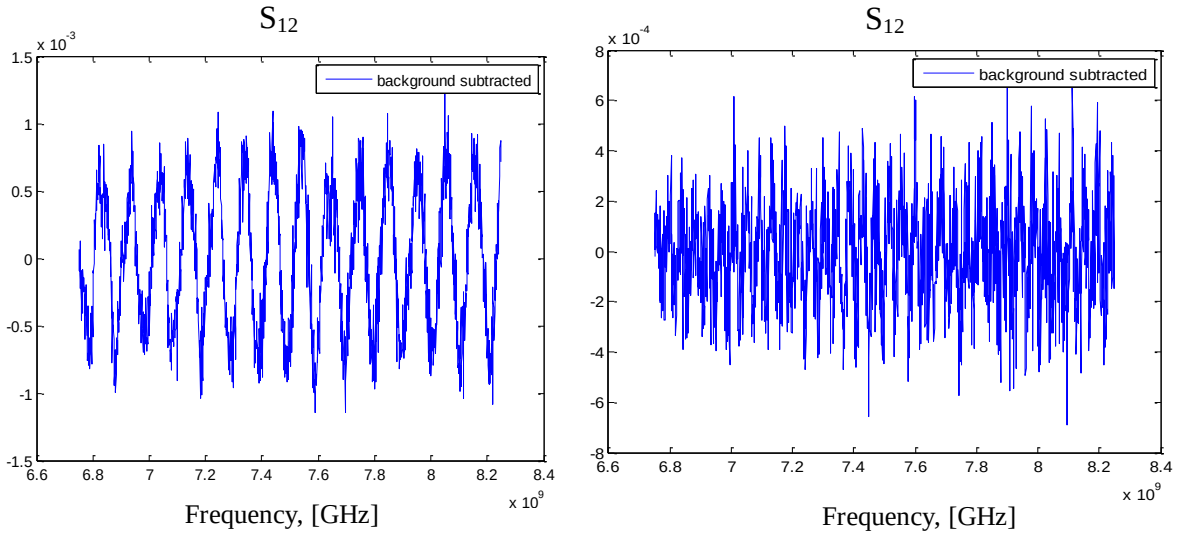

Figure 3.11: Equalized transmission coefficient (S_{12}) of the signals presented in Fig. 3.10, sphere at (a) 1.6 m and (b) 3.8 m in regards to the transceiver

3.3.3.2 Windowing

Gaussian window is used to suppress the Sinc function sidelobes before applying Inverse Fourier Transform (IFT) to the signal with rectangular envelope. Fig.3.12 shows the windowed frequency response of the signals presented in Fig. 3.11.

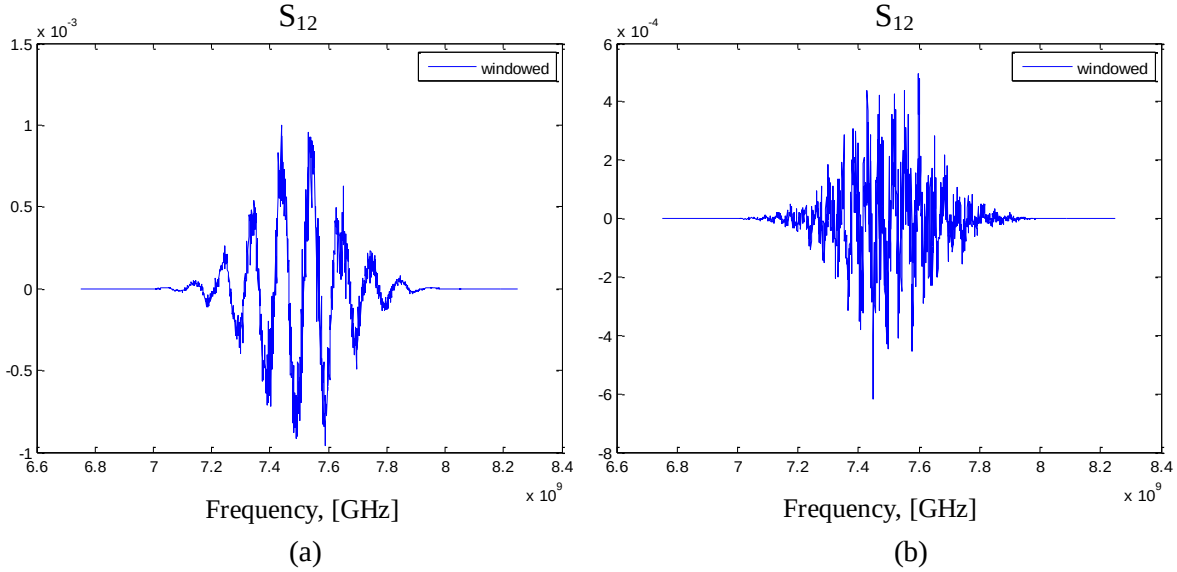

Figure 3.12: Windowed frequency domain response of the signals presented in Fig.3.11 (a) sphere at 1.6 m and (b) 3.8 m with respect to the reference plane of the transceiver

3.3.3.3 Time domain response

Fig. 3.13 shows the time domain response or range profile of the sphere corresponding to the frequency domain signals presented in Fig. 3.12. The time domain response is obtained after applying IFFT to frequency domain signals shown in Fig. 3.12.

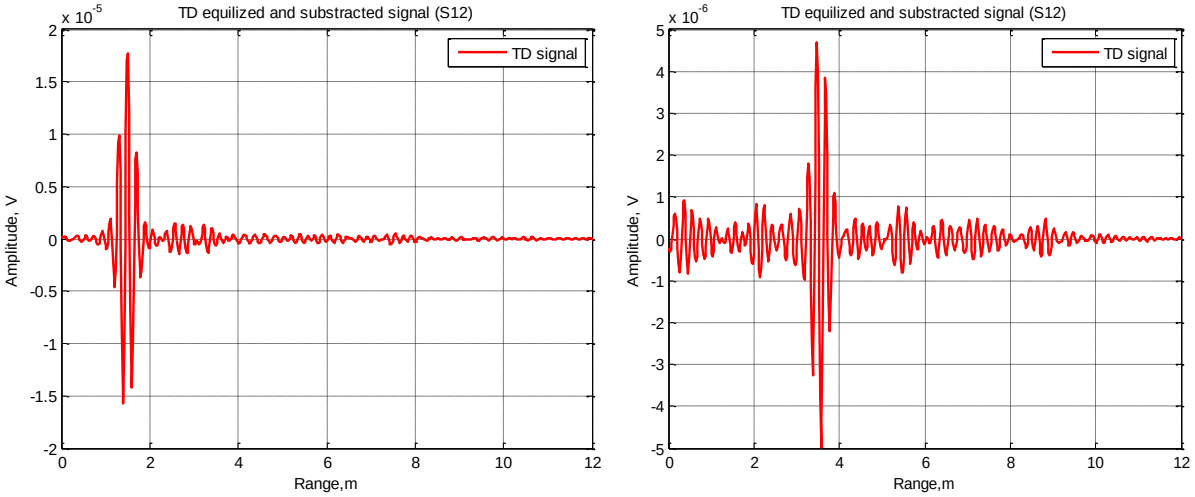

(a) (b)

Figure 3.13: Time domain response from a sphere at (a) 1.6 m and (b) 3.8 m from the transceiver

3.3.4 Propagation environment III: Outdoor Controlled environment

After experimenting in the anechoic chamber, the next stage is to go to a controlled free space environment. The roof top of the EESE Building at the University of Birmingham was chosen as the measurement site. The measurement set-up and parameters are kept the same as the previous measurement discussed in section 3.3.3 (see Fig. 3.14 (a)). Fig. 3.14 (b) and (c) shows the topology of the experiments with reference canonical targets, a sphere and a cylinder at the distances of 2.7 m and 1.6 m from the transceiver respectively at the same azimuth (lateral) position relative to the transceiver.

(a)

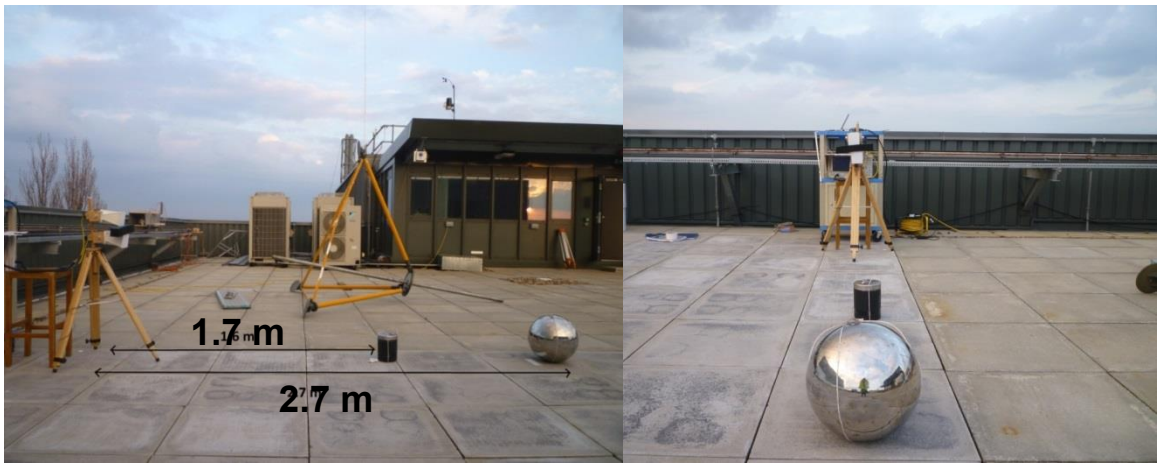

(b) (c)

Figure 3.14: (a) Experimental set up on the roof top of EESE building at the University of Birmingham. (b) and (c) shows the topology of the experiments with reference targets.

Fig. 3.15 shows the response from the sphere and cylinder. The responses show the range of the targets to the transceiver. The purpose of this experiment is to try and resolve two relatively close by objects in range. The cylinder and the sphere are placed at the distance of almost 1 m apart in range at the same azimuth (lateral) position. It can be seen from the range profile shown in Fig. 3.15 that the responses from the objects are resolved in range. The amplitude of the responses indicates the intensity of the backscattered signal from both

objects. This is evident by comparing the simulated RCS of a cylinder and sphere shown in Fig 3.16 and Fig.317 respectively.

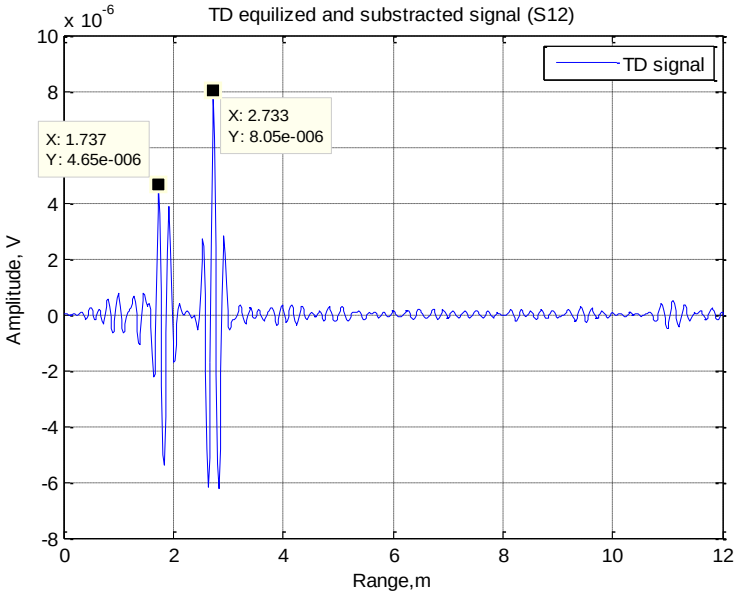

Figure 3.15: Range profile of the sphere and cylinder at about 1.6 m and 2.7 m from the transceiver.

3.3.4.1 RCS of a cylinder and sphere

Fig. 3.16(b) shows the simulated monostatic RCS of a PEC cylinder with the height of 17 cm and diameter of 13 cm at the operating frequency of 7.5 GHz. The simulation is made by a CST Microwave Studio simulation environment. The simulation movement is made in Z-Y plane shown in Fig. 3.16 (a). It is evident that at the grazing angle of 5 ° the RCS of the cylinder is below -30 dBm^2. At the height of about 80 cm at grazing angle of about 5°, the incident waves encounter the edge of the cylinder which has a small RCS due to its sharp shape. However, the RCS of the sphere is uniform and independent of the incident angle. At 7.5 GHz it is about -12 dBm^2 shown in Fig.3.17. This explains the smaller amplitude of the received signal from cylinder in comparison to the sphere in range profile plotted in Fig.3.15.

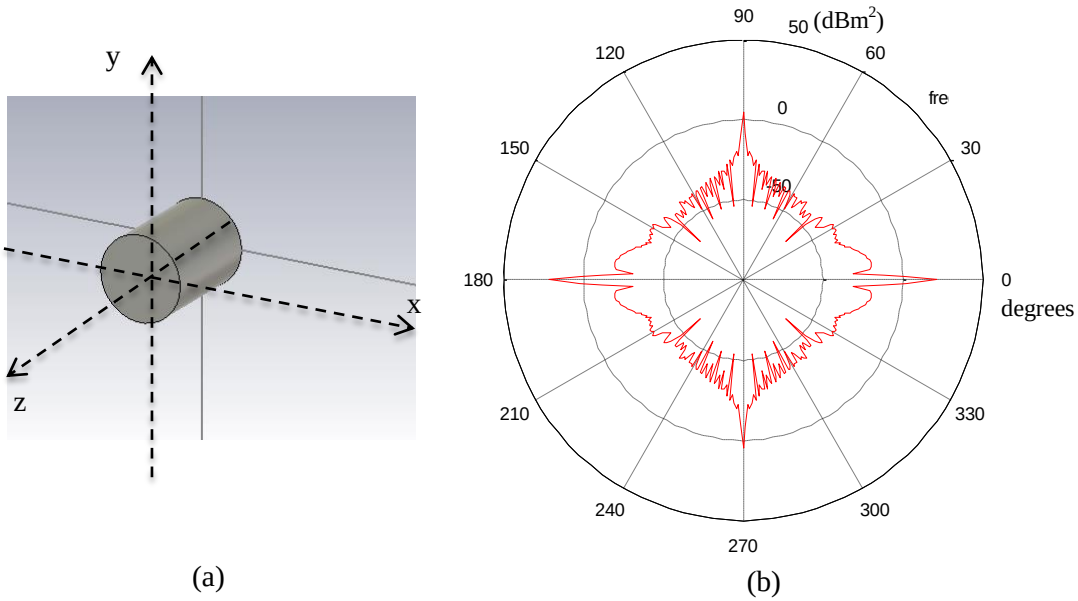

(a) (b)

Figure 3.16: The simulated monostatic RCS of a PEC cylinder at the frequency of 7.5 GHz

Fig. 3.17 shows the monostatic RCS of a PEC sphere at operating frequencies of 7.5 GHz, 65 GHz and 75 GHz. The simulation is made by a CST Microwave Studio simulation environment. The radius of the PEC sphere is 0.16 m. Therefore the simulation is performed at the frequencies corresponding to the optical scattering, when wavelength is much smaller than the effective dimension of the sphere. The RCS is thus defined solely by the projected area of the sphere ($\sigma=\pi r^2$), and is independent of the operating frequency. This is evident in Fig. 3.17, because the plotted monostatic RCS at the three different frequencies are coinciding. The homogenous monostatic RCS confirms that sphere is an isotropic radar reflector. A metallic sphere is hence usually used as a canonical target for radar measurements as the orientation or positioning of the sphere corresponding to the transceiver does not affect radar reflection intensity measurements.

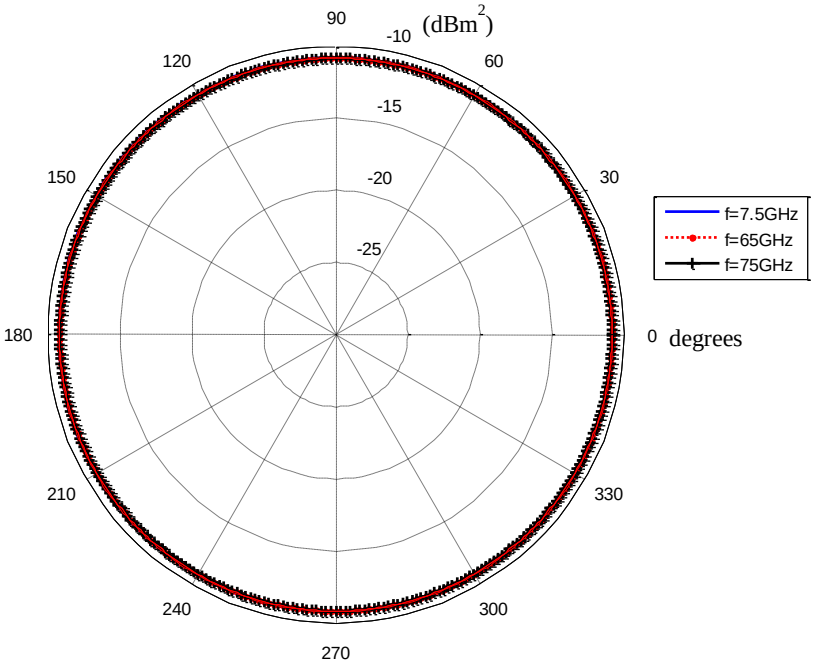

Figure 3.17: The simulated monostatic RCS of a PEC sphere at the frequencies of 75 GHz, 65 GHz and 75 GHz.

Fig. 3.18 shows the approximate bistatic RCS of a PEC sphere at operating frequencies of 7.5 GHz with the wavelength of $\lambda = 40$ mm , 65 GHz with the wavelength of $\lambda = 4.6$ mm and 75 GHz with the wavelength of $\lambda = 4$ mm. The incident angle is at 0 °. The shadow region of the sphere can be seen at 180° at all three frequencies. Even though the radar systems discussed in this study are monostatic, the bistatic radar cross section simulation demonstrates the shadow region of an arbitrary object. As discussed in section 2.2.5, the shadow region of relatively large objects can be used to detect and classify them. This will be demonstrated in the imaging results presented in chapter 6.

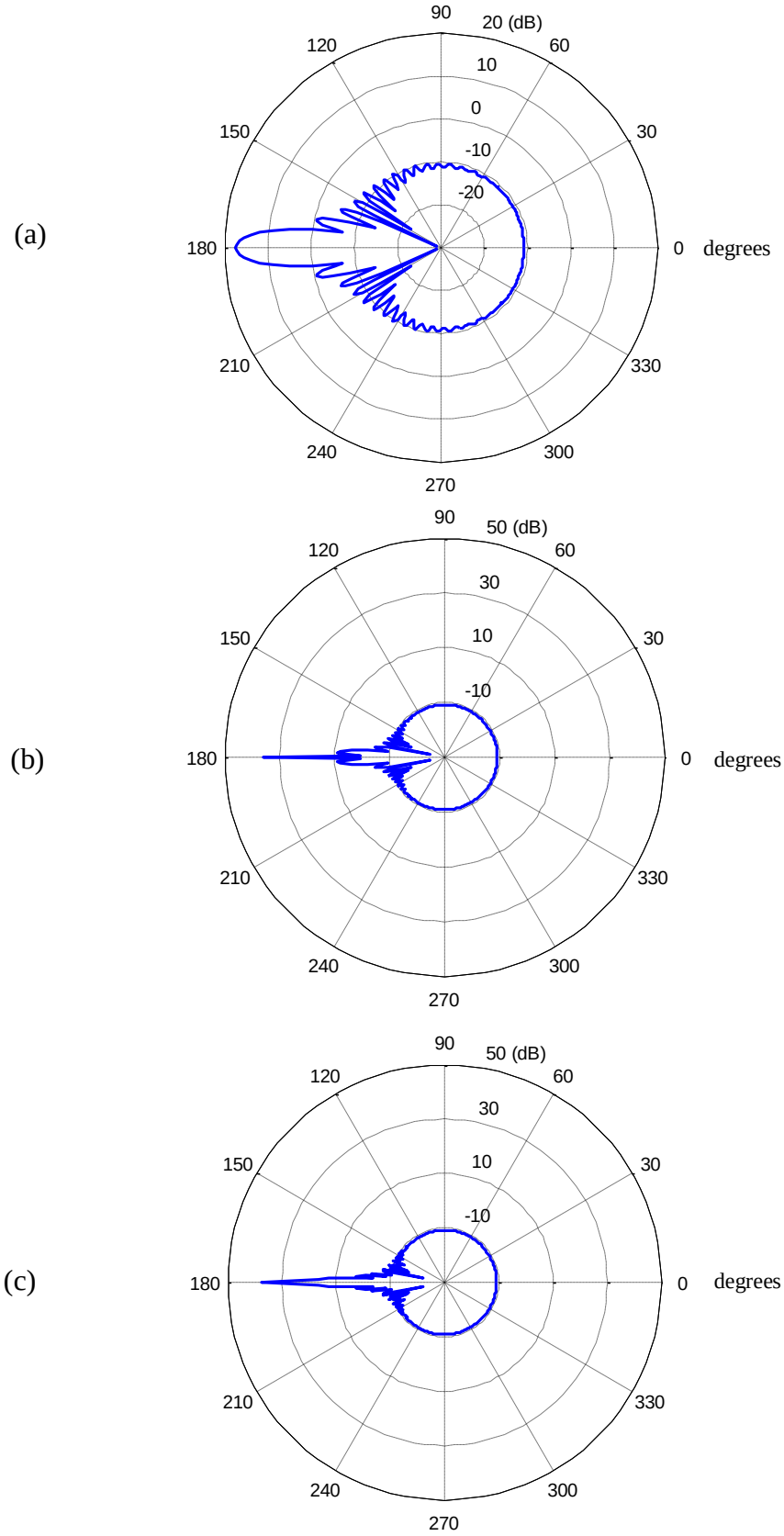

Figure 3.18: Simulated bistatic RCS of the PEC sphere at the frequency of (a) 7.5 GHz (b) 65 GHz and (c) 75 GHz

The experiment has been repeated with two bricks representing real-environment obstacles, which were positioned at distances of 1.6 m and 3.8 m from the transceiver. The purpose of this experiment is to demonstrate the effect of path loss on the amplitude of the received signal. The two bricks are relatively identical and are placed at the same lateral position (z=0). Fig. 3.19 shows the range profile of the two bricks. It is evident that the amplitude of the response from the further brick is smaller due to the propagation loss.

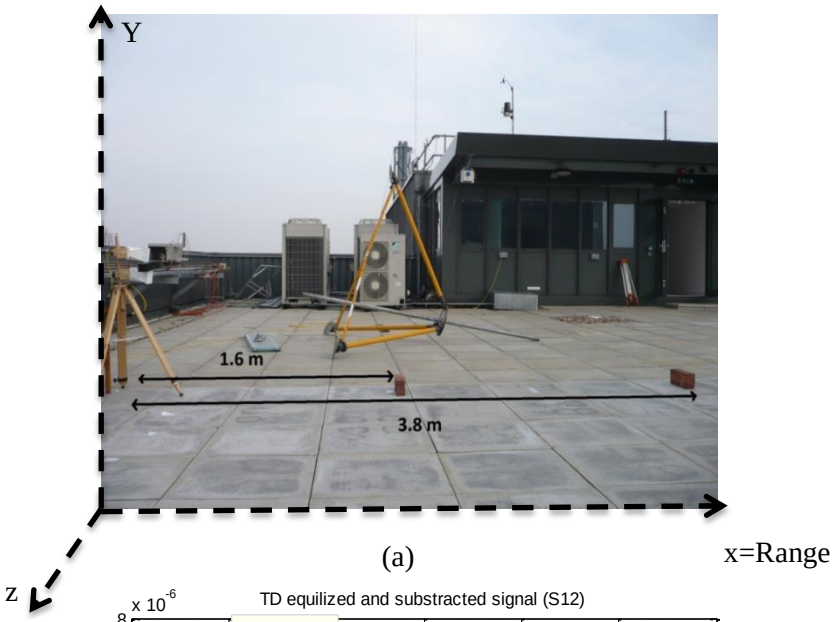

(a)

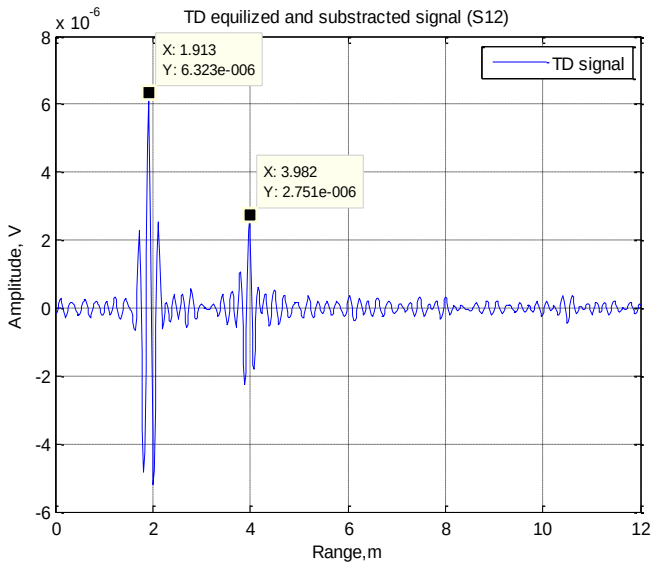

(b)

Figure 3.19: (a) Two bricks at about 1.6 m and 3.8 m from the transceiver. (b) Time domain responses from the two bricks.

3.4 2D Imaging (Image Formation)

In this set of experiments, the aim is to produce a 2D image map of the objects in front of the antennas by placing the range profiles next to one another in the order they were collected. As was discussed before a narrow azimuth beam antenna is required in order to illuminate a different portion of the scene at each scan angle which then will be merged to deliver a continuous image of the scene. The Q-par Angus antenna which was used so far, has a relatively wide azimuth beamwidth (40°). It was therefore replaced by a custom made horn antenna that has a narrower beam (12°) which is shown in Fig. 3.20(b). In this initial set of experiments, the aim is to move the antenna beam in azimuth in order to imitate the translation motion of the antenna with respect to the stationary objects (see Fig. 3.21) in order to produce an azimuth-range image map. In order to investigate a different antenna platform height in comparison to the pervious set of measurements, the height of the antennas is chosen to be 1.7 m; all other radar parameters are the same as described in section 3.3.3.

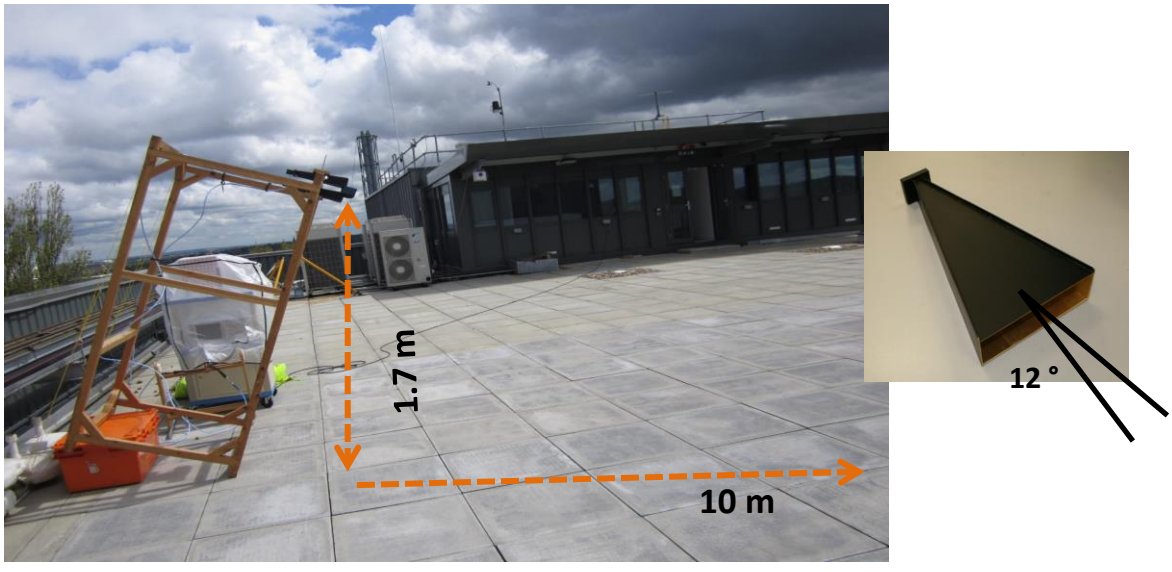

(a) (b)

Figure 3.20: (a) Topology of the measurement, antenna height 1.7 m (b) Q-par Angus UWB antennas with 40° azimuth beam width, (c) In house made antennas with12° azimuth beamwidth.

Fig. 3.21 shows the topology of the experiments corresponding to the scene of Fig. 3.20 (a). The azimuth resolution on the ground is calculated at distances of 5 m, 7 m and 10 m which are equal to 0.56 m, 0.75 m and 1.07 m respectively. The transceiver has been shifted along the azimuth (z) to produce the two dimensional (range, azimuth) image map of the illuminated scenario.

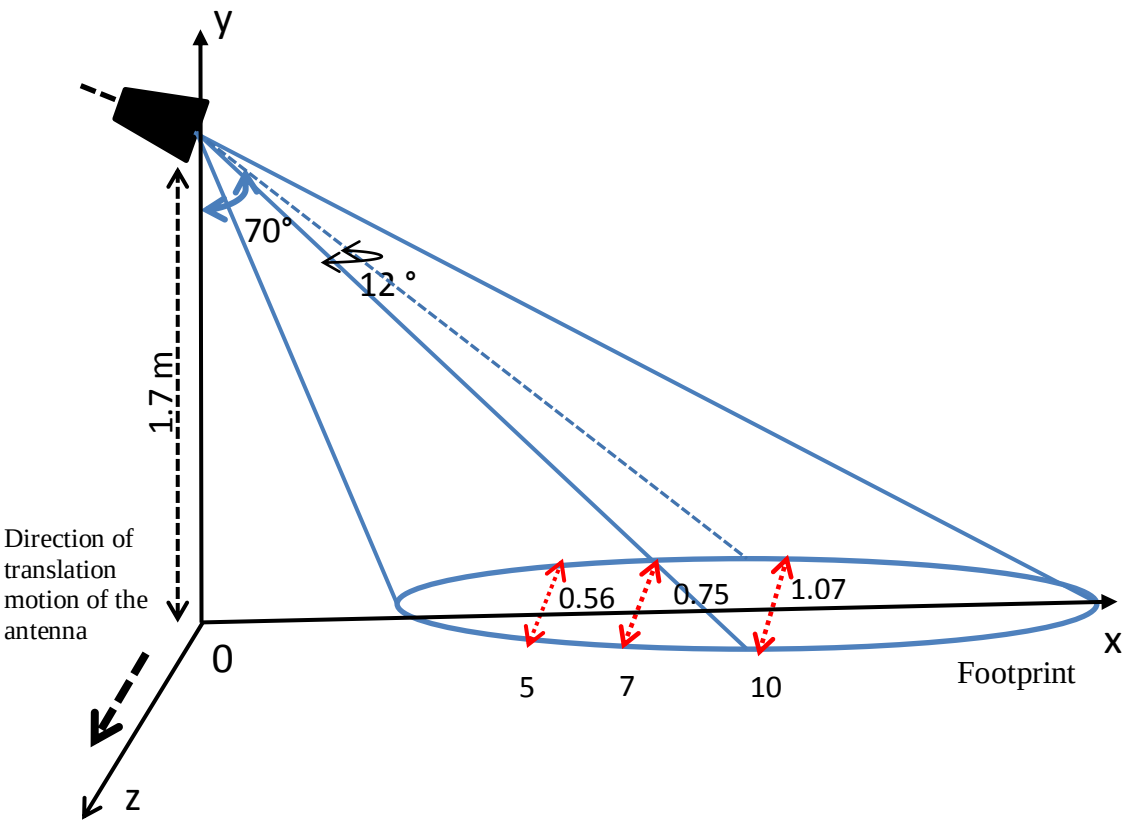

Figure 3.21: Topology of the experiments corresponding to Fig.3.17 (a). Antenna grazing angle is equal to 20°.

The azimuth beamwidths of the antennas are 12° corresponding to the azimuth resolution of 0.75 m on the ground at 7 m from the transceiver. Fig. 3.21 shows the range-azimuth image map of a brick placed at 7 m form the transceiver which was moved in steps of 0.5 m in azimuth (along the z) in Fig.3.22. Four resolution cells are created according to the step size. In the first cell, the brick is within the main beam of the antenna where the maximum backscattering is expected. As the transceiver moves in azimuth, the brick will be in the side

lobes of the antenna and therefore the smaller reflection intensity is seen on the images. In the last resolution cell beyond 1 m, the brick is outside the sidelobes of the antennas and therefore brick is not visible on the image map in the last azimuth resolution cell.

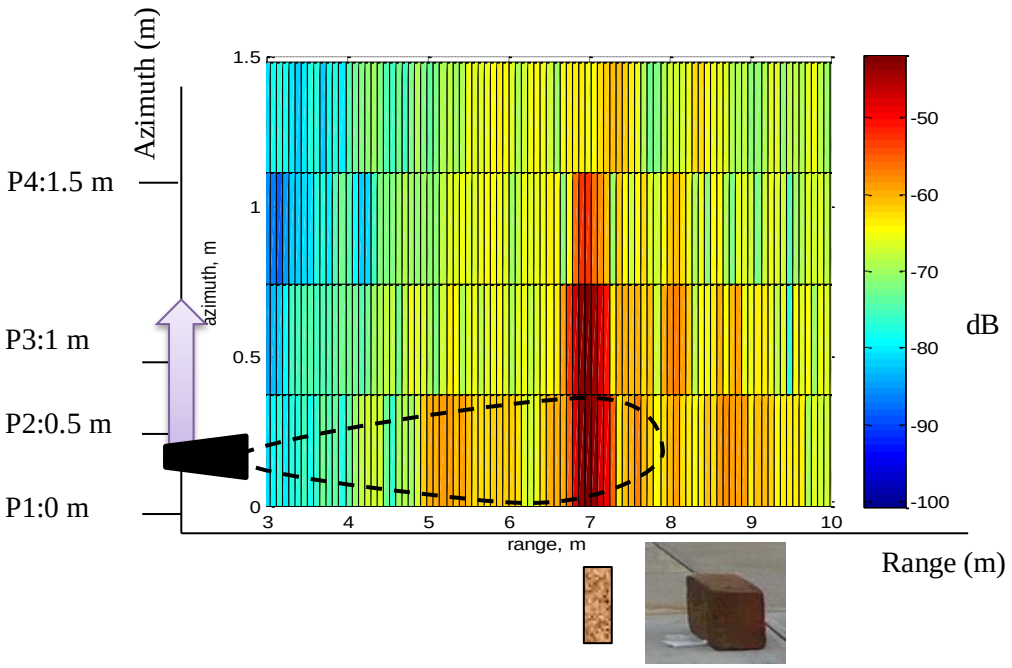

Figure 3.22: Two dimensional range-azimuth image map of the reflection from a brick at 7 m from the transceiver.

3.4.1 Time domain gating

Time gating is used to remove the effects of unwanted responses outside the range of interest. Gating in the time domain is achieved by filtering the frequency domain signal. Gating can be thought of as multiplying the time domain response by a function with a value of one over the region of interest, and zero outside this region [68].

Practically, time gating can be achieved by applying a band-pass filter to the frequency domain signal. It is important to choose the low and high cut off frequencies accurately in order to achieve the desired time region. High frequency components represent the reflections from further distances, while the low frequency components represent the nearby objects.

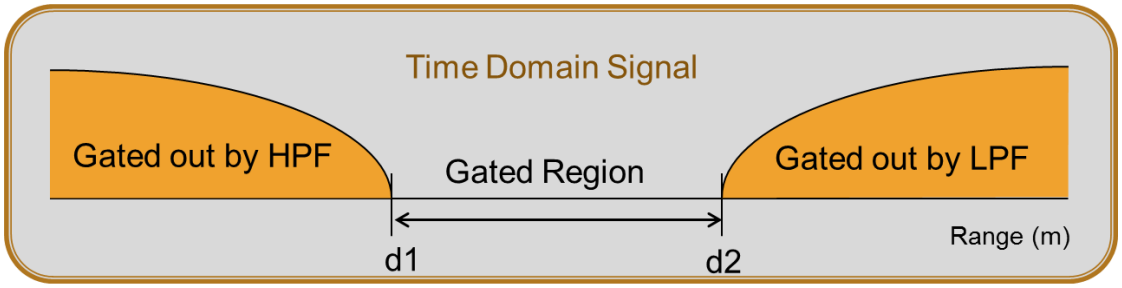

Figure 3.23: Time gating could be done by applying a band pass filter to a frequency domain signal.

Fig. 3.24 shows the time gated image presented in Fig. 3.22 as an amplitude-range-azimuth map. As can be seen, the response from the brick is prominent because all the unwanted responses outside the region of interest (3-10 m) are removed.

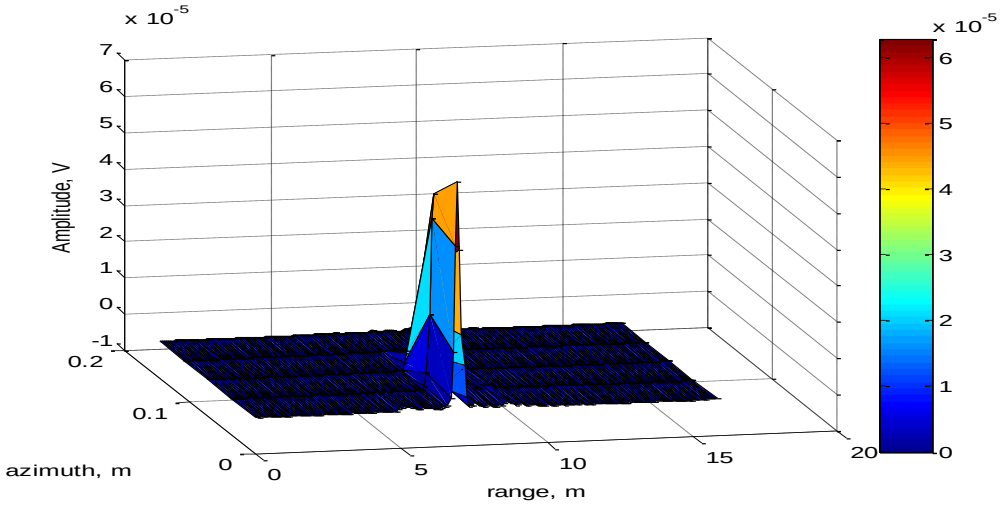

Figure 3.24: 3D representation of a time gated response of a brick at 7 m; time gated from 3 m to 10 m.

3.4.2 Imaged objects and RCS comparison

Fig. 3. 26 represents a 2D azimuth-range image map from a cereal bowl at 5 m, and a brick at 7 m with respect to the reference plane of the transceiver. The transceiver is shifted along the azimuth in steps of 0.5 m. At the first three offset positions up to 0.8 m azimuth offset, both the brick and the bowl are detected within the main beam or side lobes of the antenna and are therefore visible on the image map as areas of high intensity. Beyond about 1 m offset

position, both objects are within the antenna side lobes. The brick becomes visible at the azimuth offset of 1.2 m.

Fig. 3.25 shows the peculiarities of reflection expected for the brick and the bowl related to their shapes. The brick backscatters a larger amount of the incident energy towards the transceiver in comparison to the bowl. The brick therefore has a larger backscatter RCS, and it results in a higher intensity area on the image map. The analytical maximum RCS of the brick and the bowl can be estimated when considered as a flat plate and as a half sphere respectively. The maximum RCS of a PEC flat plate is estimated using equation (3.9):

$$\sigma_{FlatPlate} = \frac{4\pi a^2 b^2}{\lambda^2} \tag{3.9}$$

where a and b are the width and height of the flat plate (brick), respectively. The maximum RCS for the brick is thus around 4.5 m^2 (6.5 dBm^2). The maximum RCS of the bowl is estimated as 0.07 m^2 (-11.5 dBm^2) (according to $\sigma_{sphere} = \pi r^2$). It is evident that the brick has a much larger RCS than the bowl due to its shape. As can be seen in Fig. 3.26, at the azimuth offset position of 30 cm, the amplitude of the reflection from the brick is around -43 dBV, and the amplitude of the response from the bowl is about -60 dBV. It is noteworthy that the brick is further from the transceiver than the bowl, and the loss factor is not considered in this case.

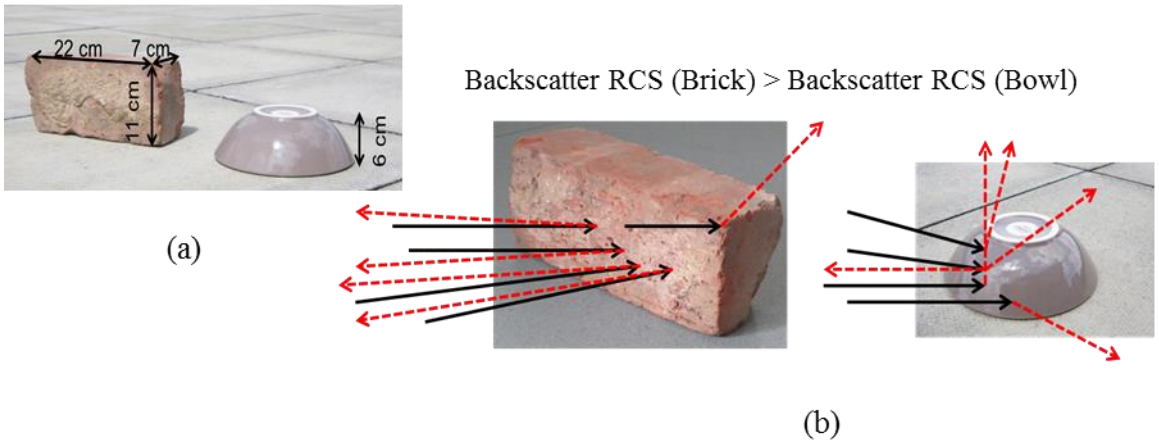

Figure 3.25: (a) Brick and a ceramic cereal bowl are used as natural targets (b) the sketch of signal scattering of the brick and the bowl due to their shapes

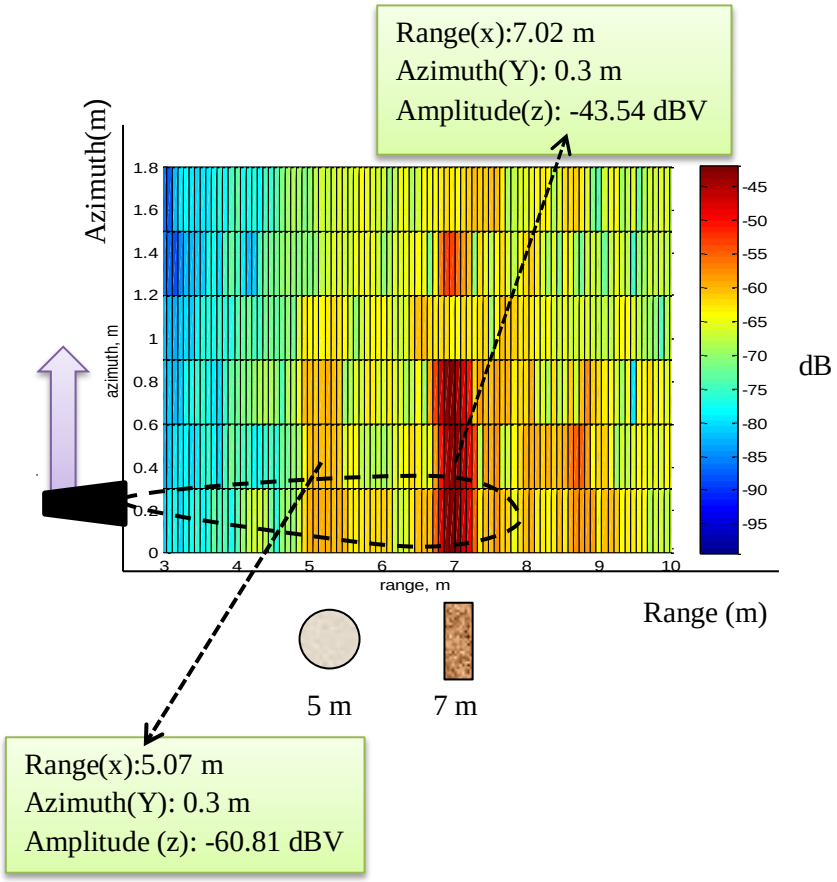

Figure 3.26: 2D azimuth-range image map of the reflection from a ceramic bowl at 5m and a brick at 7 m from the transceiver.

3.5 Summary

This chapter introduced a radar system built using available instrumentation and components in-house in order to analyse the basic method of image formation by beam scanning radar. Physical beamforming was introduced in order to produce a preliminary 2D range-azimuth image map. The range resolution was achieved by using a stepped frequency waveform. The azimuth resolution was achieved by using an antenna with relatively narrow azimuth beamwidth. In the next chapter, a high resolution radar system built with in-house components operating close to conventional automotive radar frequencies is described and its imaging performance is analysed.

4. 30 GHz Stepped Frequency Reference Radar

Overview- *This chapter introduces a radar system built from available instruments and components in house. They act as a prompt solution for creating reference radar operating around conventional automotive frequencies. The aim is to compare the images produced by this radar with the images formed by the radar system operating at 150 GHz which is introduced in chapter 5.*

The reference radar operates at 30 GHz. This frequency is chosen because the available antenna operates at 30 GHz which is close to the legacy 24 GHz short range automotive radar operating frequency. This antenna is used for both transmit and receive channels, which are isolated by a 2.5 GHz bandwidth circulator so that the configuration is monostatic. The waveform is stepped frequency, and is generated and logged by the VNA as discussed in the chapter 3. The VNA sweeps the frequency from 29 GHz to 31.5 GHz and delivers an overall bandwidth of 2.5 GHz.

4.1 Antenna Design

The in-house available antenna shown in Fig. 4.1 is a highly directional parabolic antenna operating at 30 GHz.

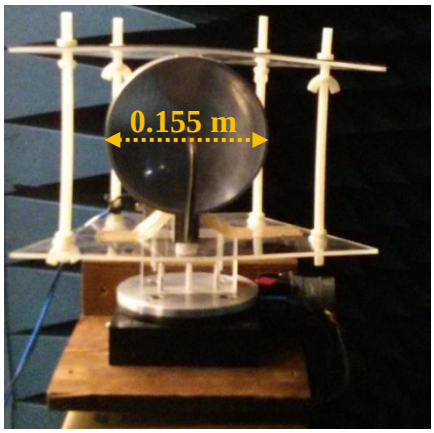

Figure 4.1 A directional parabolic antenna with a waveguide feed. The antenna is mounted on a turntable.

Parabolic antenna's diameter, *D*, is approximatly 0.155 m as shown in Fig. 4.1. Antenna's radiating Near Field (Fresnel) region (D_1) is estimated according to (4.1) [69]

$$D_1 = 0.62\sqrt{\frac{D^3}{\lambda}} = 0.4\,m \tag{4.1}$$

where λ is the wavelength. Parabolic antenna's Farfield (Fraunhofer) region (D_F) is estimated according to (4.2) [69].

$$D_F = \frac{2D^2}{\lambda} = 5.1\,m \tag{4.2}$$

The approximate azimuth and elevation beams of the parabolic antenna (H- and E-planes) are both measured in the range from -30° to +30°. Fig. 4.2 (a) shows the azimuth beam. The 3 dB beamwidth is found to be about 3.5 °, which provides an acceptable resolution for reference radar. The 3 dB elevation beamwidth shown in Fig. 4.2 (b) is also around 3.5 °, which is expected for a symmetrical antenna aperture. As described in chapter 3 wide elevation beamwidth is required to provide a desired footprint on the ground. The 3.5 ° elevation beam is not wide enough to provide the desired footprint 4 -100 m on the ground; the elevation beam should therefore be increased.

Let us find the required elevation beamwidth of the antenna to cover the specified antenna footprint starting from 4 m (R_{min}) from the transceiver (shown in Fig.1.3). The radar elevation, *H*, is chosen to be 80 cm above the ground according to the approximate mounting height of the radar in the vehicle's front bumper or grille area. The antenna tilt angle, θ, is about 5°. According to Fig.1.3, the 3-dB elevation beam, Θ_E, is calculated to be about 11°, using equation (4.3):

$$\Theta_E = 2\left[\arctan\left(\frac{H}{R_{\min}}\right) - \theta\right] \tag{4.3}$$

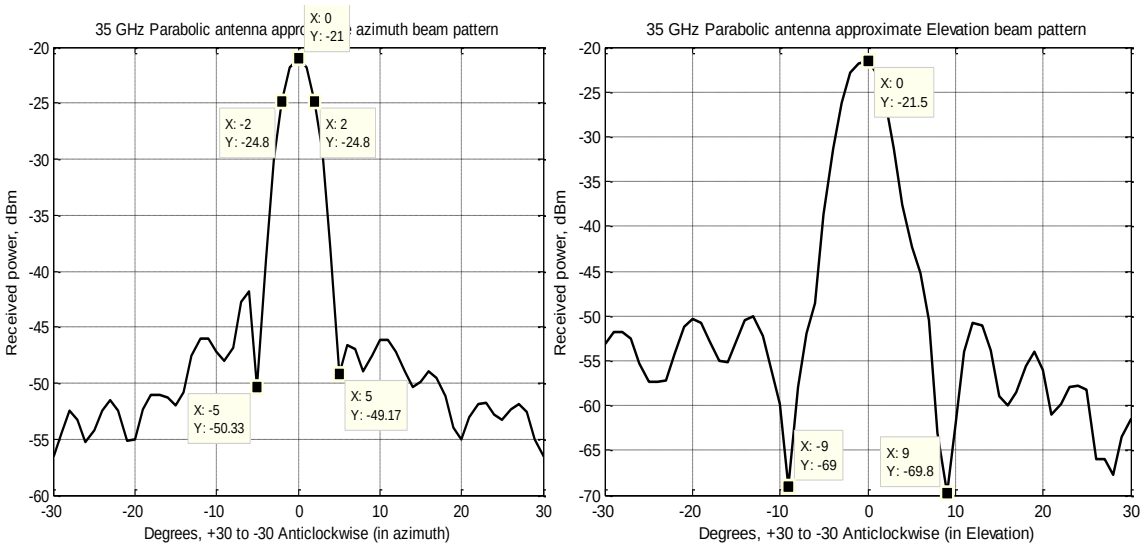

(a) (b)

Figure 4.2: Measured parabolic antenna pattern (a) H-plane (azimuth) (b) E-plane (elevation)

The beamwidth is defined by the effective size of aperture and the operational wavelength. In parabolic antennas, the 3-dB beamwidth (in Degrees) in a particular plane is defined by its effective dimension in this plane (d) and can be estimated using (4.4):

$$\Theta_E = \frac{\alpha * \lambda}{d} \tag{4.4}$$

where α is a coefficient that is different for every parabolic antenna. Thus in order to increase the beamwidth in elevation plane, d should be decreased.

In order to achieve the required elevation beam Θ_E, the required size of aperture is calculated using (4.4). α is found to be 49° for this parabolic antenna based on previous empirical measurements. Consequently (according to (4.4)), in order to achieve a 11°, 3dB beamwidth at 30 GHz (λ= 10 mm), the effective size of aperture in elevation should be 40 mm.

Therefore the parabolic antenna is tapered by covering part of the aperture with the magnetic absorbing material (see Fig. 4.3), leaving a parabolic sector of 40 mm wide. Fig. 4.4 shows the measured elevation beam; in this figure, the 3-dB beamwidth is 11.5°, which agrees with

the calculated value. The parabolic antenna is now called the sector parabolic antenna because it is tapered with absorber to have a smaller effective aperture size.

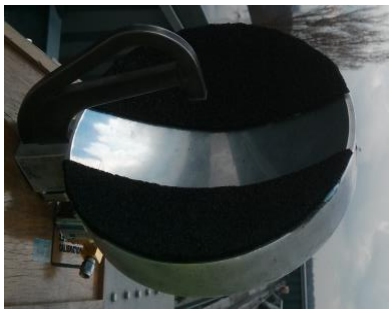

Figure 4.3: Parabolic antenna tapered with absorber

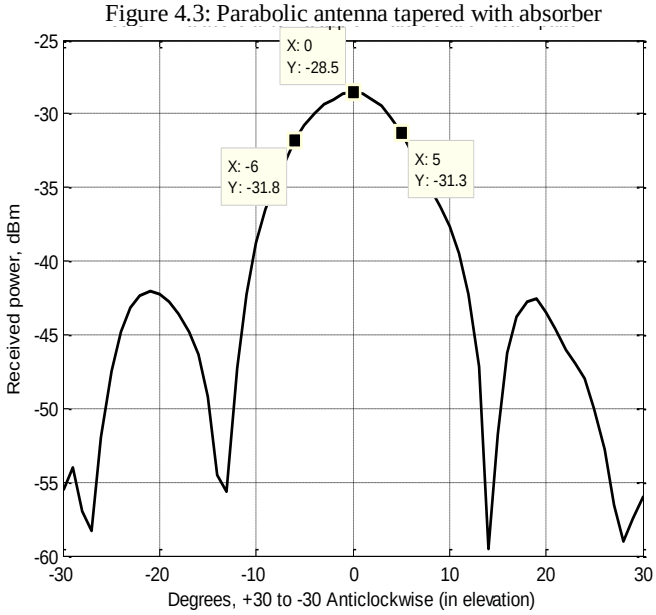

Figure 4.4: Measured sector parabolic antenna pattern in E-plane

In order to investigate the antenna's pattern deterioration from far to near field (Fresnel zone), the antennas H-plane pattern has been measured crudely at few range values from a calculated far field distance (within the dimensions of the anechoic chamber) down to 50 cm to the antenna which is shown in see Fig. 4.5. The pattern remains more or less the same until the distance of 1.4 m from the antenna, which is within the calculated nearfield region.

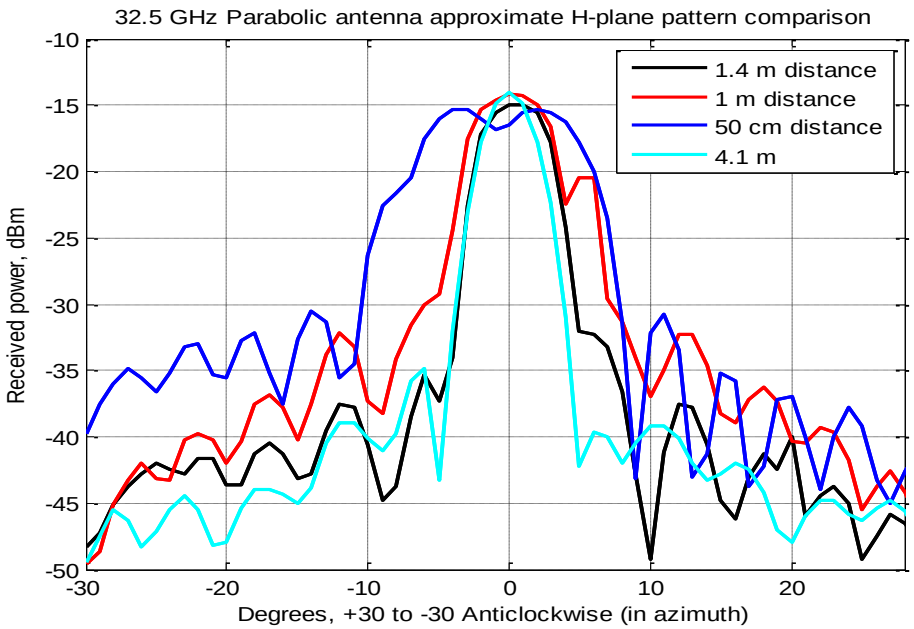

Figure 4.5: Measured parabolic antenna's H-plane (azimuth) beamwidth at different distances to the antenna

4.2 Tx and Rx isolation for Monostatic radar configuration

The sector parabolic antenna is used for both transmitting and receiving signals. Therefore the transmit and receive channels must be isolated. The circulator is a three-port RF microwave device which can fulfill this task. The scattering matrix for an ideal circulator is shown in (4.5):

$$[S] = \begin{bmatrix} 0 & 0 & 1 \\ 1 & 0 & 0 \\ 0 & 1 & 0 \end{bmatrix} \tag{4.5}$$

The circulator scattering matrix shows that power flow can occur from ports 1 to 2, 2 to 3, and 3 to 1, but not in the reverse direction as shown in Fig. 4.6. The opposite circulatory can be obtained by transposing the port indices; a circulator can therefore be clockwise or counter clockwise. In practice, this result can be produced by changing the polarity of the ferrite bias field in ferrite-based circulators [25].

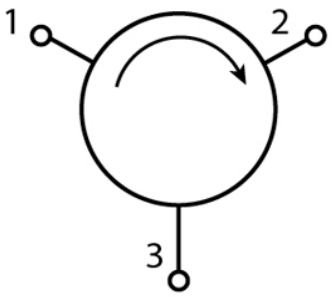

Figure 4.6: Clockwise circulator

The S-parameters of a circulator with a resonant frequency of 32.5 GHz has been measured. Fig.4.7, Fig. 4.8 and Fig. 4.9 show the measured S-parameters of the circulator. In order to measure the isolation of each two ports of the circulator, the third port is matched with a standard wideband (VNA calibration kit) load. The circulator has been measured with Vector Network Analysers: R&S ZVA 67 and HP 8722D 50 MHz-40 GHz in order to compare the results and to ensure the maximum isolation between transmit and receive channels.

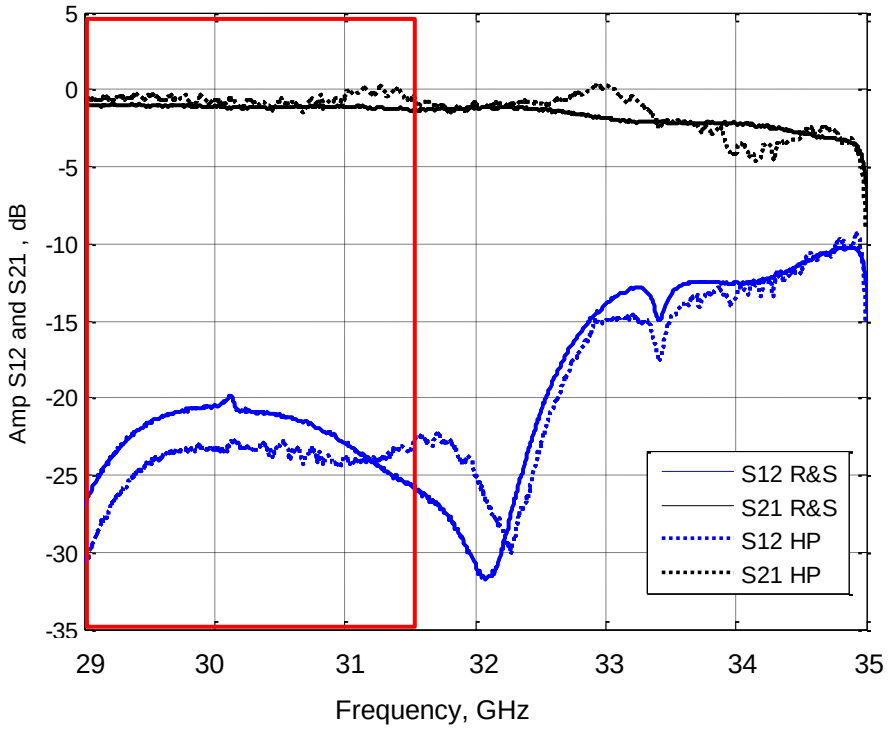

Figure 4.7: Comparison of S12 and S21 magnitudes (in dB) measured by Vector Network Analysers: R&S ZVA 67 GHz and HP 8722D 50 MHz-40 GHz

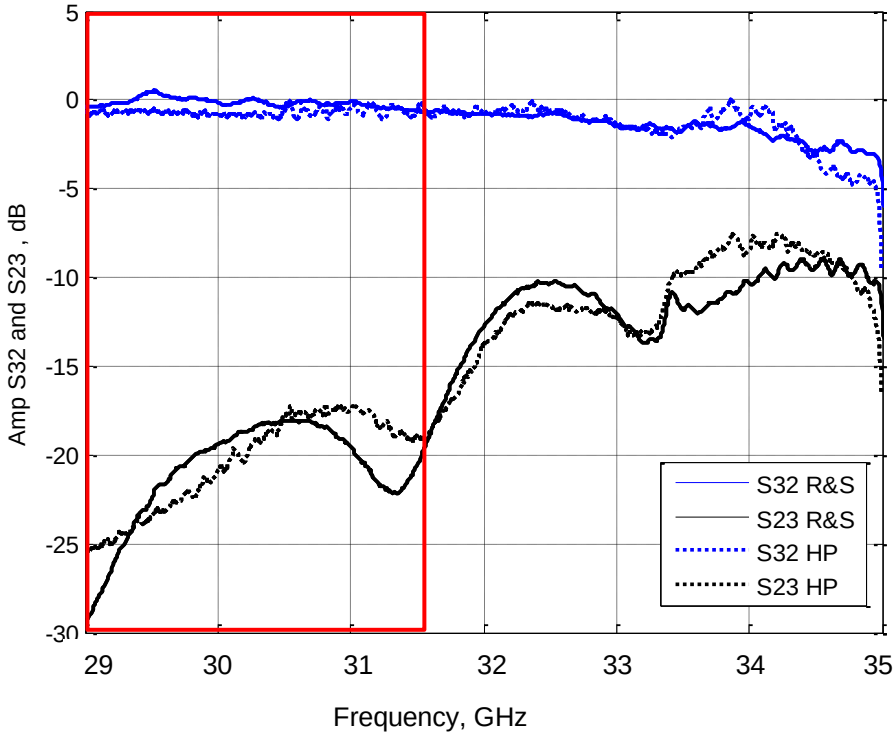

Figure 4.8: Comparison of S32 and S23 magnitudes (in dB) measured by Vector Network Analysers: R&S ZVA 67 GHz and HP 8722D 50 MHz-40 GHz.

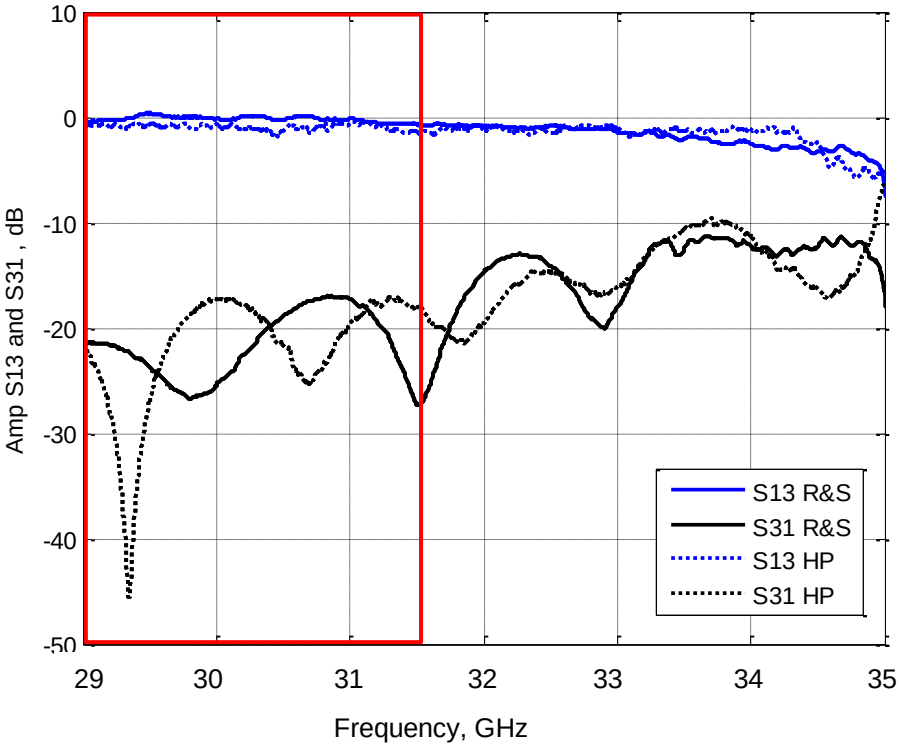

Figure 4.9: Comparison of S13 and S31 magnitudes (in dB) measured by Vector Network Analysers: R&S ZVA 67 GHz and HP 8722D 50 MHz-40 GHz.

In can be concluded that the S-parameter measurements with R&S ZVA 67 GHz agrees with the results from HP VNA. According to the measurements shown in Fig.4.7-4.9, the isolation of about 17-20 dB can be achieved within the frequency band of 29-31.5 GHz. The S-parameter measurement results demonstrate that the circulator is clockwise.

In Fig. 4.10, port 1 of the VNA is connected to port 3 of the circulator and port 2 of the VNA, which is the excitation port, is connected to port 1 of the circulator. The antenna is connected to port 2 of the circulator. When port 1 of the circulator is excited, the power flows to the antenna in order to transmit. According to Fig. 4.7, the isolation is less than -20 dB within the bandwith of 29-31.5 GHz, therefore there is a very little power going back to port 1. When the antenna is operaing as a receiver, the power flows in the circulator from port 2 to port 3. The received channel is therefore isolated from the transmit channel by about 17-20 dB within the the bandwidth of 29-32.5 GHz which is acceptable for the radar system under study.

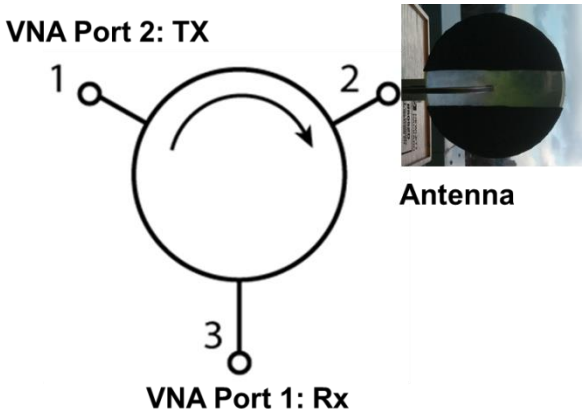

Figure 4.10: Circulator connected to the antenna

4.3 The 30 GHz radar system

Fig. 4.11 shows the system configuration. The VNA (HP 8722D 50 MHz-40 GHz) is used for transmitting, receiving and logging data. A laptop is connected to the VNA via GPIB for data acquisition. As described in section 4.2, the sector parabolic antenna is used both for the transmit (Tx) and receive (Rx) channels, and the circulator is used to isolate the Tx and Rx channels. The bandwidth is limited to 2.5 GHz because the circulator's bandwidth is 2.5 GHz. The waveform is a stepped frequency waveform sweeping from 29 GHz up to 31.5 GHz. The signal processing and image formation was done using MATLAB. There are 1601 frequency steps per each sweep that takes 1.8 s. No sweep averaging is used. The antenna is mounted on a turntable to provide the azimuth scanning. Table 4.1, summarises the parameters of the radar system introduced in this chapter.

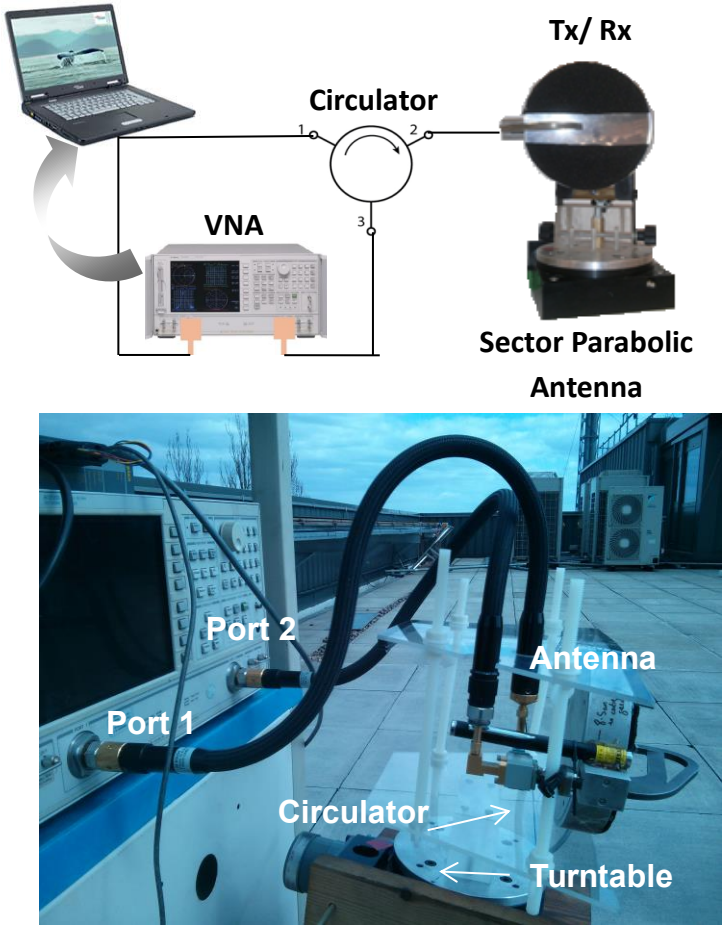

:

Figure 4.11: Radar system configuration

Table 4.1: Parameters of the stepped frequency radar system operating at 30 GHz

Parameter	**Values**
Transmitter	
Power output into antenna	1 mW(0 dBm)
Frequency sweep	29 – 31.5 GHz
Sweep bandwidth	2.5 GHz
Waveform	Stepped Frequency Waveform
Chirp Sweep Time	1.8 s
IF bandwidth	1 kHz
Number of samples	1601
Sweep type	Continuous Sweep
Antenna	
Antenna type	Sector parabolic (Tx and Rx)
Antenna aperture size	15.5 x 4 cm^2
Gain	20 dBi
Antenna beamwidth (2 way) azimuth(H-plane)	+/- 1.75°
Antenna beamwidth (2 way) elevation(E-plane)	+/- 5.5°
Polarization	Vertical
Tx/Rx isolation, provide by circulator	15-20 dB
Farfield	< 5.1 m
Receiver	
Noise figure	11 dB
IF bandwidth	1 kHz
Processor Unit and Digital Data	
Range resolution	6 cm
Number of range cells per sweep	4096 (2^{12} FFT points)
Operational range (Unambiguous range)	
Digital data output	Via GPIB-Frequency, *I* and *Q*
Circulator bandwidth	2.5 GHz

Fig. 4.12 shows different stages of imaging (from left to right): data collection with scanning antenna and data processing in order to form the 2D azimuth-range image map, as discussed in the chapter 3. The intensity of the image is the ratio of the absolute received power to the transmitted power (S_{12} or S_{21}) in dB. The signal processing also includes applying a threshold to the image. In the image shown in Fig. 4.12 for example, a -90 dB threshold is applied. Three reference targets are visible on the image map.

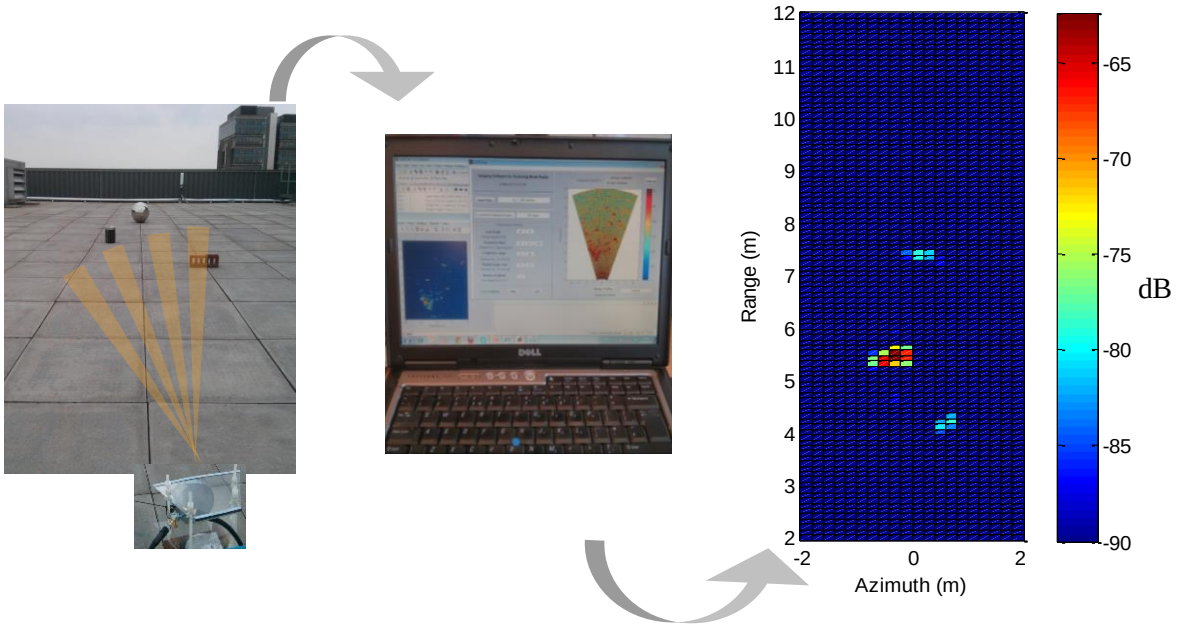

Figure 4.12: Radar imaging process

In all the experimental results presented in this chapter, the antenna elevation *H* is set to 80 cm which is approximately as high as an arbitrary vehicle bumper (see Fig.1.3). The height is measured up to the midpoint of the antenna. The grazing angle or antenna tilt angle (θ in Fig.1.3) is around 5°.

4.4 Range and azimuth resolution

The range resolution is defined by the sweep bandwidth. The range resolution of the radar with bandwidth of 2.5 GHz using equation (2.4) is about 6 cm.

The azimuth resolution is calculated using equation (4.6) (See Fig. 1.3):

$$R_c = 2R\tan\left(\frac{\Theta_H}{2}\right) \tag{4.6}$$

where, R_c stands is the azimuth (cross-range) resolution. R is the range and Θ_H is the 3 dB H-plane (azimuth) beamwidth. According to (4.5), the azimuth resolution at the distance of 10 m is 61 cm.

4.5 Experimental results

4.5.1 Scenario I

The performance of the imaging radar has been analysed by initial testing in controlled outdoor conditions with canonical targets. Fig. 4.13 shows an experimental scenario on the rooftop of the building of Electrical Electronic and Systems Eng. (EESE) School of University of Birmingham. Four identical trihedral corner reflectors and a standard rubber speed bump were positioned above the tiled concrete floor. The corner reflectors form a square of 1 m^2, with the centre at 5.4 m from the transceiver. The purpose of positioning the corner reflectors in such a configuration is to assess the resolution in range and azimuth. The rubber road bump with the total length of (3 x 90 cm=2.7 m) is placed at 7.4 m distance from the reference plane of the transceiver. The road hump is chosen as a target in this experiment, as it is a standard obstacle that could be seen on roads. The result of the experiments with 150 GHz using the same targets is found in chapter 6, section 6.3. The scene is scanned from

+20° to -20° counter clockwise with 1° steps. Table 4.2 shows the description of the objects used in the experimental scenarios shown in Fig.4.13 and Fig. 4.15.

Table 4.2: Description of the objects used in the scenario of Fig. 4.14 and Fig. 4.16

Target	***Dimension***	***Max RCS dBm^2 @ 30 GHz***
Tridehral corner reflector	14 cm (side)	12
Rubber 'hump'	2.7m (length) x 7.5cm (height)	N/A
Square concrete tile	60 cm (side) x 4.5 cm (depth)	< 20
sphere	radius=16	-11
Cylinder	Height: 17 cm diameter: 13 cm	4

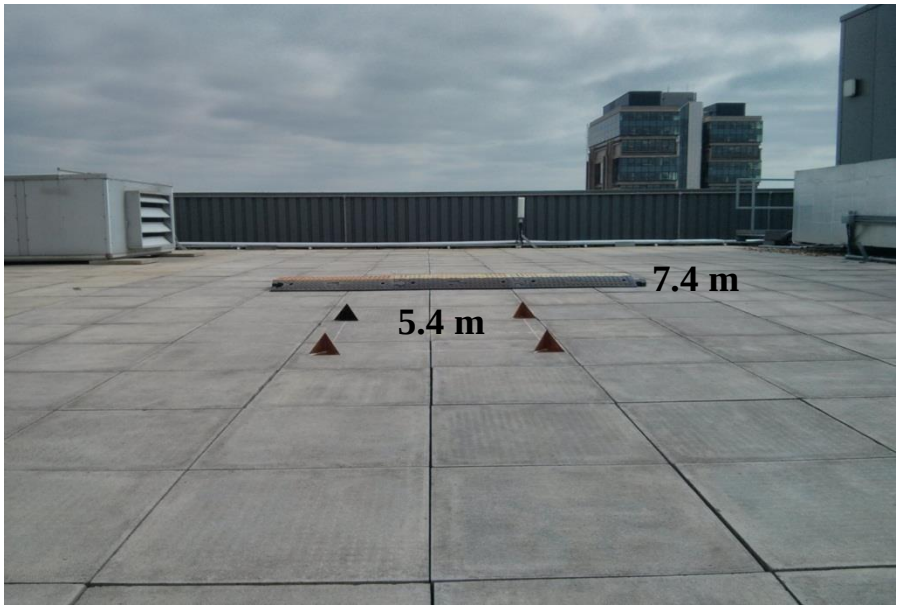

Figure 4.13: Four corner reflectors forming a square of 1m are positioned at 5.4 m from the radar and a rubber road bump placed at 7.4 m from the radar on the roof top of the EESE building, University of Birmingham

Fig. 4.14 shows the image map corresponding to the scenario of Fig.4.13. The intensity of the image is the ratio of the received power to the transmitted power (S_{12} or S_{21}) in dB. The range, the angular position, and the intensity of the return from each imaged object correspond to the scene of Fig. 4.13. The corner reflectors are clearly resolved in range and the distance from mid-point of the corner reflectors is about 1 m. However, they occupy more resolution cells in range than their actual size because of the high level of side lobes of the

large response from corner reflectors. The corner reflectors appear larger than their actual size in azimuth (i.e. occupying more space (resolution cells)) on the map than expected) owing to low azimuth resolution and being in one azimuth cell of about 30 cm at 5.4 m from the reference plane of the transceiver. This is the achievable range resolution by using an antenna with 3.5 ° beamwidth without using azimuth refinement methods. The resolution in azimuth can be improved by using an antenna with a narrower azimuth beam (for instance 1°). As the scene is scanned counter clockwise (from right to left), the metallic fan cover which is located on the far left hand side in the photo of Fig. 4.13, appears on the right side of the image. In other words, the image is the mirror of the scene.

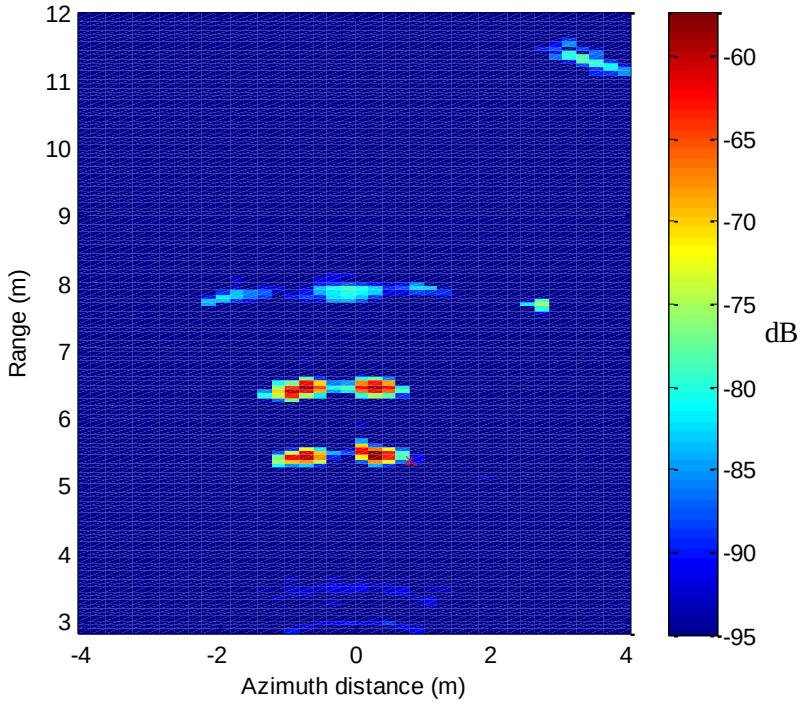

Figure 4.14: 2D azimuth-range image map corresponding to the image of the scene of Fig.4.13; a threshold of -95 dB is applied to the image.

4.5.2 Scenario II

Fig. 4.15 shows the rooftop of the EESE building covered with snow. This experiment has been set up after the snowfall in February 2013 in order to investigate how signals penetrate

or attenuate in obstruction media, such as snow. Road surfaces covered with snow can be experienced around the world and the radar system must be robust to such conditions. The thickness of the layer of the snow is measured around 5-6 cm. Two canonical targets, a metallic sphere and a cylinder were used for the purpose of calibration. A tile was removed from the ground to imitate a pothole. In Fig. 4.15 (a), a few footprints are also visible on the snow. Fig.4.15 (b) shows a sketch of the scenario with targets positioned relative to the radar. The scene is scanned from -10° to +10° clockwise with 1° steps. The measurement bandwidth from 29.75 GHz to 31.25 GHz is chosen according to the optimum circulator isolation band, and therefore in this case the range resolution is about 10 cm.

Fig. 4.16 shows the resulting image corresponding to the scene of Fig.4.15. The three targets are detected and their location on the map corresponds to the scene. The maximum estimated RCS of the targets used in the experiment can be found in Table 4.2.

The sphere and the cylinder appear larger than their actual size owing to low azimuth resolution. The most interesting feature visible on the image of Fig. 4.16 is the removed tile. The square shape created by removing a tile is recognisable in the image. Similar experiments have been done without any snow on the rooftop and the results are discussed in chapter 6, section 6.3. In the case of no snow, only the back edge of the tile reflects the energy back towards the receiver, and the rectangular shape of the space formed by the removed tile is not detected (see Fig.6.3 (b)). This is caused by the layer of snow being more absorbent and less reflective than the ground at the operating frequency of the radar. In the case of this experiment, the layer of snow is the background instead of the tile floor.

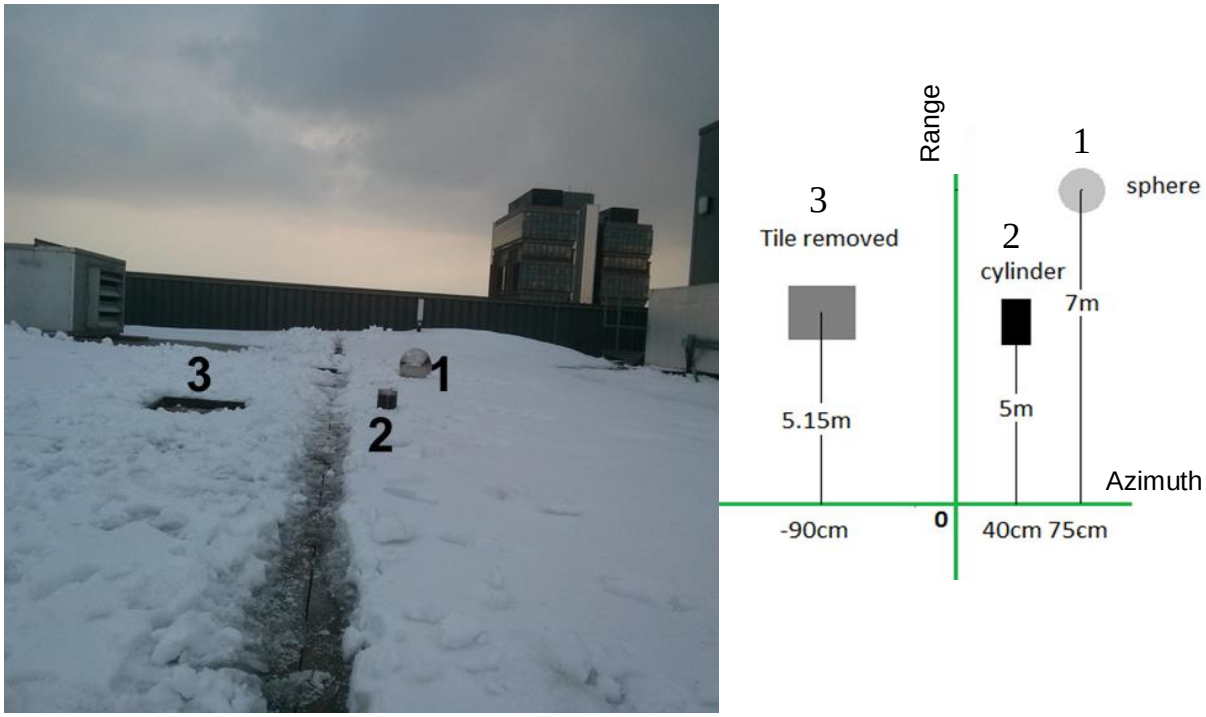

(a) (b)

Figure 4.15: Experimental scenario in snow on the roof top of EESE building at the University of Birmingham.

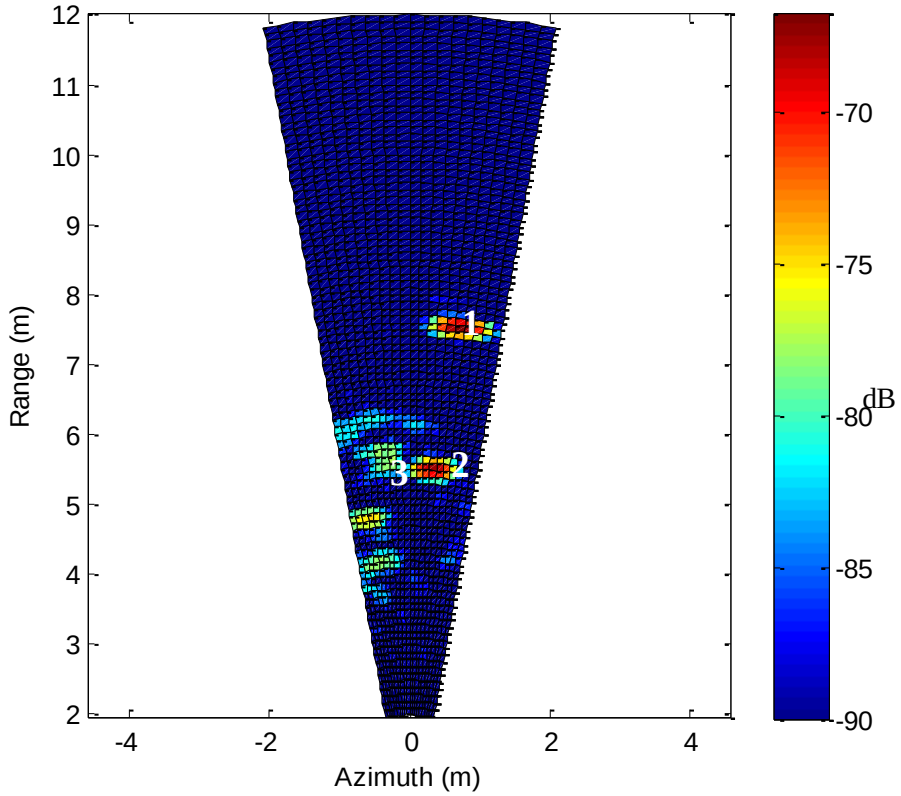

Figure 4.16 : Image corresponding to the scene of Fig. 4.15.

4.5.3 Scenario III

Fig. 4.17 shows a road scene on the campus of the University of Birmingham which is the first real road scenario discussed in this study. The purpose of this experiment is to assess the imaging capability of the radar system under study in real road scenarios with different obstacles and road features. Another reason is to evaluate its sensitivity to the surface roughness and texture for surface identification in addition to imaging of the obstacles in order to benchmark the 150 GHz radar system capabilities against the radar operating at conventional RF frequencies. The resulting images will be compared to the images made by using a FMCW radar operating at 150 GHz in chapter 6, section 6.4. Fig. 4.17 shows a road scene which includes potential obstacles for vehicles at different ranges: a metallic fence, a wall, a lamp post, small rocks and stones. As a reference, three canonical objects with known RCS (a sphere, a cylinder and a brick) are placed at 6 m, 9 m and 13 m respectively from the antennas. Fig. 4.18 shows the different obstacles which are used in the experiment and Table 4.3 provides a description of the targets used in the scenario of Fig. 4.17. The road is scanned from -40° to +40° clockwise with 2° steps. The measurement BW is 29-31.5 GHz. The radar image made by the 30 GHz radar is shown in Fig. 4.19. Fig. 4.19 shows that the range, the angular position and the intensity of the return from each imaged object correspond to the scene. The fence is visible on the left hand side of the image. However, the texture difference between asphalt, grass and rock salt spread on the asphalt observed in Fig. 4.17 is not distinguishable on the radar image of Fig. 4.19.

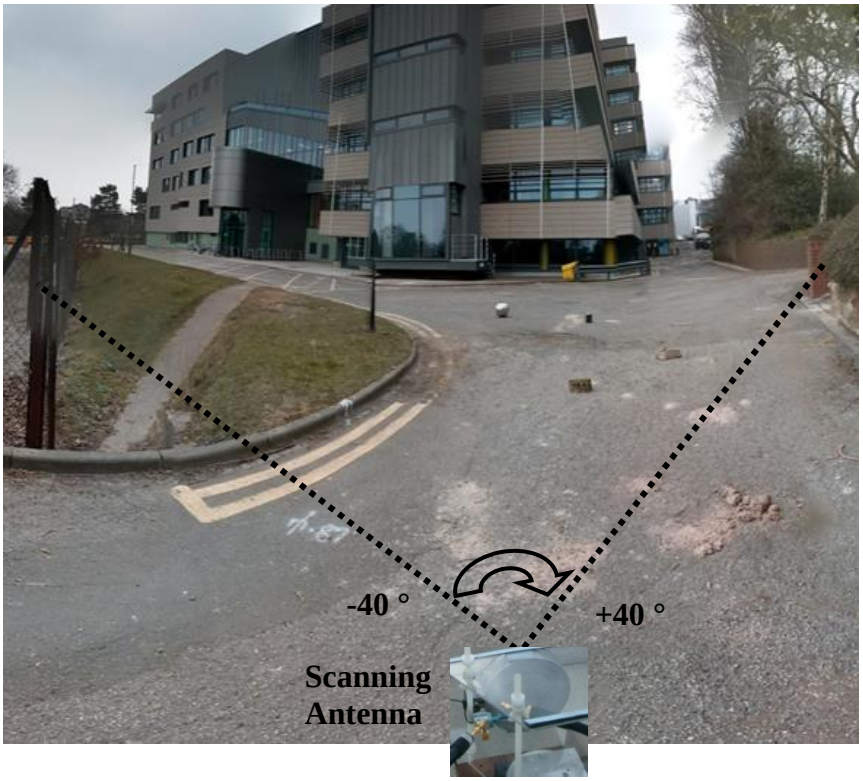

Figure 4.17: Road scenario with different obstacles. Targets consist of a brick at 5 m, a small rock at 6m, cylinder at 9 m, sphere at 9.6 m, lamp post at 7.2 m and a fence.

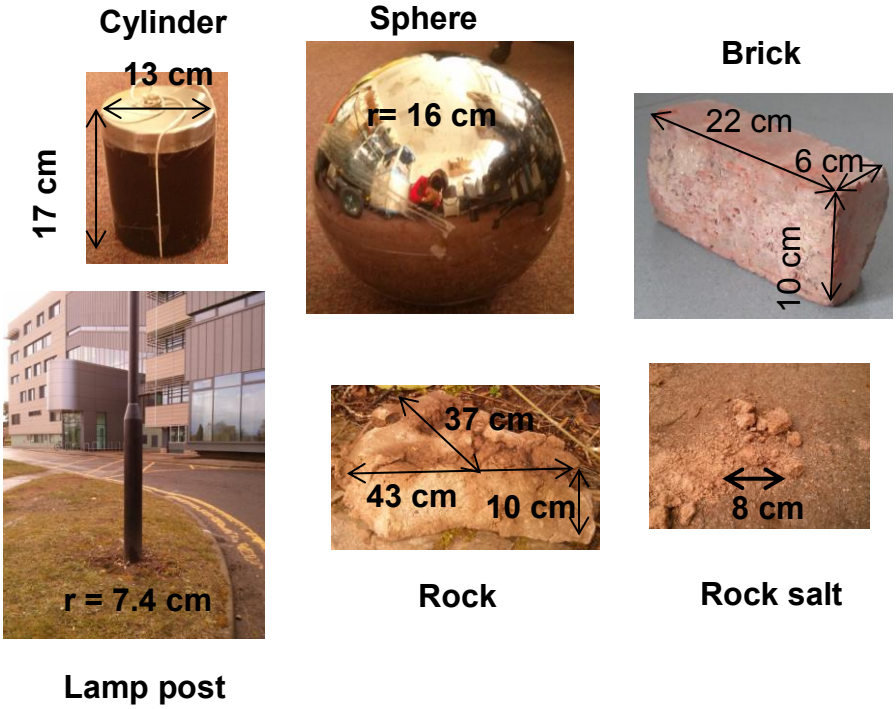

Figure 4.18: Different obstacles on the road and reference targets

Table 4.3: Objects used in the road scenario in Fig. 4.18

Object	Dimension, cm	Range, m	RCS, dBm^2
			30 GHz
sphere	radius=16	9.6	-11
brick	22 x10 x 6	5	19
lamp post	r = 7.4 cm, 3 m illuminated area	7.2	29
stone	≈ 43 x 37 x 10	6	NA
Cylinder	Height: 17 cm Base diameter: 13 cm	9	4

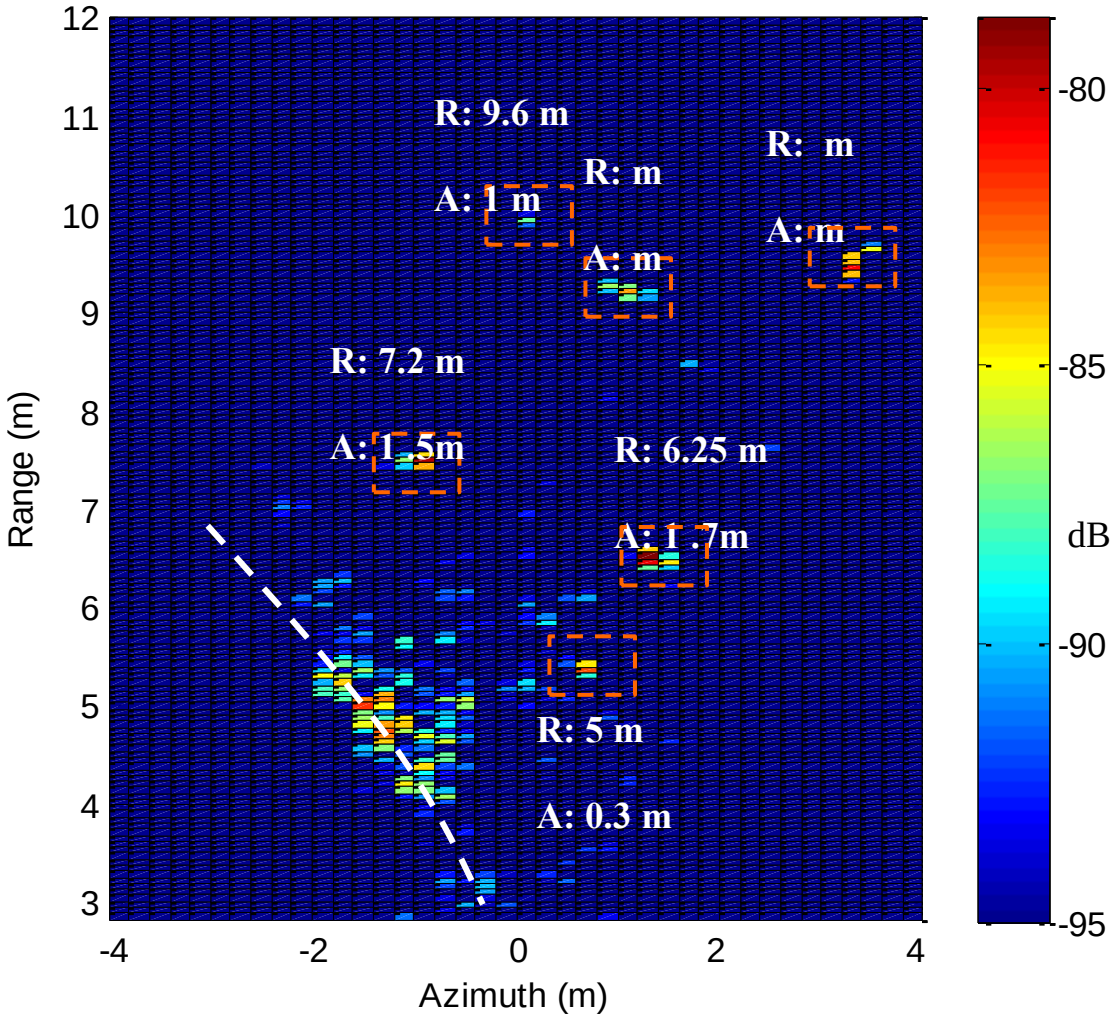

Figure 4.19: Image corresponding to the scene of Fig. 4.18 produced by 30 GHz stepped frequency radar. R is the range to the antenna and A is the Azimuth displacement from reference (the negative and positive values are not shown). Linear and squared features are added manually for visual indication of discriminated obstacles.

4.5.4 Scenario IV

Fig. 4.20(a) shows an experimental setup taken place on the Jaguar Land Rover sand testbed in Gaydon. This experiment is set-up to assess the potential of the mm-wave radar for profiling of an uneven surface. Sand is a potential terrain that a vehicle may experience in some parts of the world. Fig. 4. 20(a) shows the sand test bed with tracks on the sand created by the vehicle tire. The radar is positioned 4 m away from the wooden edge of the test bed in a parallel orientation toward the tracks. The purpose of this experiment is to image the profile of the sand (peaks and nulls). The road is scanned from -14° to +14° clockwise with 2° steps. Fig. 4.20 (b) shows the image produced by the 30 GHz radar system with the measurement bandwidth of 2.5 GHz. The parallel tracks on the sand are presented by parallel lines on the image map, where the intensity of reflections is defined by the topology of the road profile with respect to the aspect angle of the interrogating signal. The peaks produce a high intensity, while the dips appear as low reflective bands.

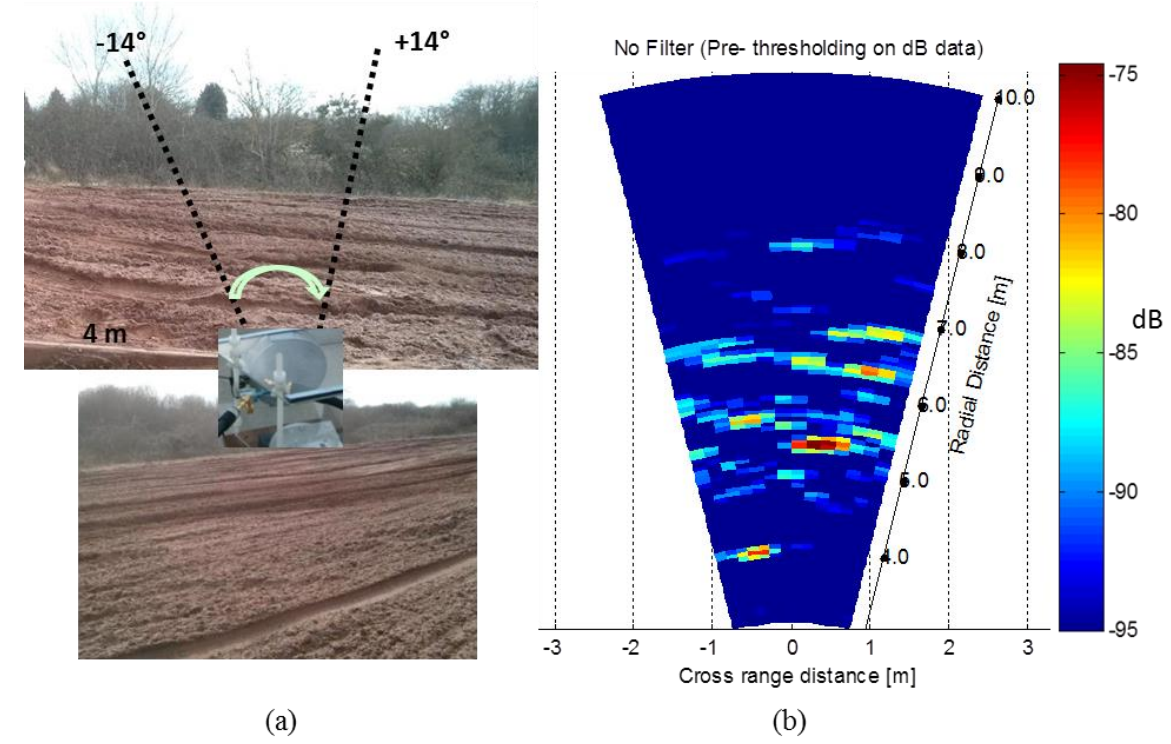

Figure 4.20: 30 GHz measurements on sand test bed in Gaydon; scanning angle is 28 ° with 2° steps.

4.6 Summary

This chapter described the design and operation of the reference radar system operating at 30 GHz built by in-house components and instruments. In order to achieve the fan-beam shape of antenna pattern required for imaging, the 30 GHz antenna pattern has been measured. Consequently, the aperture of the antenna was tapered to achieve a smaller effective aperture size and therefore a narrower azimuth beam width. A circulator was used to isolate, transmit and receive channels. Table 4.1, summarises the parameters of the radar system introduced in this chapter.

The imaging performance and robustness of the developed radar system has been examined in controlled laboratory conditions and unconstrained outdoor scenarios with different surfaces types such as asphalt snow and sand. In this chapter it is shown that while 30 GHz radar with 2.5 GHz bandwidth can provide reasonable images, it is still very far from delivering high resolution imagery and visually recognizable images, comparable to the images produced by electro optical cameras.

In chapter 6, the 30 GHz radar is used alongside the 150 GHz FMCW radar which is discussed in chapter 5, to compare the performance and demonstrate the advantages and specific features of low-THz imaging radar.

5. 150 GHz FMCW Radar Design

Overview- *In this chapter, an overview of the custom-made low-THz imaging radar prototype is presented. The radar is a portable laboratory system using a Frequency-Modulated Continuous Waveform (FMCW), sweeping over a 5 GHz bandwidth, from 145 GHz to 150 GHz. The peak output power to the antenna is around 15 mW so that the radar is far below the accepted RF safety thresholds [70, 71].*

The radar has been built in collaboration with ELVA-1, Millimetre Wave Division [72] from the available off-the-shelf components, except the antennas which are designed according to the required imaging radar performance, which will be explained in section 5.6.3. In this chapter all calculations are considered for stationary targets.

Fig. 5.1 shows a flow diagram of the high-resolution medium range imaging radar design for automotive applications. This flow diagram can be compared to section 1.3.2. Top-level requirements are shown in diamonds and enablers for achieving the requirements are shown in rectangles. The external influential factors are shown in circles. The imaging method of physical beam mapping is also included on the flow chart. The flow diagram represents how parameters are interlinked.

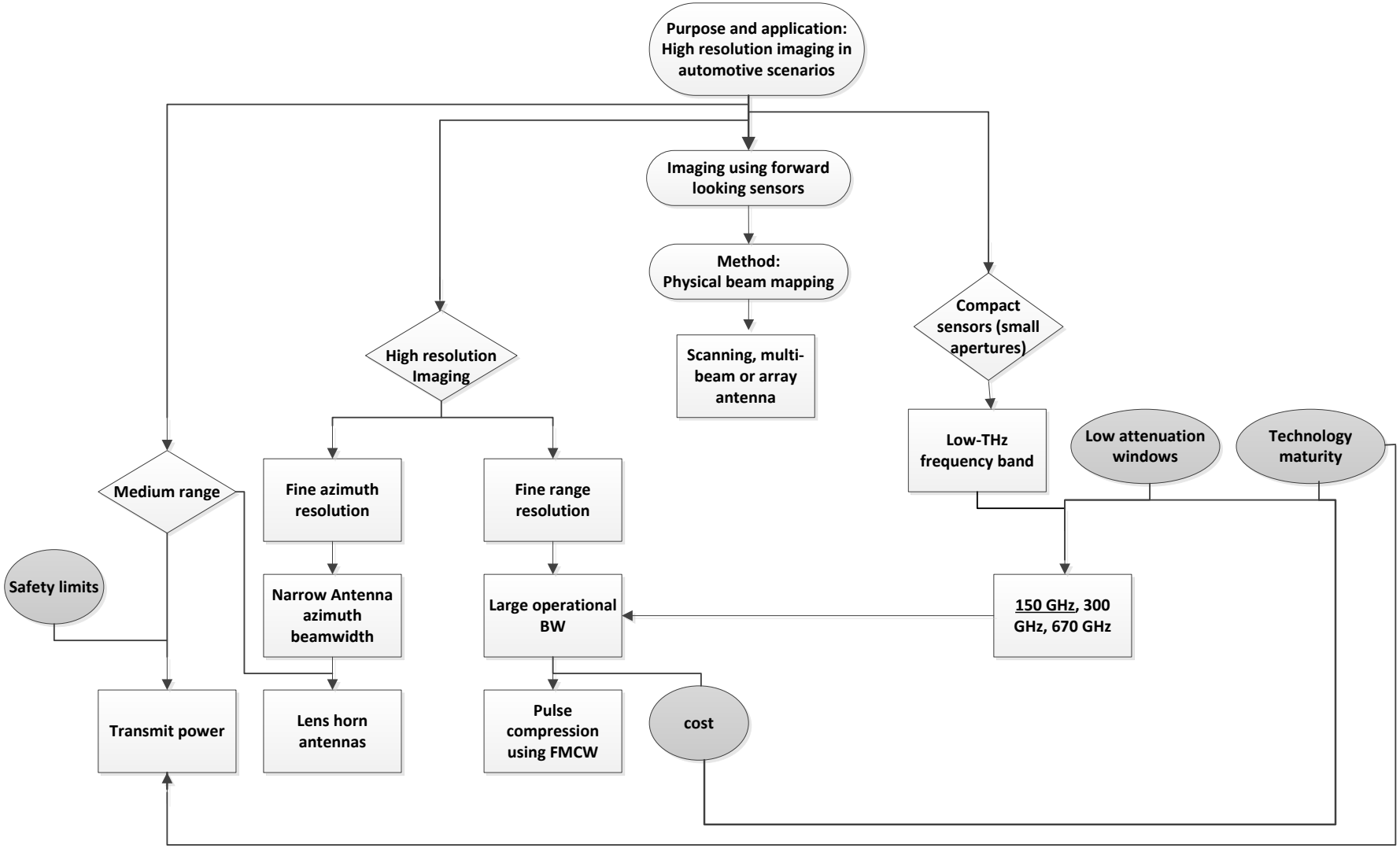

Figure 5.1 Flow diagram of the high-resolution medium range imaging radar design for automotive applications. Parameters in the circles represent external influential factors.

5.1 Radar equation

In order to consider the power budget analysis for this radar system, the radar equation is used. The radar equation or range equation is an expressive tool to describe a radar system performance as a whole. The radar equation is expressed either in maximum range (R_{max}) format or it could be written in received power format. Equation (5.1) shows the radar equation in terms of range [16, 19]. It is noteworthy that parameters in the radar equation are interlinked and the optimum value should be achieved for every parameter in order for the radar to be optimised as an integrated system.

$$R_{\max} = \left[\frac{P_t G_t G_r \lambda^2 \sigma \times t_{\text{int}}}{(4\pi)^3 S_{\min} L} \right]^{1/n} \tag{5.1}$$

where R_{max} *is the* maximum energetic range, P_r is the received signal power, P_t is the transmitted signal power, λ is the wavelength, σ is the radar cross section of the target, t_{int} is the integration time (time on target), L describes the system Losses, n is the path loss factor *($n=4$* for Friis free space model) [22] and S_{min} is the minimum detectable signal which is calculated according to equation (5.2).

$$S_{\min} = KT_0 B_n F_n \left(S/N\right)_{req} \tag{5.2}$$

where, K is the Boltzmann's constant, which is equal to 1.38×10^{-23} J×K^{-1}, T_0 is the ambient temperature (in degrees or Kelvin), F_n is the noise figure of the receiver; B_n is the receiver bandwidth and $(S/N)_{req}$ is the required Signal to Noise Ratio (SNR). Some of the parameters in the radar equation (5.1) require further discussion; they are outlined in the following section.

5.1.1 Transmit power (P_t)

It is ideal for a radar system to have a transmit power as large as possible depending on the specific short, medium or long-range application of the radar. However, in practice the transmit power is limited by several factors. The first and most important factor is that the maximum transmitted power for any system is specified and controlled by national and international bodies such as Federal Communications Commission (FCC) [70, 71]. The main motivation for the choice of transmit power is health and safety limits. On the other hand, achieving the allowed maximum power at some frequencies can be expensive and might make the system quite bulky and heavy. It also depends on the technology maturity for providing high powers at certain frequencies.

5.1.2 Integration time (t_{int})

The coherent integration time or in other words, "time on target" is usually considered for pulsed radars. What actually defines the detection performance of a system is not the maximum power but the total energy on target. This is because the coherent signals reflected by target would add up constructively and increase with time. The noise, which is a random process, decorrelates with time. By carrying out signal integration over time, the noise level may increase but not to the same extent as the signal. The SNR of the integrated output is therefore increased; which results in better detection performance for longer coherent integration time. The dynamic range of the non-integrated images presented in Chapter 6 can improve by increasing the coherent integration time. However, this is not exercised in this study.

5.1.3 Minimum detectable signal (S_{min})

Minimum detectable signal (MDS) is the smallest (weakest) signal that the receiver can detect. It is the smallest signal before it is undistinguishable from noise. It is defined as the

receiver's sensitivity. MDS can be calculated using equation (5.2) [16]. The required signal to noise ratio $(S/N)_{req}$ defines the required value that the signal magnitude needs to be, in order to be larger than noise magnitude, so that it is detected [19]. This defines the detection threshold level applied to the signal mixed with noise.

5.1.4 Receiver Noise Floor

Equation (5.2) can be re-written in logarithmic form as equation (5.3). The noise floor of the radar system is defined in equation (5.4):

$$S_{\min} = kT_0B_nF_n + SNR_{required}\,[\text{dB}] \tag{5.3}$$

$$P_N = kT_0B_nF_n\,[\text{dB}] \tag{5.4}$$

where P_N is the noise floor, T_0 is equal to 290 K at room temperature; B_n is the receiver bandwidth, in most receivers it is equal to the *Intermediate Frequency* (IF) amplifier bandwidth [16]. The IF amplifier bandwidth of the radar under discussion is measured to be around 2 MHz. The noise figure, F_n, of the systems is 11 dBm [16, 19]. By using equation (5.4), the noise floor of the radar system under study is calculated as -99.9 dBm. It can be concluded that the radar system discussed in this study has a relatively large noise value.

5.2 Signal to Clutter Ratio (SCR)

The purpose of the imaging radar under study is to detect and locate road features and objects in order to form an image for further classification of objects. The response from the road objects and features within the antenna beam is the desirable signal. Therefore, the high intensity reflection from road features and objects with respect to background backscattering from the relatively uniform road surface is defined as the signal. The background reflections from the relatively uniform road are defined as clutter. Clutter strength is usually much

higher than the noise floor. Therefore, the radar system discussed in this study is clutter limited rather than noise limited. The initial threshold for detection of the obstacles is defined by the mean power of background clutter. The SCR can be defined according to equation (5.5) [16]:

$$\frac{S}{C} = \frac{P_s}{P_c} = \frac{\sigma_{trg}}{\sigma_0 \times A_{res\_cell}} \tag{5.5}$$

where P_s is the signal power and P_C is the clutter power. σ_{trg} is the RCS of the target, σ_0 is the RCS of the surface per unit area and A_{res_cell} is the area of the resolution cell. The required SCR for the images presented in chapter 6 is about 3-4 dB.

Methods such as increasing the integration time (t_{int}) and signal equalization discussed in section 3.3.3.1 can enhance SCR. Signal equalization is implemented in forming some of the images presented in chapter 4 and chapter 6.

5.3 Dynamic range of the 150 GHz images

The dynamic range of a radar receiver is the difference (in dB) between the smallest received signal and the largest signal that can be present in the receiver bandwidth while the smallest signal is received. In other words the receiver's ability to pass large and small signals simultaneously in such a way that signals integrity is maintained [19].

For a radar image, dynamic range is defined as the largest and smallest responses possible to be displayed on one image. The higher end of the dynamic range for the images can be defined as an intensity level where the receiver saturates. The most sensitive component within the radar receiver under discussion is the frontend mixer, which saturates at around 10 dBm. The mixer saturation point defines the upper limit of the dynamic range. The lower limit of the dynamic range of the images in this study is adjusted by applying a threshold

above the mean power of the background clutter to the images. The dynamic range of the normalised intensity images presented in the chapter 6 is set to 40 dB, unless otherwise specified.

Dynamic range of radar images can be enhanced by matched filtering. The matched filter is the optimal linear filter for improving the signal to noise ratio (SNR) in the presence of noise. Two-dimensional matched filters are commonly used in image processing; for instance to improve SNR or achieve superior resolution. Applying a matched filter is equivalent to correlating the received signal with a copy of the transmit waveform [23]. However, a match filter has not been applied to the imaging results presented in this thesis.

5.4 Ground resolution

The ground resolution (ΔG) is the component of the range resolution along the ground. The range resolution is defined by the sweep bandwidth in FMCW radar. The range resolution (ΔR) of the radar with bandwidth of 5 GHz using equation (2.4) is equal to 3 cm.

In order to define the ground resolution (ΔG), the component of the range resolution is projected on the ground. It is found using equation (5.6) where (θ) is the grazing angle defined in Fig.1.3. It is evident that the larger the grazing angle, the larger the resolution cell on the ground in range. For the grazing angles used in this study, which are up to 5°, it results in 3.01 cm ground resolution, indicating negligible difference between the range resolution and ground resolution.

$$\Delta G = \frac{\Delta R}{\cos(\theta)} \tag{5.6}$$

5.5 Frequency Modulated Continuous Waveform (FMCW)

The radar under study uses a pulse compression technique in the form of FMCW modulation in order to obtain the wide bandwidth required for accurate range measurements. Linear frequency modulation is an appropriate solution for automotive applications in contrast to pulsed radars that are expensive and require a high speed Analogue to Digital Converter (ADC).

Therefore, a linear FMCW is used where the frequency linearly increases (up-chirp) or linearly decreases (down-chirp) within a given time interval (see Fig.5.4 and Fig. 5.6) [21].

Fig. 5.4 shows a Linear Frequency Modulated Waveform with transmit and receive chirps. The larger the transmit frequency deviation (Δf) in a given time interval (T_{Sweep}), the more accurate the measurements of the transit time and the wider will be the spectrum. The frequency deviation is called the sweep bandwidth (Δf in Fig.5.4).

Fig.5.4 and Fig. 5.5 demonstrate the concept of *stretch processing* where radar returns are mixed with a replica of the transmitted waveform [27]. Fig. 5.4 shows that the transmitted signal and the local oscillator (LO) of the receiver mixer, sweep linearly over a bandwidth Δf in the sweep time T_{sweep} at the rate of ($\mu = \Delta f / T_{sweep}$).

If there is a target at the distance R, the transmitted chirp will be reflected back to the transceiver by the target and will be received after the time T_t. The round-trip time (T_t) to the target and back can be described in terms of the range by equation (5.7):

$$T_t = \frac{2R}{c} \tag{5.7}$$

where c is the speed of light and R is the range to the target. In FMCW radar, the round-trip time (T_t) or range is measured indirectly. Instead of measuring the time (T_t), the frequency

difference (shift) between the received signal and the transmitted signal (LO) is measured (the vertical distance between the two lines of Fig. 5.4). If the received signal is mixed (heterodyned) with a portion of the signal currently being transmitted (LO), the frequency difference between these two signals will be produced. This frequency difference is called *beat frequency (f_b)* or *ranging frequency*. As the frequency is swept linearly, the slope of the chirp ($\mu = \Delta f / T_{sweep}$) is known (see Fig.5.4). If the target is considered static with respect to the radar transceiver, the beat frequency (f_b) is calculated in terms of round trip time (T_t) according to equation (5.8):

$$f_b = \frac{\Delta f}{T_{sweep}} T_t \tag{5.8}$$

By substituting equation (5.7) in equation (5.8), equation (5.9) is obtained which relates the beat frequency to range [21] .

$$R = \frac{T_{sweep} c}{2\Delta f} f_b \tag{5.9}$$

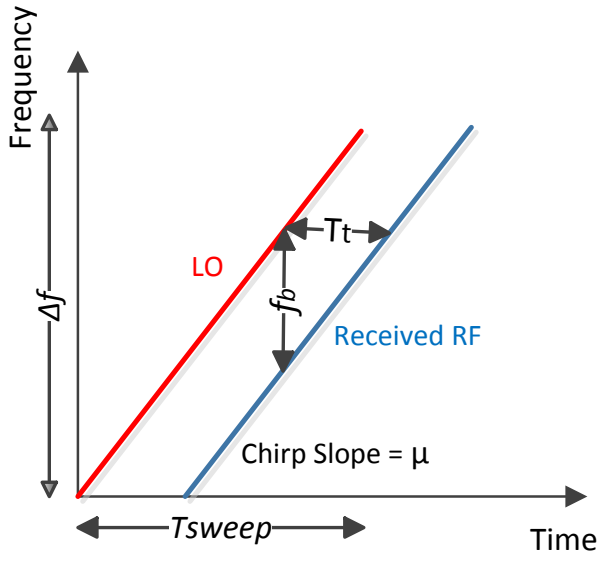

Figure 5.4: Linear Frequency Modulated Waveform, transmit (LO) and receive chirps

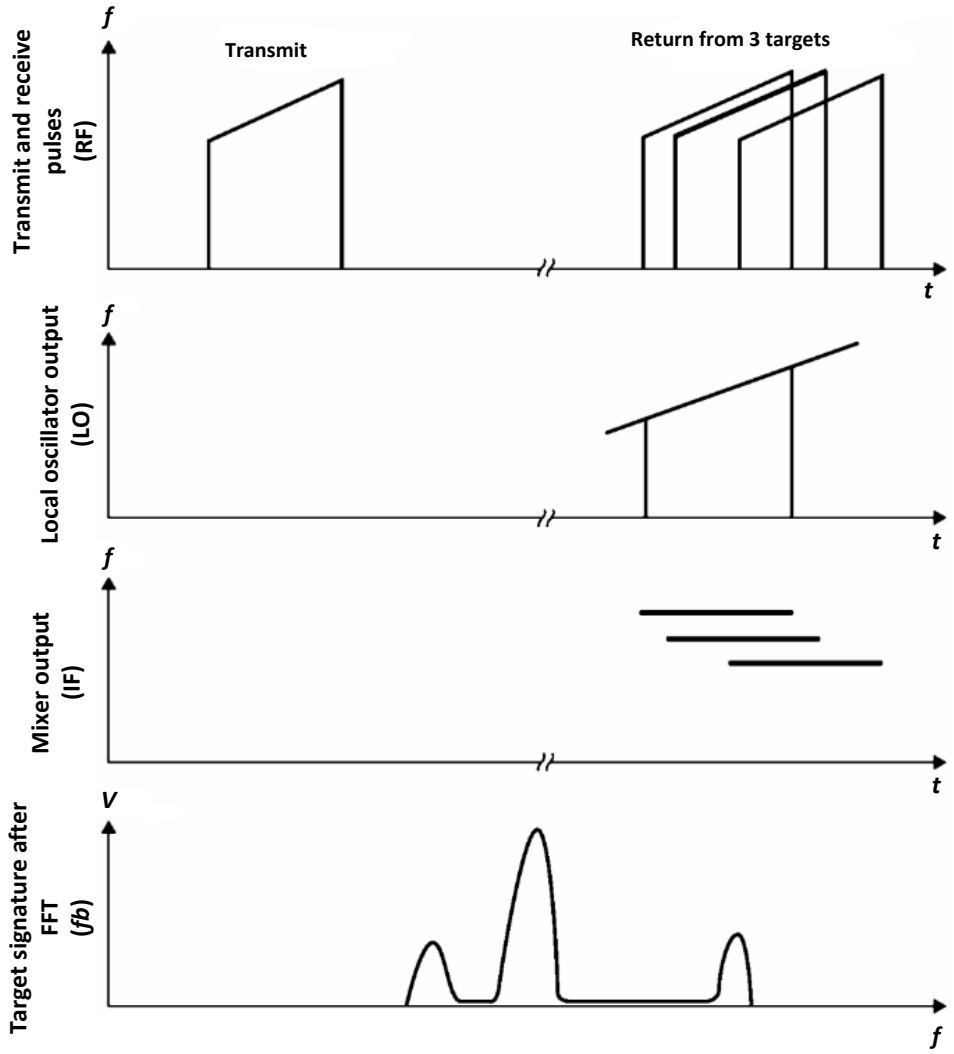

Figure 5.5: Stretch processing of received overlapping chirp echoes [73]

5.6 150 GHz FMCW Radar

In the following section, the principle of the FMCW radar and stretch processing is explained in the context of the radar system under study. Fig. 5.6 shows the transmitted triangular FMCW waveform with up-chirp, continuous wave (CW) and down-chirp. The strobe pulse is used as a trigger for synchronization. On the rise of the trigger, the up-chirp sweep starts at 145 GHz with a linear increase of the frequency over the bandwidth of Δf equal to 5 GHz. The sweep duration (T_{sweep}) is controllable and can be set to values of 1.2 ms, 2.2 ms, 5.2 ms

and 10.2 ms. Fig. 5.7 and Table 5.1 show the four chirp sweep times which are named as four radar modes. The choice of radar mode depends on the application and the available time to detect an arbitrary target (i.e. how fast the target is moving). Even though the longest chirp provides more total energy on target, it cannot not be used for fast moving targets. The experimental results presented in chapter 6 were measured in mode 1 of the radar. The reason for this selection was that the radar mode l has a more linear response of output power versus input beat frequency (range) in comparison to other radar modes within chosen imaging range. This is evident from Fig. 5.11. The beat frequency at the IF stage of the receiver defines the range to the target and accurate range measurement is obtained if the IF amplifier gain is linear for the range of interest. In radar mode 1,the measurement range in this study (from 5 m up to 24 m) lies within the relatively linear portion of the IF amplifier response. After the frequency modulated up-chirp, there is 2 ms of CW transmission in all radar modes. It can be used to measure the Doppler shift for the relative movement of targets to the transceiver. The trigger signal fall, marks the start of the down-chirp sweep, which is the mirror of the up-chirp sweep, with linear decrease of the frequency from 150 GHz to 145 GHz. Both up chirp and down chirp represents a conventional triangular FMCW waveform needed to separate the range information from the Doppler shift [9]. However, Doppler shift is not discussed in this thesis as all the measurements are taken in static scenarios. Following the down chirp, there is a 7.6 ms of idle time with no transmission. The total sweep time varies from 12 ms to 30 ms from mode 1 to mode 4.

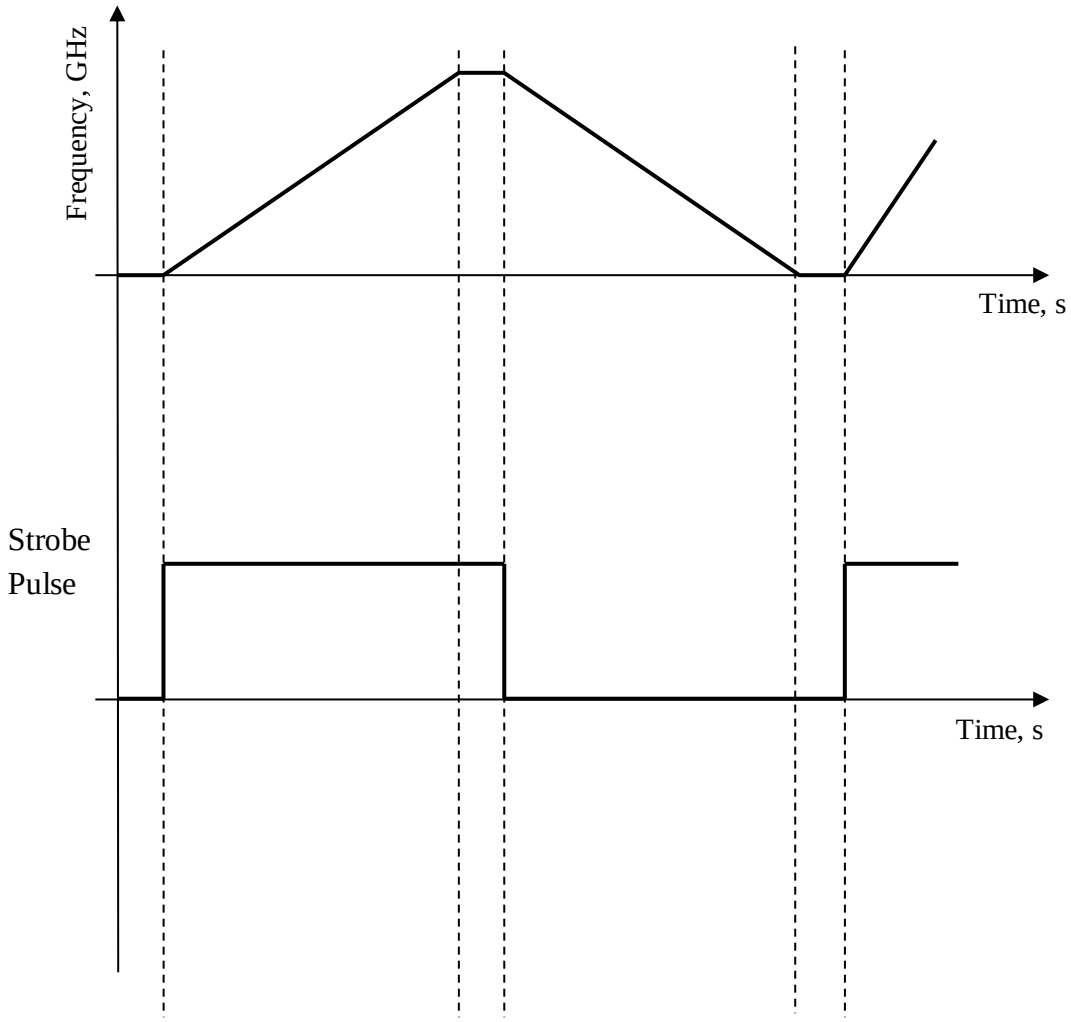

Figure 5.6: FMCW radar up-chirp and down-chirp with the strobe pulse[20].

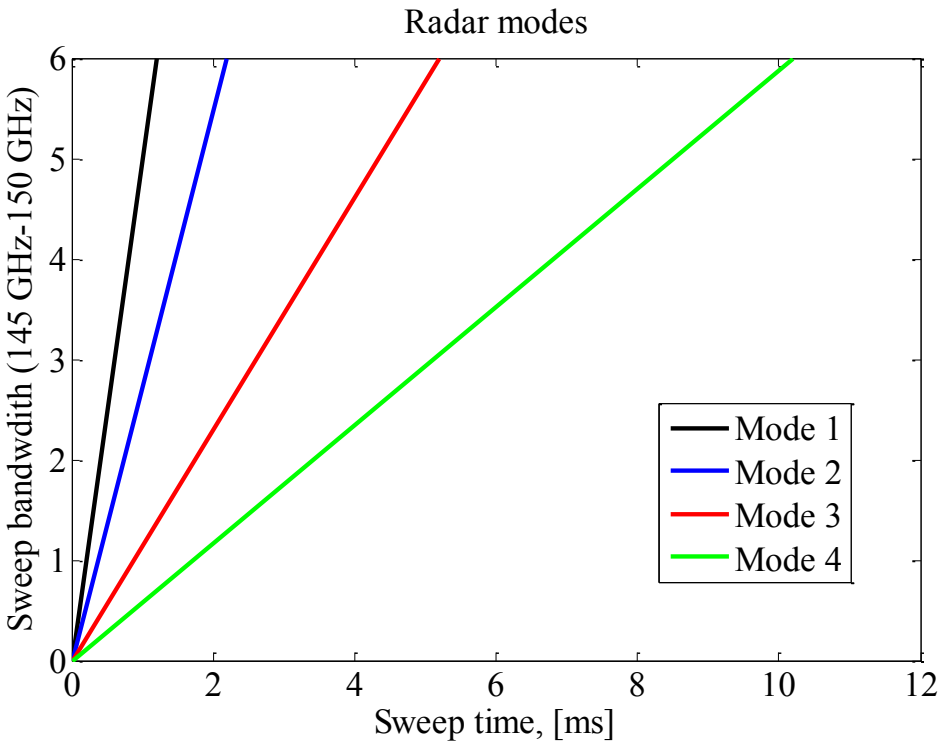

Figure 5.7: The four radar modes depending on the sweep time

Table 5.1: The four radar modes and their sweep times

Radar mode	I [ms]	II [ms]	III [ms]	IV [ms]
Sweep 1	7.6	1.2	2.0	1.2
Sweep 2	7.6	2.2	2.0	2.2
Sweep 3	7.6	5.2	2.0	5.2
Sweep 4	7.6	10.2	2.0	10.2

Fig.5.8 shows the summarised block diagram of the FMCW radar operating at 150 GHz. The Δf =5 GHz bandwidth (145–150 GHz) is obtained by using a (x12) frequency multiplier chain fed by a 7.5 GHz sweep synthesizer. The baseband waveform is amplified by a power amplifier with the nominal gain of 10 dB before up conversion and transmission.

The received 150 GHz + f_b signal is split into two channels. One is denoted *I*, for *in-phase* channel. The other is called *quadrature* or *Q* channel. The principles of two-channel coherent or *I*/*Q* detector can be found in reference [18, 23]. Subsequently, in both channels the

received signal is mixed with the local oscillator (LO) (which has a identical phase to the transmitted signal) to form the sum and difference signals. For a static scenario, let us considered that the f_1=150 GHz is transmitted. The received signal will be *150 GHz* +f_b. At the output of the mixer, the sum (*300 GHz* +f_b) is filtered out by the internal low Pass Filter. The difference will be *150-150 GHz*+ f_b, *which* is equal to f_b. The measured f_b is the Intermediate Frequency (IF) output.

At this point, the analogue beat frequency (f_b) may be extracted as *I* and *Q* data (SMA output). Otherwise the signal is amplified using an IF amplifier (with embedded high pass filter) in order to reject DC and low frequency components. The IF amplifier is discussed in the next section. After the IF stage, the signal is digitised to 4096 data points using an Analog to Digital Converter (ADC). The Fourier transform is done with 2049 points. The output of the Digital Signal Processor (DSP) is a User Datagram Protocol (UDP) packet that is acquired by MATLAB for further processing. The output here is the magnitude $\left(\sqrt{I^2+Q^2}\right)$ using *I* and *Q* data.

The 150 GHz imaging radar under study with the chirp sweep bandwidth of 5 GHz in radar mode 1, produces an IF shift (f_b) of 1 kHz per range resolution cell (3 cm), or around 1 MHz at 30 m range.

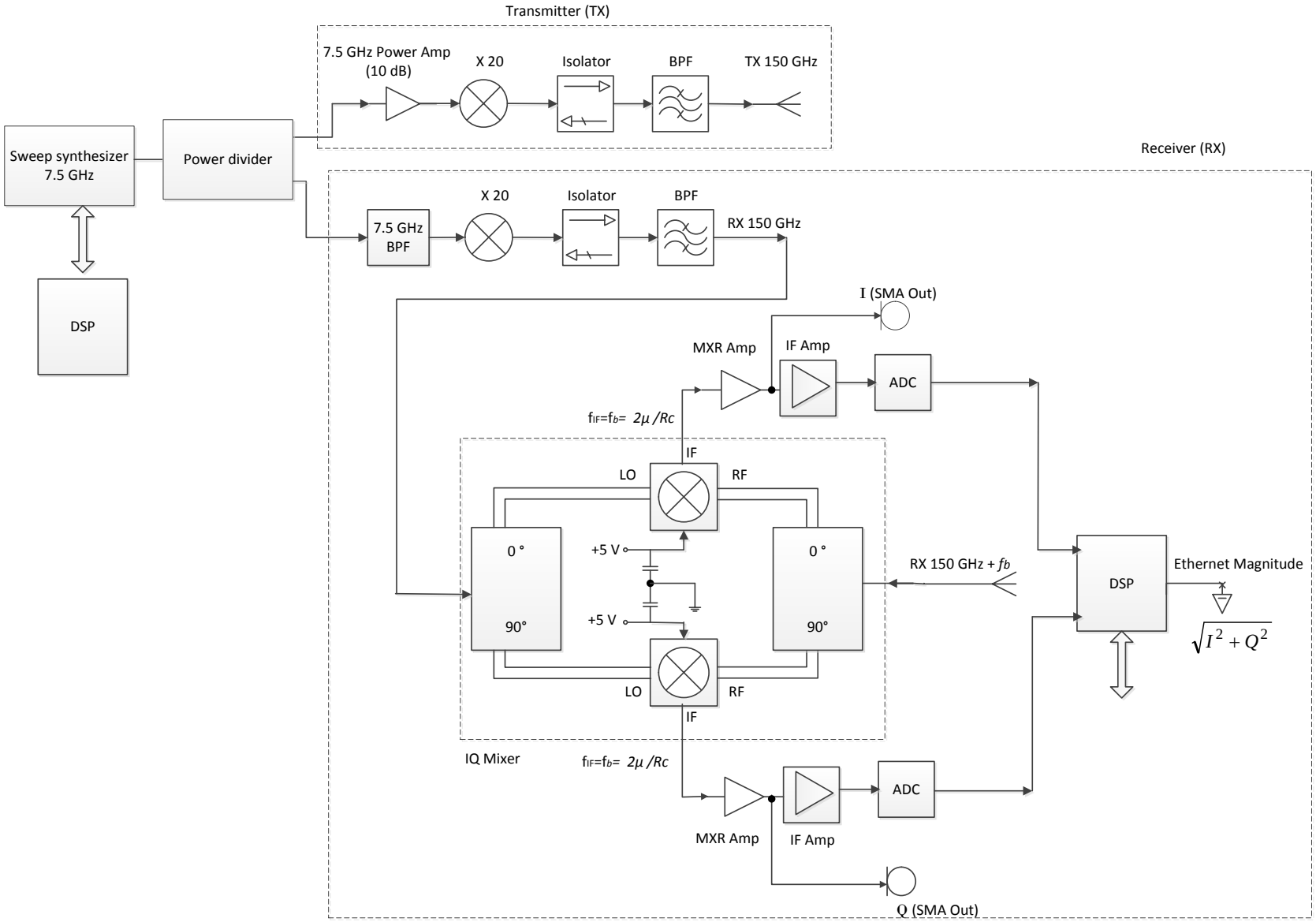

Figure 5.8: Summarised Block diagram of the FMCW radar operating at 150 GHz

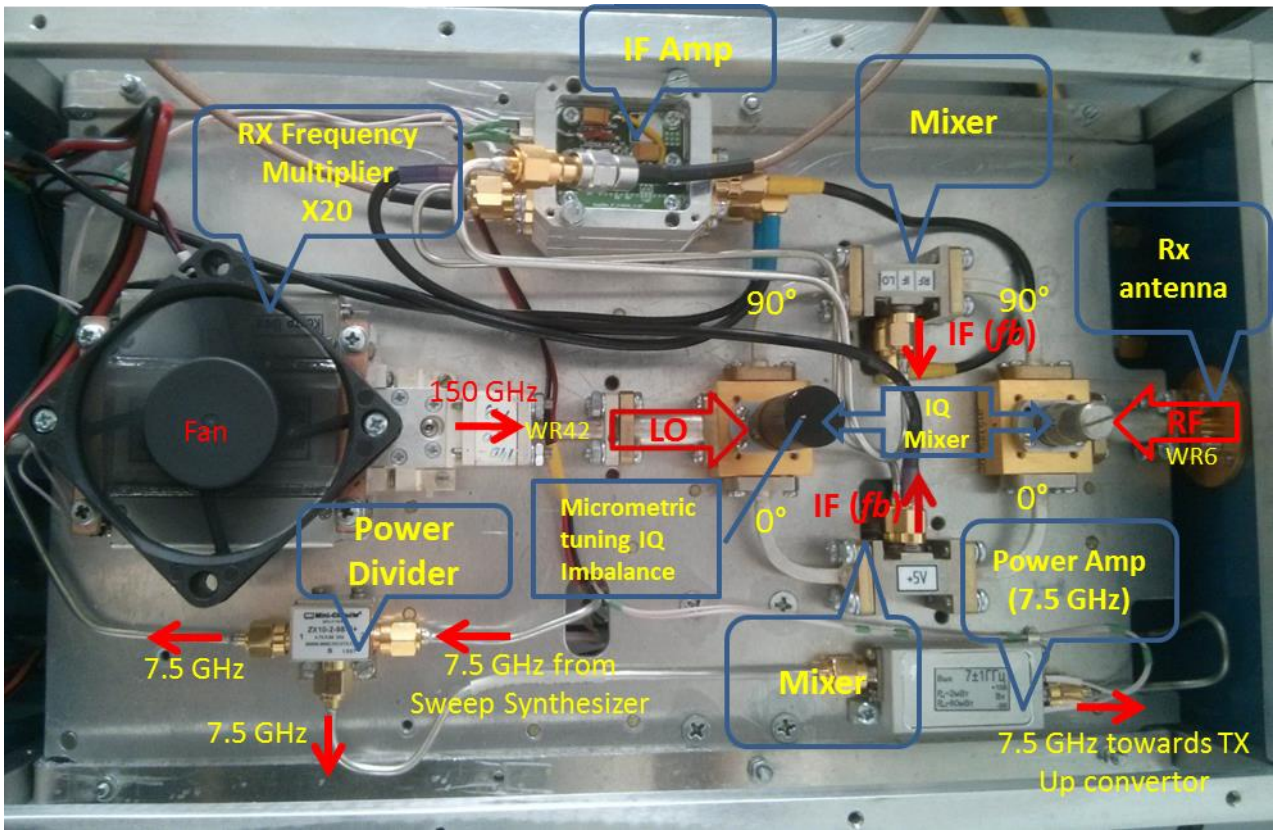

Figure 5.9: Photo of the radar transceiver. This photo mainly shows the receiver side.

Fig. 5.10 shows the 150 GHz radar system mounted on a turntable. Two custom-made lens horn antennas are attached to the radar box. They are used for separate transmit and receive channels. The radar system is a portable prototype of size of 32 cm long, 15 cm wide and height of 20 cm. The weight of the radar system (excluding the turntable) is about 2 kg.

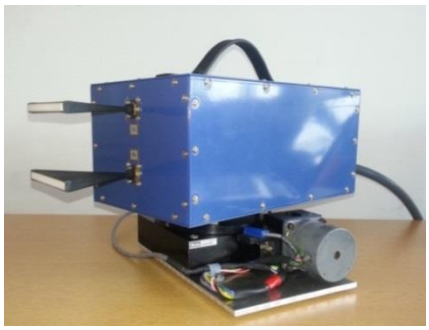

Figure 5.10: 150 GHz FMCW radar with two lens-horn antennas on a turntable to provide azimuth scanning

5.6.1 IF Amplifier

The IF amplifier frequency response of the 150 GHz radar is shown in Fig. 5.11 on a log-log scale. It shows the measured gain of the amplifier versus IF frequency (equal to f_b), ranging from 10 KHz to 2 MHz. The gain rises almost linearly up to about 44 dB where it saturates. However, nonlinear behaviour is observed throughout the graph. The range scales corresponding to beat frequencies calculated by (5.9) for each of four radar modes (Fig. 5.7) are shown along x-axis.

The IF amplifier gain gradually rises throughout one chirp sweep. This type of amplifier is known as Sensitivity Time Control (STC), or swept gain amplifier [19]. Its function is to compensate for the path loss which is directly proportional to R^n (see equation (5.1)) where n is defined according to the environment. Strong signals are usually returns from close-by objects to the receiver, whereas weak signals are usually from far away targets. Therefore, the attenuation of the signal due to path loss should be compensated [74]. In the ideal case of free-space propagation, the receiver gain should be proportional to R^4. The 2 MHz maximum Intermediate frequency is marked in Fig.5.11. In radar mode 1 for example, the maximum is at around 60 m.

It can be seen that the amplifier gain does not increase after around 300 KHz. There is therefore no compensation after approximately 9 m in radar mode 1. This can be observed in the imaging results discussed in Chapter 6. In some cases as reported in [18], the IF amplifier would have a negative compensation gain for nearby targets in order to prevent saturation of the receiver, although in the case of the radar under discussion, this is not the case.

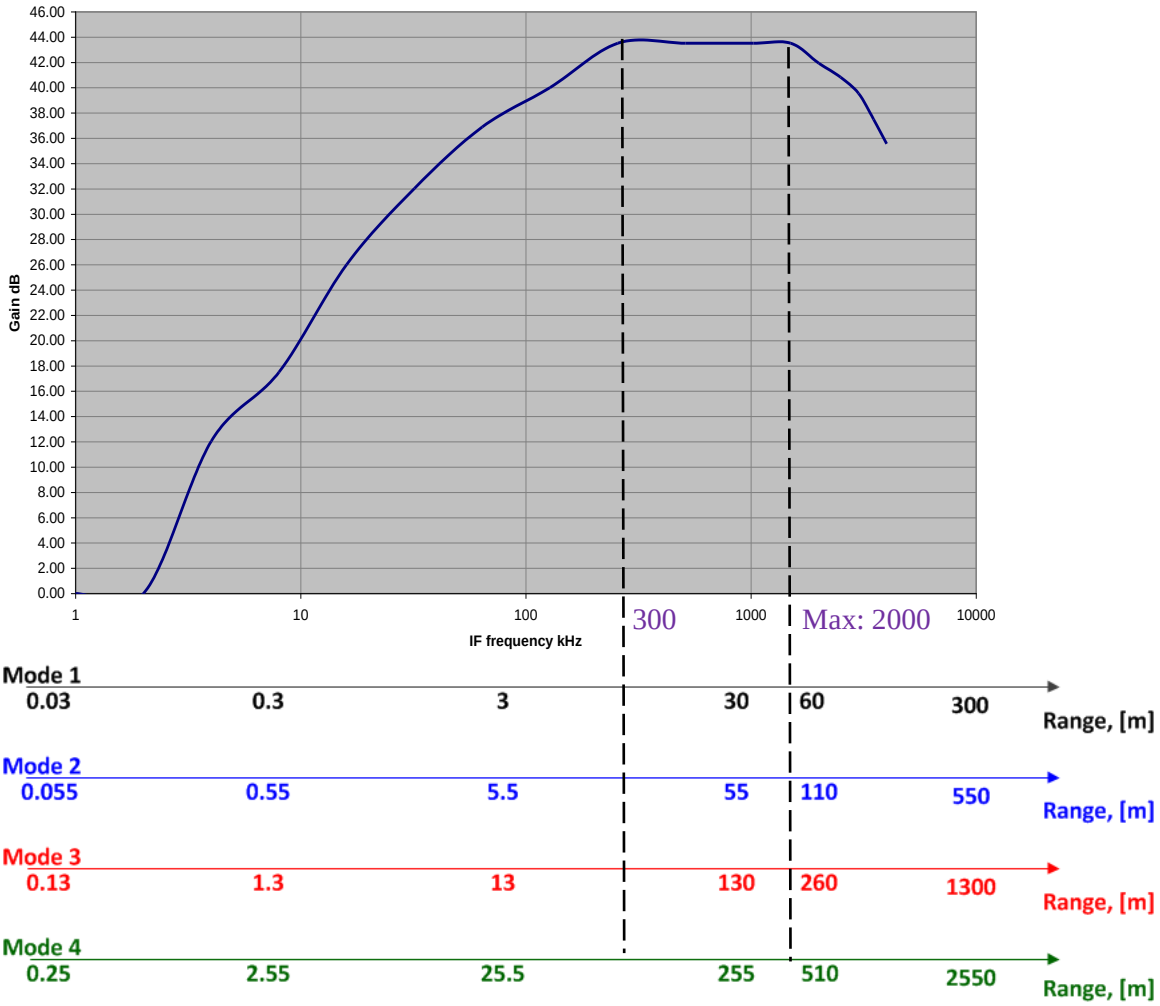

Figure 5.11: IF amplifier frequency response. Gain is plotted as a function of the measured beat frequency (f_b), corresponding to range according to the radar mode.

Alternative to the use of a physical IF amplifier, the path loss can be compensated in the software at the processing stage. The FFT and the gain control can be applied following the extraction of the analogue *I* and *Q* data before the IF amplifier stage.

5.6.2 Maximum unambiguous range

The maximum unambiguous range for the radar is calculated using equation (5.13) [20] where the pulse compression method is used. All the measurements have been carried out in radar mode 1. Therefore, the maximum unambiguous range is calculated for mode 1 when the chirp sweep time, T_{sweep}, is 1.2 ms. The Number of FFT data points is equal to 2048, which in turn results in 2048 frequency bins (see Fig. 3.6).

$$R_u = \frac{c.T_{sweep}}{2 \times N_{FFT}} \tag{5.13}$$

where R_u is the maximum unambiguous range, N_{FFT} is the number of FFT points, c is the speed of light and T_{sweep} is the chirp sweep time. According to equation (5.13), the maximum unambiguous range of this radar is around 73 m.

5.6.3 150 GHz horn antennas

Antenna requirements for automotive sensors are an important factor in sensor design. Packaging space and design (styling) are severe limitations to sensor size and positioning, particularly in the bumper area of the vehicle. Increasing the operational frequencies to 150 GHz and above will offer greater packaging opportunities due to components miniaturization. According to equation (5.14) [69],

$$G = \frac{4\pi\eta A}{\lambda^2} \tag{5.14}$$

for a given antenna gain, G, and efficiency, η, the aperture area of the antenna, A, is directly proportional to the square of the wavelength. Antenna requirements that should be met in designing a scanning high resolution imaging radar system for automotive applications are compact apertures with a narrow beam in the azimuth plane to provide a high angular resolution. In order to provide the wide field of view and to form an image of the scene in front of the vehicle, a steerable (scanning) antennas, multi-beam antenna or antenna array is required. In this study, a mechanically scanning antenna is used. The requirements for the Transmit (Tx) and Receive (Rx) antennas in a monostatic configuration are specified by the expected illuminated footprint in a range between 4 and 100 m from the transceiver (see Fig.1.3). The required cross-range resolution is about 20 cm at 5 m range, which is comparable to the vehicle tyre width. This defines the required beamwidth in the azimuth

plane, Θ_H, shown in. Fig.1.3. According to Fig.1.3, the 3-dB H-plane (azimuth) beamwidth (Θ_H) is calculated using equation (5.15).

$$\Theta_H = 2\arctan\left(\frac{R_c}{2R}\right) \tag{5.15}$$

where, R_c is the azimuth resolution at the range, R. To achieve a resolution of 20 cm at the range of 5 m the 3-dB H-plane beamwidth should be equal to about 2.2 °.

Let us find the required elevation beamwidth of the antenna to cover the specified antenna footprint starting from 4 m (R_{min}) from the transceiver (shown in Fig.1.3). The radar elevation, H, is chosen to be 80 cm above the ground according to the approximate mounting height of the radar in the vehicle's front bumper or grille area. The antenna tilt angle, θ, is about 5°. According to Fig.1.3, the 3-dB elevation beam, Θ_E, is calculated to be about 11°, using equation (5.16):

$$\Theta_E = 2\left[\arctan\left(\frac{H}{R_{\min}}\right) - \theta\right] \tag{5.16}$$

Therefore, Tx and Rx antennas of Θ_E =11° and Θ_H=2.2 ° are required to transmit and receive the 150 GHz FMCW signals of the 5 GHz bandwidth. The horn antenna, one of the simplest types of antenna [69], is chosen to provide the required azimuth and elevation beamwidth. In order to achieve a narrow beam in azimuth plane and wide beam in elevation plane the H-plane sectorial horn with rectangular aperture is designed.

The horn antenna aperture size A along the H-plane, with the 3-dB H-plane beamwidth of Θ_H=2.2 ° and wavelength of λ= 2 mm at 150 GHz is approximated according to equation (5.17) [69]. The aperture size A is equal to 70 mm as shown in Fig. 5.12.

$$A \approx 78^{\circ} \frac{\lambda}{\Theta_H} \tag{5.17}$$

The horn antenna aperture size B along the E-plane, with the 3-dB E-plane beamwidth of Θ_E=10° and wavelength of λ= 2 mm at 150 GHz is approximated using equation (5.18) [69]. The aperture size B is about 10 mm as shown in Fig.5.12.

$$B \approx 54^{\circ} \frac{\lambda}{\Theta_E} \tag{5.18}$$

Fig.5. 12 shows the drawing of the horn antenna with the aperture length of A=70 mm along the H-plane, and the aperture width of B=12 mm along the E-plane. Such an antenna is often called a fan-beam antenna, so this name will be used hereinafter. Equations (5.17) and (5.18) provide approximate values; slightly different approximations are given in [75].

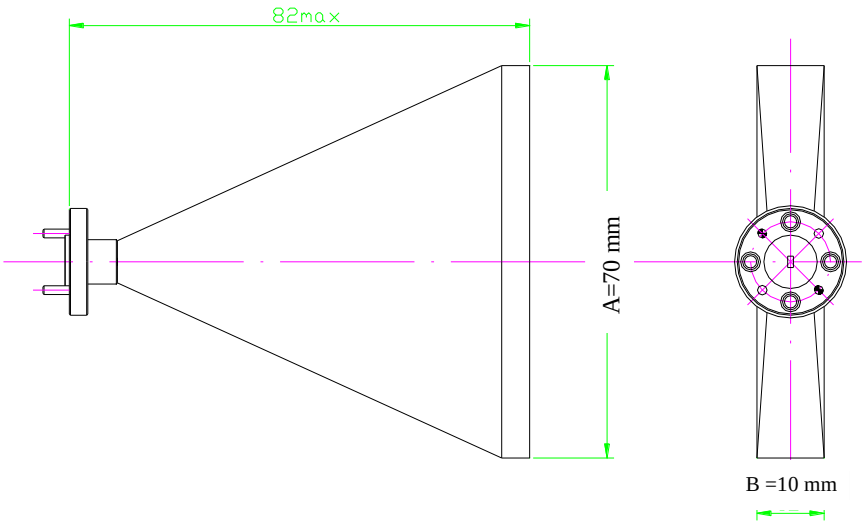

Figure 5.12: Drawing of the lens horn sector antenna, dimensions are in mm.

The designed antenna was fabricated and measured. The measured azimuth beamwidth of the Tx and Rx antennas is shown in Fig.5.13. It is evident that the measured 3-dB azimuth beamwidth agrees with the calculated 2.2 °.

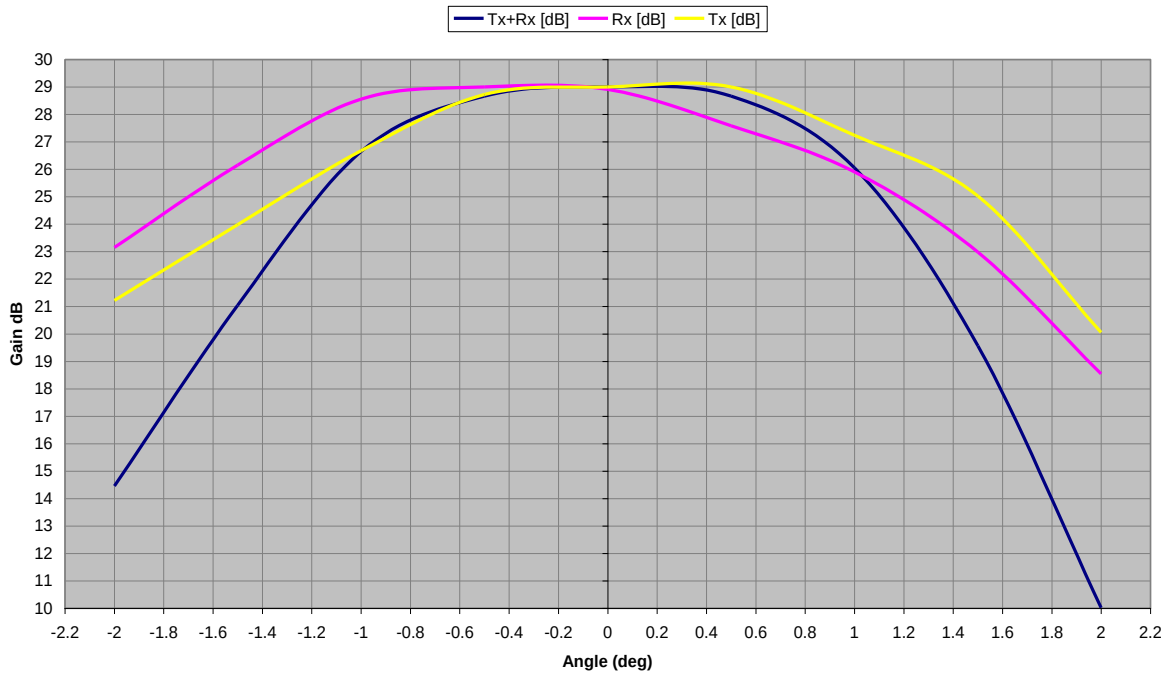

Figure 5.13: Measured antenna pattern in azimuth

The calculated farfield region ($d_{Farfield}$) for the narrow H-plane (azimuth) beam with maximum effective aperture size of 70 mm starts from 4.9 m from the transceiver, according to equation (5.19). According to Balanis [69], the *farfield region* is defined as the region of the field of the antenna where the angular field distribution is essentially independent of the distance from the antenna.

$$d_{Farfield} = \frac{2D_{eff}^{\ 2}}{\lambda} \tag{5.19}$$

where D_{eff} is the effective aperture area of the antenna, and λ is the wavelength. In order to regulate the amplitude and phase distributions of electromagnetic field over the aperture of the horn antenna, it is loaded by a dielectric material (see Fig. 5.14). This results in a tapered amplitude distribution of the aperture field, which can suppress the side-lobe radiations of the antenna that yields near perfect Gaussian beams [69, 76]. The second reason is to bring the farfield distance closer to about 2.5 m from the reference plane of the transceiver.

Antenna gain

Antenna gain is a measure that takes into account the efficiency and directivity of an antenna [77]. Equation (5.20) approximates the gain of the fan beam antenna under discussion, using the 3-dB H-plane and E-plane beamwidths [69]:

$$G_0 \approx \frac{25{,}000}{\Theta_H \Theta_E} \tag{5.20}$$

where, G_0 is the total maximum gain of the antenna, Θ_E is the beamwdith in elevation (degrees) and Θ_H is the beamwdith in H- plane (in degrees).

By substituting the beamwidth values of the antenna in azimuth (2.2 °) and elevation (10°) in equation (5.20), the maximum antenna gain is approximated to 30 dBi, which agrees well with the measured value of 29 dBi shown in Fig.5.13.

Antenna Isolation and polarization

Fig. 5.14 shows the co-located horn transmit and receive antennas attached to the radar body. The isolation of 60 dB is achieved by using separate antennas for transmission and reception. This is usually the simplest way of achieving isolation between transmit and receive channels [21]. The antenna marked as *B*, is connected to the transmitter and *A* is connected to the receiver. Theoretically, both antennas should be identical. However, the measured two-way antenna pattern showed slightly different beams. This arrangement was therefore, chosen experimentally to provide the narrowest two-way beam. The polarization, which is defined at the waveguide- antenna flange excitation, is vertical for experiments carried out in this study.

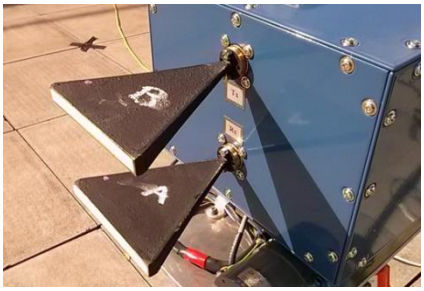

Figure 5.14: Lens horn antennas connected to transmitter and receiver channels

Table 5.2, summarises the parameters of the prototype FMCW radar introduced in this chapter. The table consists of five sections defining parameters of the sub-systems of the radar under development: transmitter, receiver, antenna, processing unit, digital data. Calculated and measured values are both present in this table

Table 5.1Characteristics of the 150 GHz FMCW radar

Parameter	**Values**
Transmitter	
Power output into antenna	15 mW
Frequency sweep	145 - 150 GHz
Sweep bandwidth	5 GHz
Waveform	FMCW
Chirp Sweep Time	1, 2, 5,10 ms
Total sweep time (duty cycle)	30 ms
Antenna	
Antenna type	Lens horn
Gain	29 dBi
Tx/Rx isolation	60 dB
Antenna beamwidth (2 way) azimuth	+/- 1.1°
Antenna beamwidth (2 way) elevation	+/- 5°
Polarization	Vertical
Farfield distance	< 4.9 m
Receiver	
Noise figure	11 dB
IF bandwidth	10 kHz -2 MHz
Processor Unit and Digital Data	
Range resolution	3 cm
Number of range cells per sweep	2048 (2^{11} FFT points)
Operational range	73 m
Digital data output	Via Ethernet after FFT
Data range	16 bits
Interface protocol	UDP
Other parameters	
Analogue data outputs	Strobe, *I* channel, *Q* channel

Power supply	12 V at 2.5 A
Size (Length, Width, Height)	L 320 mm, W 150 mm, H 200 mm

5.6.4 Link Budget analysis

An approximate link budget of the radar under study is calculated using the radar equation. The radar equation (5.1) is simplified and represented in the log scale shown in equation (5.22) [19] so the parameters are in dB units. The path loss factor is considered for the Friis free space model (n=4) [6].

$$P_r = P_t + G_t + G_r + \sigma - 20\log(freq) - 40\log(R) - 30\log(4\pi) + 20\log(c) \quad \text{[dB]} \qquad (5.22)$$

where P_r is the received signal power, P_t is the transmitted signal power, G_t and G_r are the transmit and receive antenna gain respectively; σ is the radar cross section of the target; R is the range to the target and c is the speed of light in vacuum. *freq* is considered at 150 GHz.

The expected received power for a sphere with a radius of 16 cm and RCS (σ) of -10.9 dBm^2 ($\sigma_{sphere}=\pi r^2$) at the distance of 13.5 m from the reference plane of the transceiver, is approximately -73.3 dBm. The system losses *(L)*, transmission losses (attenuation), and multipath effects are not taken into account here.

5.6.5 Path-Loss power compensation

In order to estimate the path-loss in the scenarios of the experiments that are undertaken using the 150 GHz radar, a practical large-scale propagation model of statistical *Log-distance path loss* [22] is used, which can be described by the equation (5.23). In the *log-distance model*, the mean path loss is a straight line with a slope equal to 10*n* dB. It predicts that the received power decays as a function of Tx and Rx distance (2-way distance) raised to the power *n*.

$$\overline{PL}(dB) = \overline{PL}(d_0) + 10n\log\left(\frac{d}{d_0}\right) \tag{5.23}$$

where $\overline{PL}$ is the path loss, d_0 is the close-in distance as a known received power reference point and d is the distance between Tx and Rx. The value of n in equation (5.23) depends on the specific propagation environment. For instance, in the free space model, when signal propagates from the transmitter to the receiver over the distance d, n is equal to 2. The simple form of radar equation (equation (5.1)) is based on the Friis free space equation [22]. The Friis equation, which is only valid in the far-field distance, shows that the received power falls off at the rate of the square of the distance between Tx and Rx (20 dB/decade). However, for accurate results, the power law function should be found for the specific scenario of the experimentation [16]. In general cases where assumptions of deterministic models are not any more satisfied, the statistical models must be used and the value of n should be determined empirically through representative number of measurements. In order to find the n of the power attenuation with the monostatic radar, the canonical target was placed at different distances (d) to the radar.

A stainless steels sphere of diameter equal to 0.283 m and RCS equal to -12 dBsm is used as a canonical target for the purpose of this experiment. Fig. 5.15 and Fig. 5.16 both show the experimental setup. The suspension system was constructed to allow suction cups to suspend a sphere so that the illuminated surface of the sphere is multiple range cells closer than any clutter in the setup. The fiber glass pole used to suspend the sphere at about 1.538 m above the ground. The centre point between the Rx and Tx is about 1.4m from the ground. The floor between the radar and target was covered with Persian carpet as well as the wall behind the target to minimize the clutter. A laser spirit level was used to align the boresight with the nearest point on the sphere. The elevation and azimuth angles were varied by using the stand

that the radar was mounted upon. All measurements were made with the radar to target distance in the range of 3 m to 8 m.

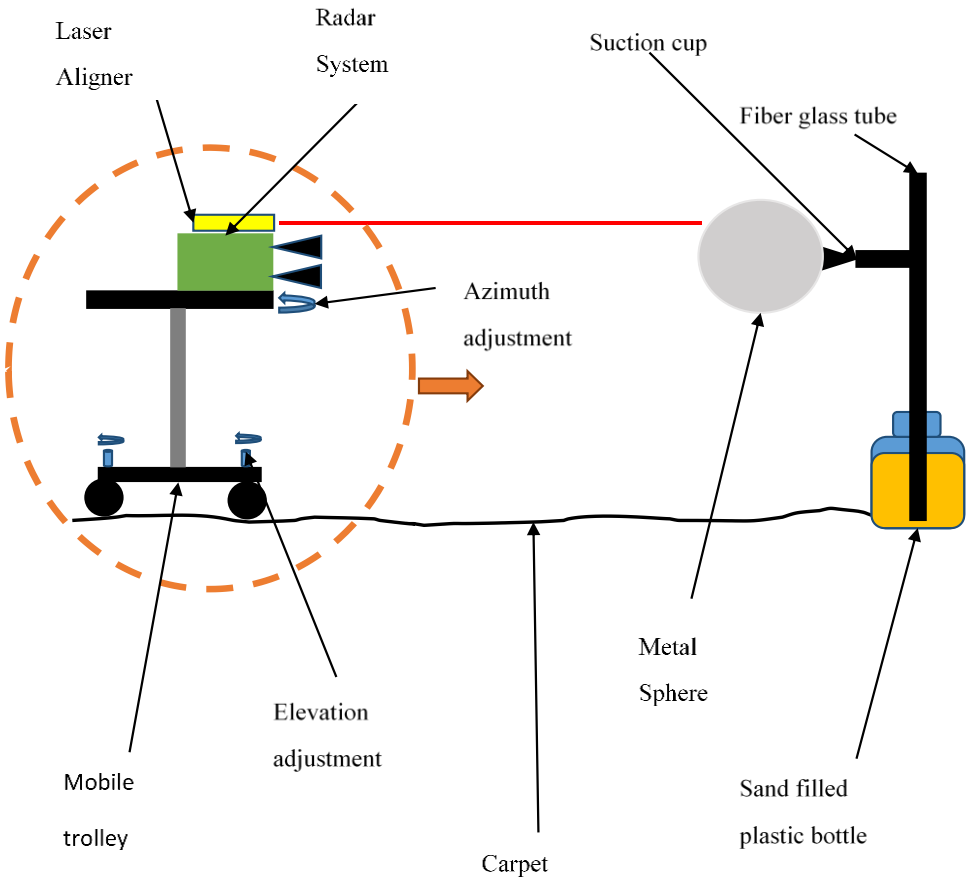

Figure 5.15: Diagram of the experimental setup

Figure 5.16: Realised relatively non-reflective stand with metal sphere attached

Fig. 5.17 shows the magnitude of the received power from the sphere positioned at different distances to the transceiver as a function of the range. By plotting the received power versus distance in log-log scale, and fitting a linear approximation curve to the recorded data points, the decay rate and the power law function is found to be equal to (n=3.3). The value of n can be factored in for the path loss compensation in the measurements taken by the radar system.

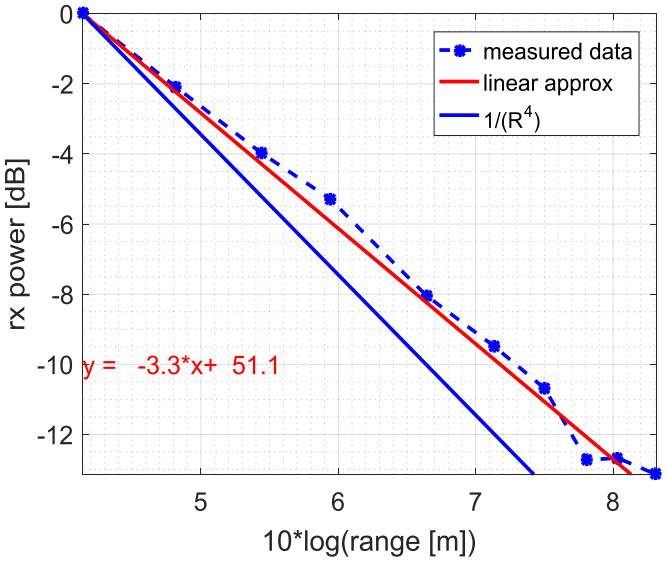

Figure 5.17: Normalised received power from a sphere at different distances to the transceiver; using the measured data (I and Q) in comparison to the theoretically calculated values

5.6.6 Measurement of the radar system response

In order to equalize the target responses measured by radar system under study and to remove the radar system responses from the range profile measurements, the radar system response should be measured. This can be achieved by measuring the reflections from a perfect absorber. The sky is a perfect absorber. In the case of the monostatic configuration, the antennas are pointed to the sky but not directly towards the sun. As the sky acts as a perfect absorber or fully matched medium, there will be no reflections, and the only measured response by the radar system is the one produced by the radar system itself. Fig. 5.18 shows the measurement set-up. Fig 5.19 shows the measured range profile of the radar system

response with the maximum at around 63 dB. By subtracting the recorded system response from received signals, the effect of the system is removed (see chapter 3.3.3.1). Such equalization has been done in some of the experiments presented in chapter 6, where the background signal was considered to be stationary.

Figure 5.18: Measurement of radar system responses by pointing the Tx and Rx to the sky (perfect absorber).

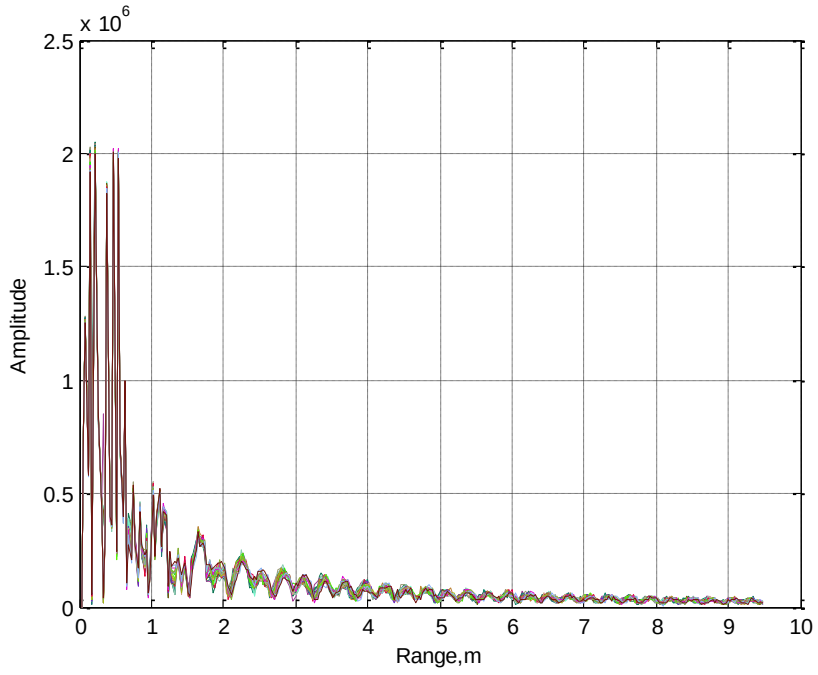

Figure 5.19: Range profile of the 150 GHz radar system response; antennas pointing to the perfect absorber (sky)

5.7 Summary

In this chapter, an overview of principles and design considerations for a radar system is given. Principles of FMCW radar system are discussed in the context of the 150 GHz radar under study. The parameters of the designed 150 GHz radar are summarised in Table 5.1.

The design of a prototype radar system can be investigated in a lot more detail than discussed in this chapter. Detailed discussion of the radar design is beyond the scope of this thesis. Full practical design details of few different types of FMCW radar can be found in [20]. In the next chapter, the imaging results of the 150 GHz FMCW radar are presented.

6. Imaging results of the 150 GHz radar: Objects and surface characteristics

Overview- *This chapter demonstrates the imaging performance of the low-THz FMCW radar discussed in chapter 5 for outdoor unstructured scenarios as expected in automotive environments. The focus is on the initial interpretation of radar images by analysis of features of imaged environments and comparison with microwave radar images. Images of the specific on-road and off-road scenarios have been made at 150 GHz. They are compared to the radar images made by the stepped frequency radar operating at microwave frequencies (30 GHz) introduced in chapter 3 [4]. The images in this chapter are presented without any image processing. The received power is normalised to 0 dB for the sake of comparison.*

6.1 150 GHz FMCW radar set-up

As introduced in chapter 5, the 150 GHz FMCW radar has been custom-made in collaboration with ELVA-1, St.-Petersburg, Russia [14] using the specifications of the University of Birmingham. The requirements for the Tx and Rx antennas in a monostatic configuration were defined by the expected illuminated footprint of a 4 m -100 m extent of the road in range from the transceiver. The minimum required angular resolution is 20 cm at 10 m range and is comparable to the vehicle tyre width. This defines the beamwidth in the azimuth plane, Θ_H, the aperture size and the gain. As a result, two co-located custom-designed H-plane horn-lens antennas of Θ_E =11 ° and Θ_H=2.2 ° were designed to transmit and receive the 150 GHz FMCW signals of the 5 GHz sweep. The 150 GHz radar was mounted on a turntable to provide the mechanical scanning in azimuth (see Fig.6.1(a)). A laptop is used for logging data via an Ethernet connection.

6.2 30 GHz Stepped frequency radar set-up

As introduced in chapter 4, the reference 30 GHz stepped-frequency radar is driven by a Vector Network Analyser (VNA) and uses a single sector parabolic antenna of a 15 cm dish which provides the relatively narrow azimuth beam of Θ_H =3.5 ° (Fig.6.1 (b)). In order to achieve the desired range footprint of up to few hundred metres, the elevation beam was increased to around 12°. This was done by reducing the effective size of the aperture in the E-plane from 15 cm to 4 cm by tapering it with absorbers. This antenna is used for transmit and receive channels, which are isolated by a 2.5 GHz bandwidth circulator so that the configuration is monostatic. The VNA sweeps the frequency from 29 GHz to 31.5 GHz and delivers an overall bandwidth of 2.5 GHz.

In all the experimental results presented in this chapter, the antenna elevation H is around 80 cm (see Fig. 1.3). The height is measured to the midpoint of Tx and Rx antennas for the 150 GHz radar, and to the midpoint of the dish in 30 GHz antenna. The grazing angle or antenna tilt angle, θ, is around 5° (see Fig. 1.3). The parameters of both the 30 GHz and 150 GHz radars are summarised in Table 6.1.

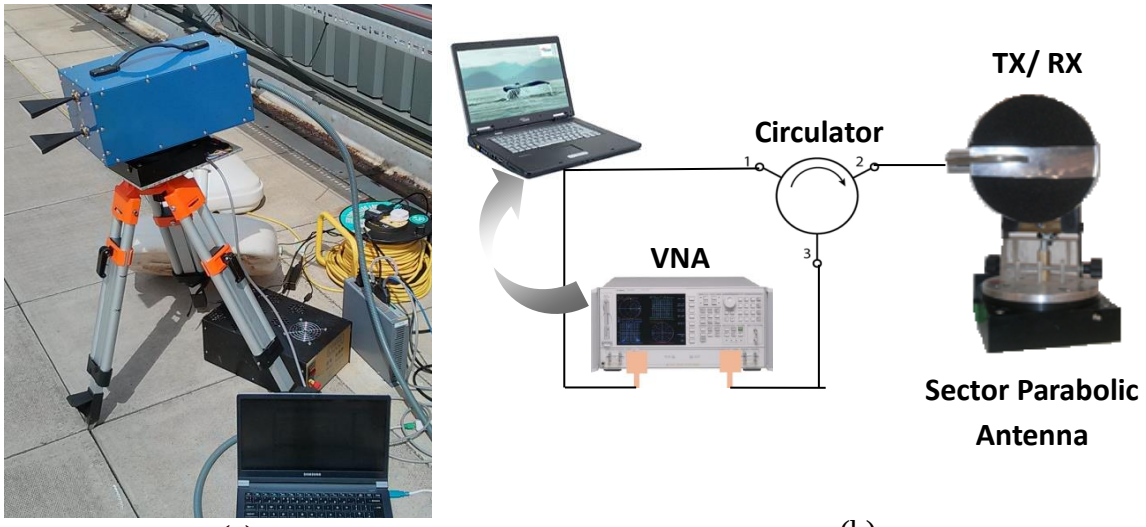

(a) (b)

Figure 6.1: (a) Mechanically scanning 150 GHz FMCW radar set up. (b) The 30 GHz experimental system

Table 6.1: Comparison of 150 GHz and 30 GHz radar parameters

Parameters	150 GHz	30 GHz
Sweep Bandwidth	5 GHz	2.5 GHz
H-Plane Beamwidth	2.2 °	3.5°
E-Plane Beamwidth	11°	12°
Antenna aperture size	Horn-lens 7 x 1 cm^2	Parabolic Sector 15 x 4 cm^2
Antenna gain	29 dBi	20 dBi
Range resolution	3 cm	6 cm
Angular resolution	38 cm (at 10 m)	61 cm (at 10 m)
P_t	15 mW	1 mW

6.3 Measurements in controlled environment

Performance of the imaging radar has been analysed by initial testing in controlled outdoor conditions with calibrated targets (Table 6.2). Corner reflectors of two sizes, a standard rubber speed bump, a rectangular pothole replica (tile taken out of the floor) and a rectangular 'bump' (tile placed above the floor) were all positioned above the tiled concrete floor on the rooftop of the building of EESE School of University of Birmingham (see Fig.6.2). The scene is scanned from -12° to +12° clockwise with 1° steps. Two images of the scene of Fig. 6.2, produced by the 150 GHz radar and 30 GHz radar, are shown in Fig. 6.3 (a) and Fig. 6.3 (b) respectively. The images presented in Fig. 6.3 show the normalised (to 0 dB) received power for the objects of interest in Fig. 6.2. No significant processing has been applied to the images, though a median filter and a threshold were applied to both images.

Table 6.2 : Description of objects used in the scenario of Fig. 6.2

Target	*Dimension*	*Range m*	*RCS dBm^2 @ 30 GHz*	*RCS dBm^2 @ 150 GHz*
Tridehral corner reflector	7 cm (side)	7.8	0.6	14
Tridehral corner reflector	14 cm (side)	12	12	26
Rubber hump	2.7m (length) x 7.5cm (depth)	9.5	N/A	N/A
Square concrete tile	60 cm (side) x 4.5 cm (depth)	5.4	< 20	< 30

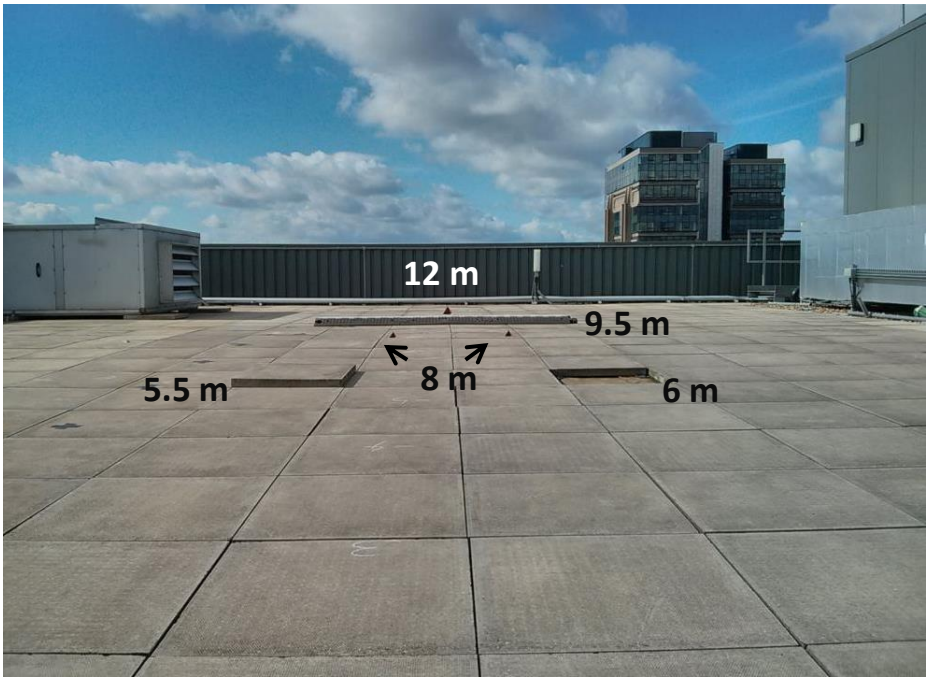

:
Figure 6.2: Controlled scenario with calibrated targets. Roof top of Gisbert Kapp building, University of Birmingham.

It is apparent from Fig. 6.3 that the 150 GHz image (see Fig.6.3 (a)) has a finer resolution in range and azimuth than the 30 GHz image (see Fig.6.3 (b)). The corner reflector at 12 m is visible in the 150 GHz image, while it is not visible in the 30 GHz image. The two corner reflectors at 8 m are 50 cm apart in cross range (azimuth) distance. Therefore they are resolved in the 150 GHz image; however, they are hardly resolved in the 30 GHz image owing to the smaller azimuth resolution of 150 GHz compared to 30 GHz reference radar (see Table 6.1).

Note: In all the images presented in this chapter, each resolution cell in azimuth corresponds to the step size of 1°, while the azimuth beamwidth is 2.2°. Therefore, there is an overlap for each resolution cell in azimuth.

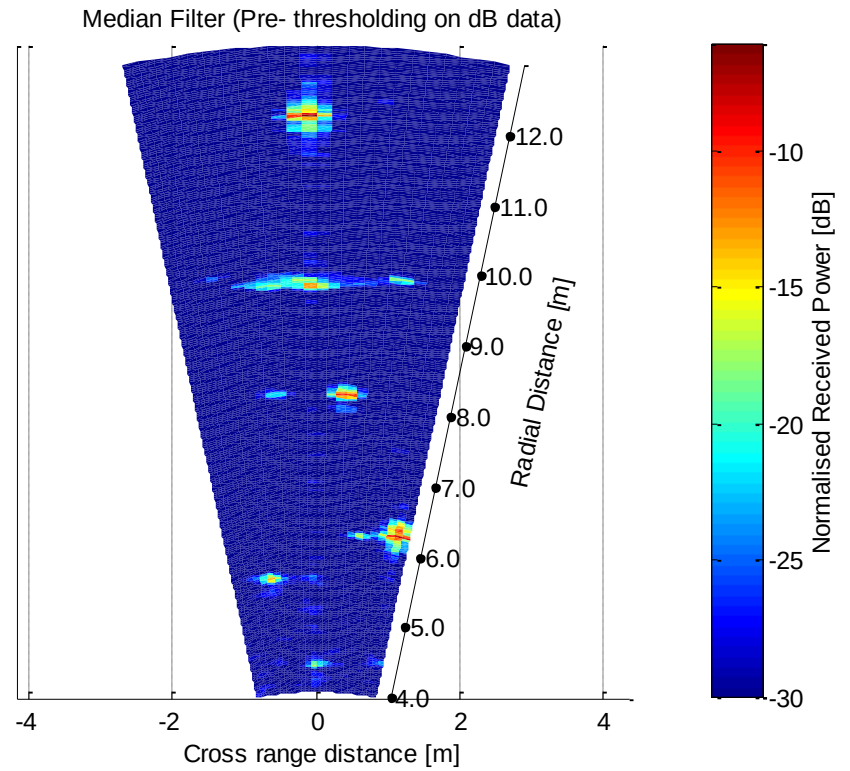

(a)

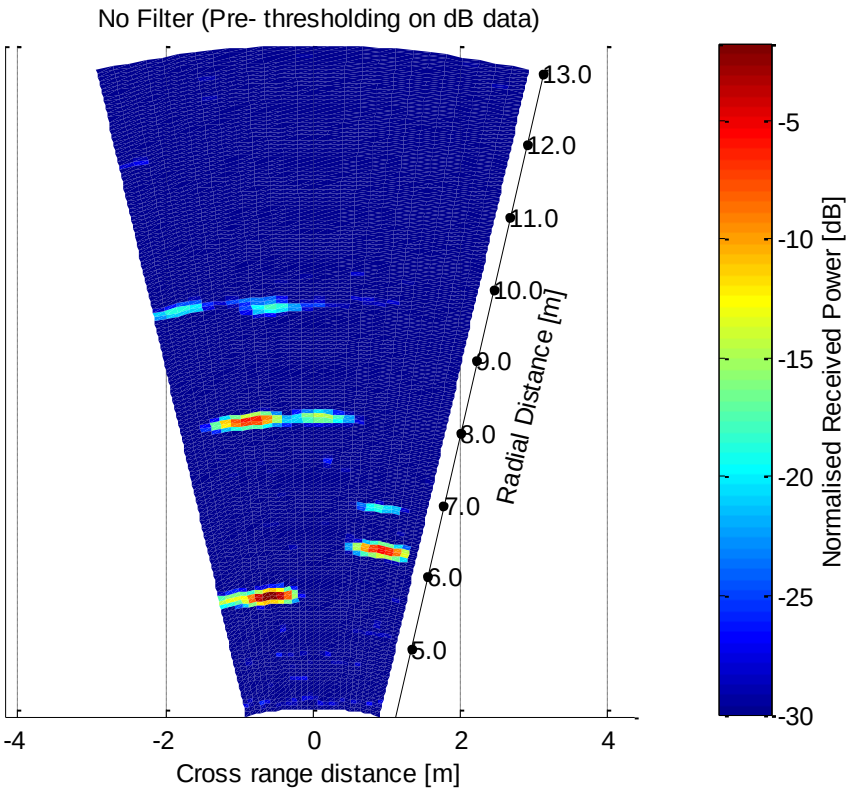

(b)

Figure 6.3: Images of the scene of Fig.6.2 by (a) 150 GHz FMCW radar; (b) 30 GHz stepped frequency radar

Fig. 6.4 shows another experimental scenario in a controlled environment on the roof top of EESE building. The target consists of pieces of car carpet laid on the tiled floor at 6 m from the radar. The purpose of this preliminary experiment was to investigate the texture and material sensitivity of the 150 GHz frequencies. The scene is scanned from -10° to +10° clockwise with 1° steps. Fig. 6.5 shows the imaging result of the scene of Fig. 6.4. The carpet is distinguishable as an area of high intensity on the image at around 6 m. The shape of the carpeted area is recognisable while the bent edge of the carpet is marked as the highest intensity point on the image. The few small horizontal lines at distances of up to 6 m are identified as the exposed edge of the gaps between the tiles.

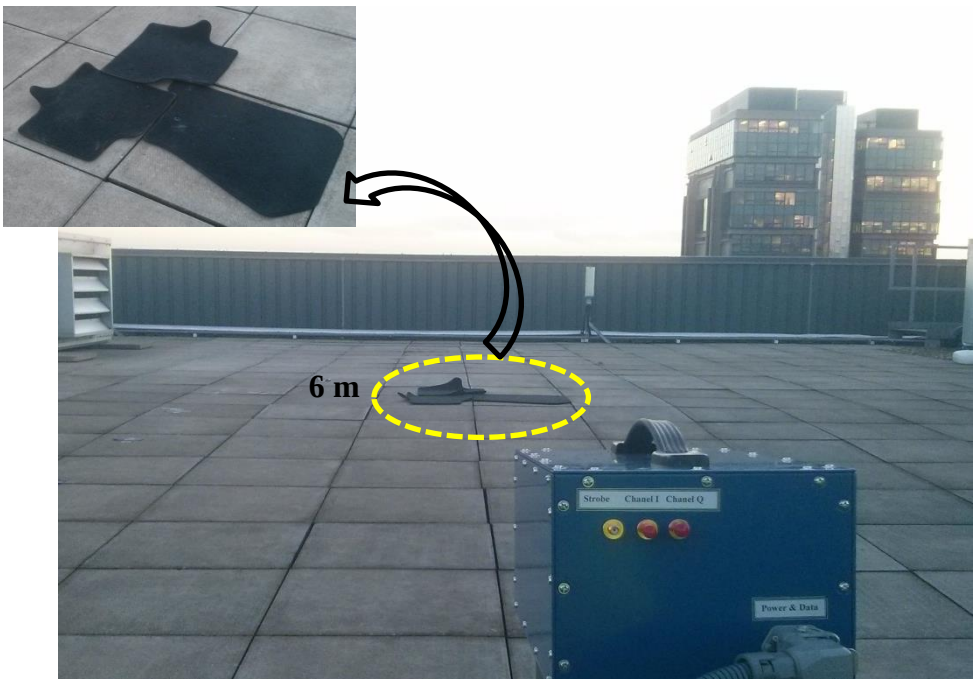

Figure 6.4: Controlled scenario with car carpet at 6 m from the radar. Roof top of EESE building, University of Birmingham.

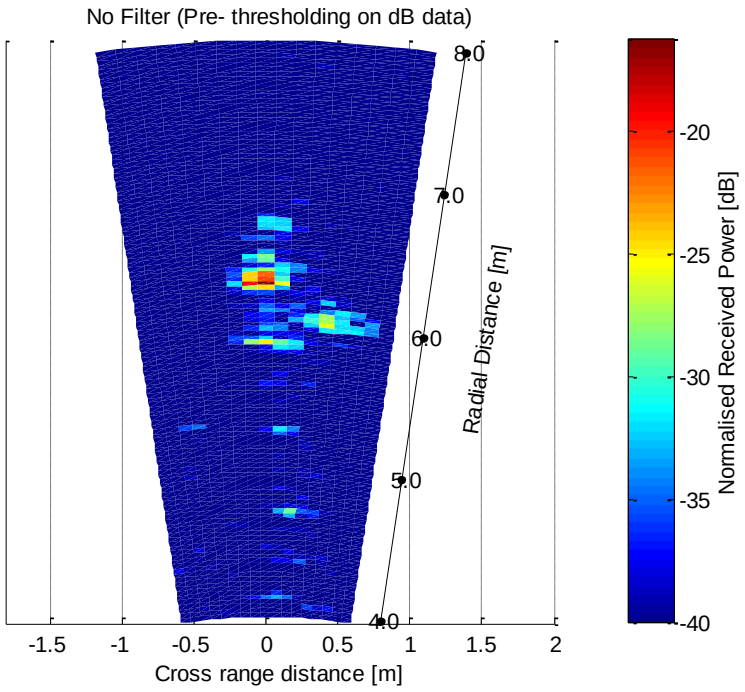

Figure 6.5: Image of the scene of Fig.6.4 using the 150 GHz FMCW radar

6.4 Outdoor uncontrolled environments

In this chapter from this section onwards, the static images of real on-road and off-road scenarios with the focus on features of scattering from surfaces and road objects are presented. Fig. 6.6 shows a road scene on the campus of the University of Birmingham which includes potential obstacles for vehicles at different ranges: a kerb, a wall, a lamp post, small rocks and stones. As a reference, two canonical objects with known RCS (a sphere and a brick) are placed at 6 m and 13 m from the antennas (see Table 6.2). The road is scanned from -30° to +30° clockwise with 1° steps. The two radar images made by the 150 GHz and the 30 GHz radars are shown in Fig. 6.7 (a) and (b), respectively.

Fig. 6.7 shows that the range, the angular position and the intensity of the return from each imaged object correspond to the scene. It is also evident that 150 GHz signal is very sensitive to surface roughness due to its 2 mm wavelength. Returns from the kerb and the wall are seen

as nearly continuous features on the image approaching optical quality, whereas, in the 30 GHz radar image they are seen rather as a set of discrete speckles typical of radar imagery. Strictly speaking, the two radar images cannot be directly compared to one another due to slight differences in range and angular resolution; however, a comparison is still valid as long as emphasis is placed on the differences relating to the increase of diffuse scattering from surfaces of different roughness and texture.

It is worth noting that the increased diffuse scattering of a 150 GHz signal (Fig. 6.7(a)) allows smoother patches to be distinguished from the (generally) rough surface of the road. In the 150 GHz image, the footpath, highlighted in yellow in Fig.6.6, can be clearly recognised by the reduced backscattering. This is a result of the smoother texture of the road compared to the remaining part of it which was covered by loose leaves and soil.

This indicates the great potential of low-THz to deliver information on the texture and profile of road surfaces. It is a borderline frequency range between microwave and optical regions, thus it demonstrates increased diffused reflections from the surfaces which can be seen as flat and mirror-like by microwave and conventional mm-wave radars. High sensitivity to texture and roughness cause further differentiation between patches of slightly different texture that are not generally visible in optical images [78].

Table 6.3: Objects used in the road scenario shown in Fig.6.6

Object	**Dimension, cm**	**Range, m**	**RCS, dBm^2**	
			30 GHz	150 GHz
Sphere	radius=16	13	-11	-11
Brick	22 x10 x 6	6	19	32
Lamp post	r = 7.4 cm, 3 m illuminated area	11.4	29	36
Stone	≈ 43 x 37 x 10	8	NA	NA

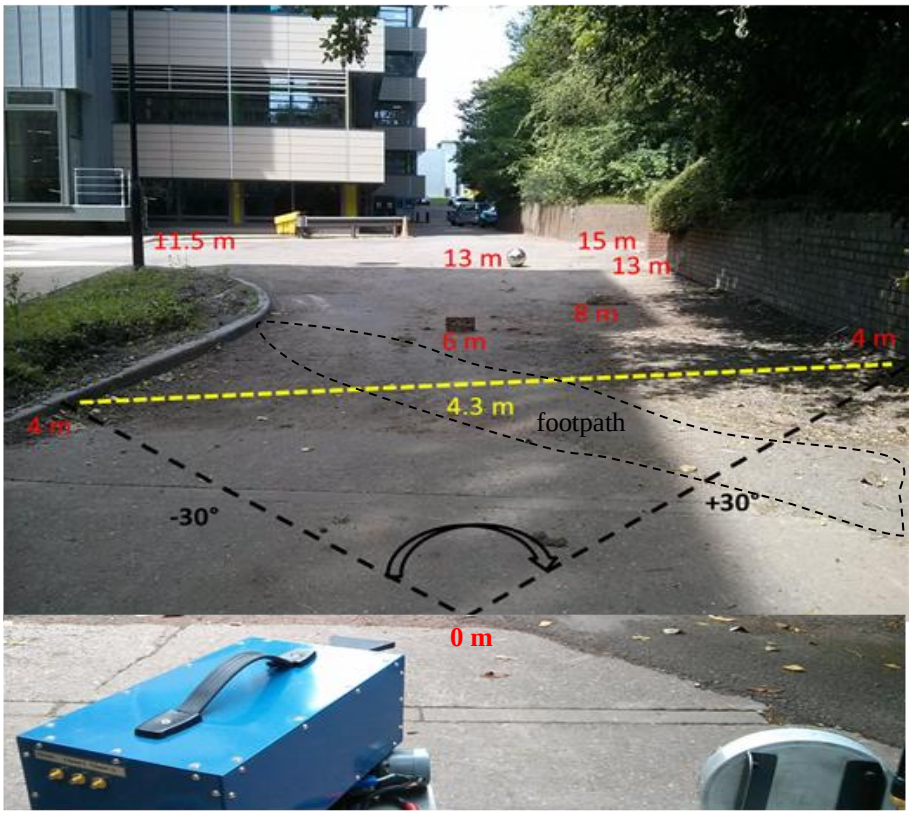

Figure 6.6: Road scenario with different obstacles and road features [78]

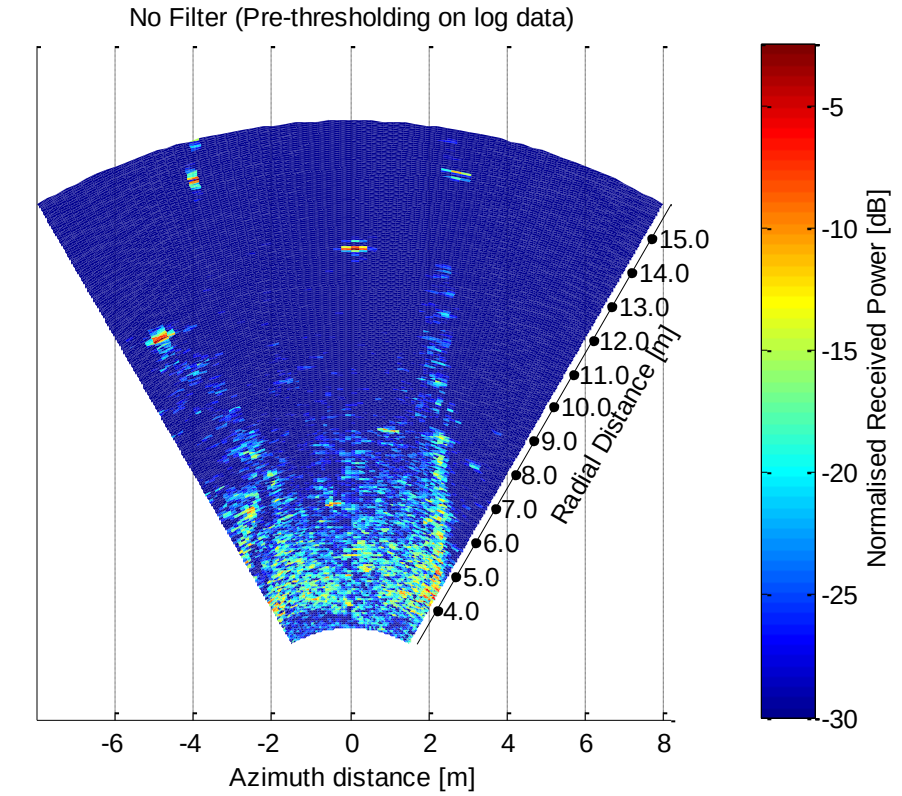

(a)

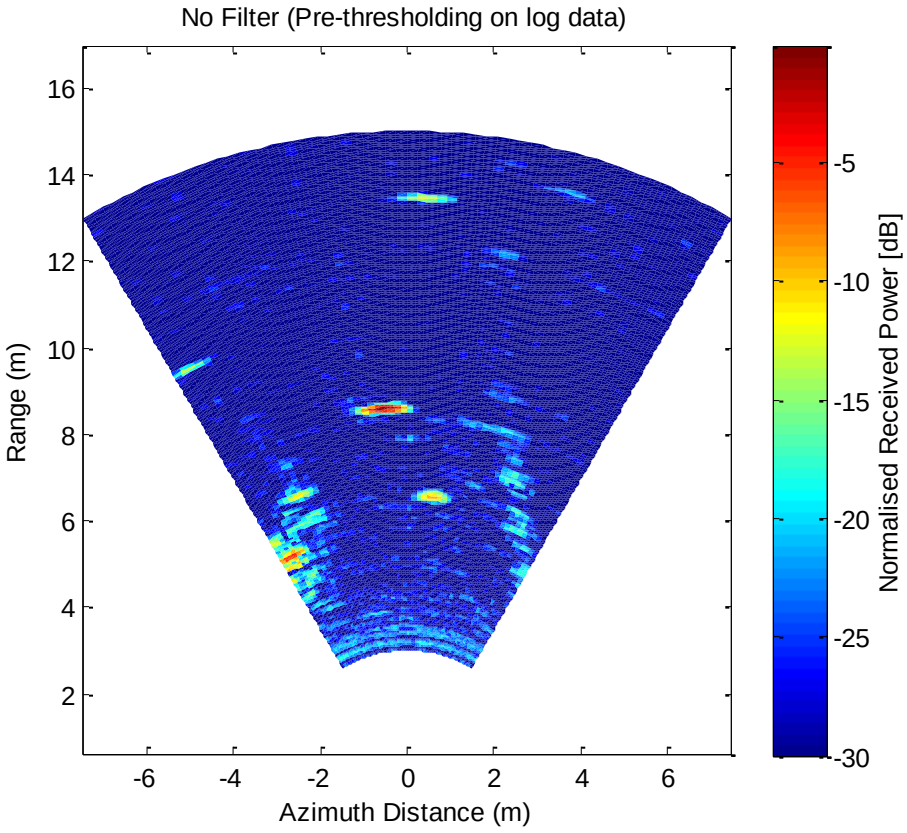

(b)

Figure 6.7: Image of the scene of Fig.6.6 by (a) 150 GHz FMCW radar; (b) 30 GHz stepped frequency radar [78]

6.5 Imaging of road markings at 150 GHz

Fig.6.8 shows photos of the road with rumble-type painted markings on the campus of the University of Birmingham: in (a) the radar is positioned at the side of the road and the scanning beam is directed at an angle to the strips; in (b) the radar is on the road and the axis of the radar scanning beam is perpendicular to the rumble strips. In both cases, the scanning angle is 10° on each side. The rumble strips are 42 cm apart, the width of the strip is 10 cm and the thickness of the paint is approximately 5-7 mm.

In Fig.6.9, the 150 GHz radar images of stripes with radar positioned as in Fig. 6.8 are presented. The rumble strips in (a) are clearly visible as diagonal lines on the left hand side of the image. The two wide diagonal lines starting at 12 m and 13 m on the right side of the image correspond to the kerb and the short wall on the side of the road opposite the radar, indicating a 1 m pavement between them. The linear increase of the resolution pixel size in azimuth is visible here, and is the reason for discrete presentation of linear features at a longer range. In the image of Fig.6.9 (b) the rumble strips appear more continuous due to their orientation towards the radar. Figs.6.8 (a) and (b) show a comparison of two scenarios with different angles of incidence. It is evident that the specular return from the rumble strips to the radar is expected only in the scenario of Fig.6.8(b). Here the radar beam is perpendicular to the strips. Only off-specular reflections to the radar are expected in the case of Fig.6.8(a). However, it is clear from Fig.6.9 that the power of reflections from rumble strips are similar in both scenarios. This result is a manifestation of dominant diffuse scattering at THz frequencies, even if the surface is seen as only slightly rough according to visual/optical observation. Several bright points on the left hand side in Fig. 6.9 (b) are reflections from the corners of parked cars appearing at the edge of the scanned area. The received power is normalised to 0 dB.

(a) (b)

Figure 6.8: Imaging of rumble stripes on a road at the University of Birmingham campus (a) side road radar positioning (b) the radar is positioned on the road

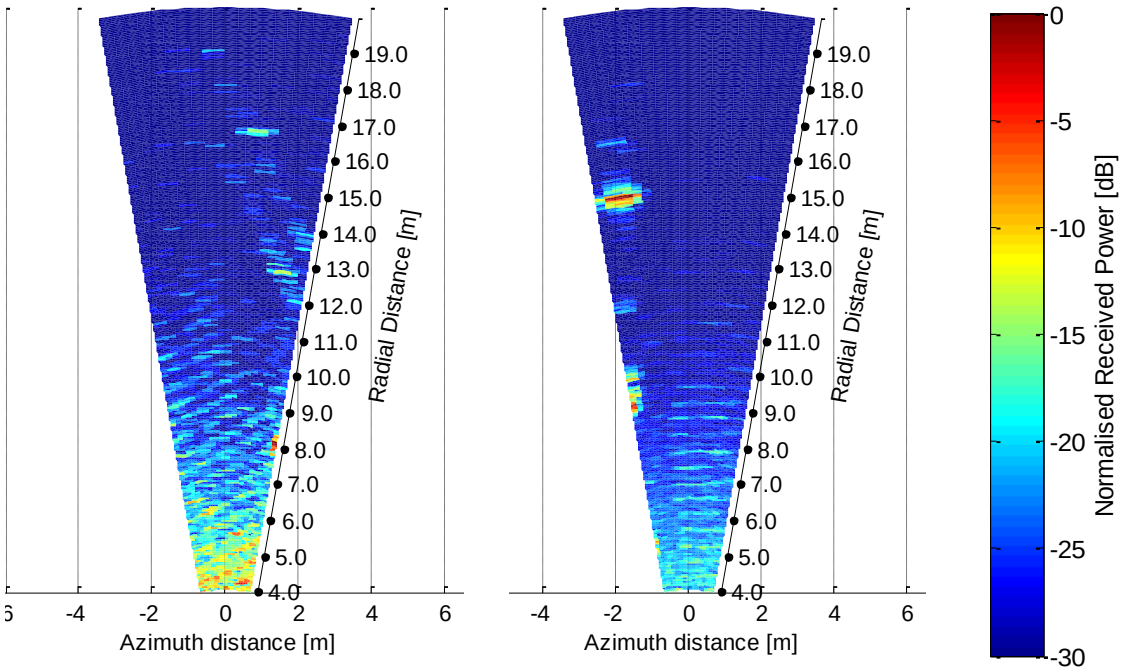

(a) (b)

Figure 6.9: (a) Image corresponding to the road scenario and radar position shown in Fig.6.8(a) Scanning at an angle to the rumble stripes; (b) Image corresponding to the scene of Fig.6.8(b) Scanning perpendicular to the rumble stripes (normal incidence).

In order to investigate the dependence of the reflectivity of rumble strip on its height, a carefully controlled experiment has been set up. Several mock rumble bars of four different heights have been made with the help of a company (Durolas LTD) specialising in road surface maintenance.

Different heights have been achieved by stacking layers of thermoplastic hot paint on a base which is commercial textured vinyl (lino) flooring; with approximate thickness of 1.1 (see Fig.6.10).

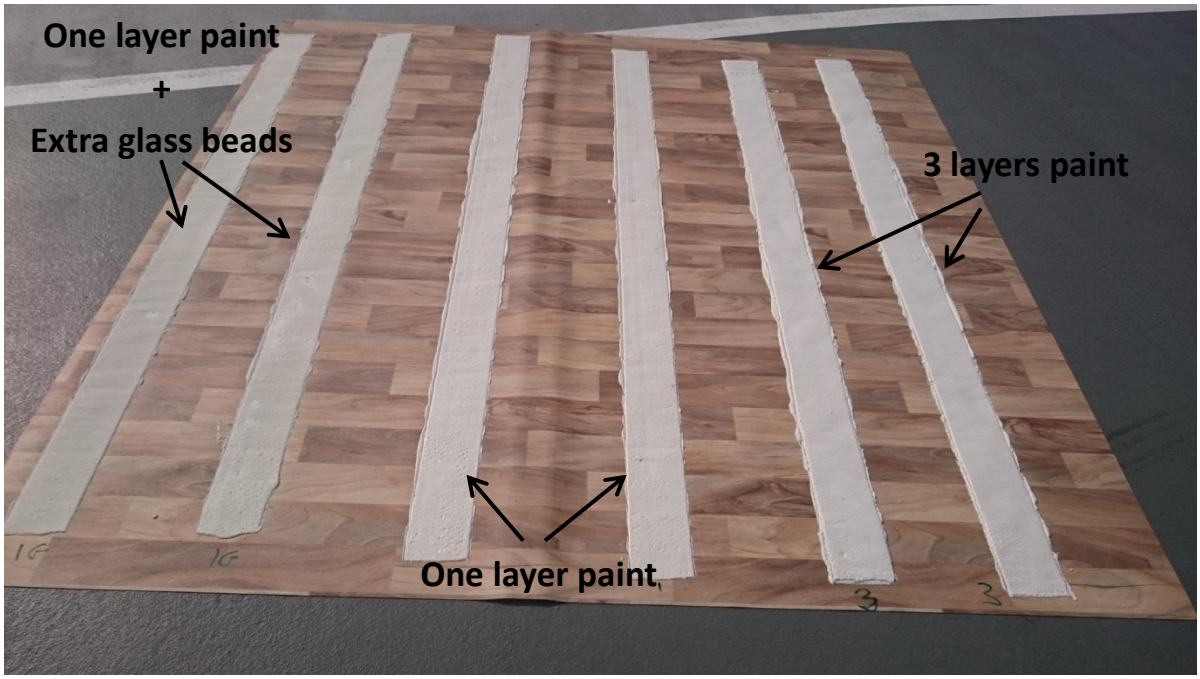

Figure 6.10: Mock rumble stripes created by stacking layers of thermoplastic hot paint on vinyl (lino) flooring.

The thermoplastic is the industrial standard material for road markings in the UK. Each layer of paint is about 2-3 mm thick. One to four layers of thermoplastic on vinyl result in approximately 4 mm, 7 mm, 10 mm and 12 mm total bar heights. Four sets of two rumble strips of 10 cm wide have been created. The purpose-made thermoplastic stripes were placed at an angle of 75 ° towards the antenna's boresight at 5-6 m range from the radar. The two rumble strips were placed approximately 30 cm apart (see Fig. 6.11).

Figure 6.11: Two Mock rumble stripes placed at the distance of 5-6 m from the radar with 75 ° angle from the bore sight to the radar. The experiments took place on the top of the multi-storey car park on the campus of University of Birmingham. The floor is painted tarmac.

6.5.1 RCS Modelling

In order to investigate the trend of the backscattering from the rumble bars depending on its height, RCS modelling has been done using MATLAB. The front face of the rumble stripe which is the reflective edge is considered as a long rectangle. The rectangle is considered to have a fixed length of 20 cm (2a= 20 cm in Fig. 6.12) equivalent to the required azimuth resolution at 5 m. The height varies in order to simulate different thicknesses of the bars, from 1 mm, 4 mm, 7 mm, 10 mm and 12 mm (see Fig. 6.12). The depression angle is about 6° replicating the experimental grazing angle. The rumble bar orientation angle is chosen around 75 ° to the line of sight in order to imitate the experimental setup. For approximating the RCS of the bar, both depression (tilt) angle and positioning angle to the line of sight in two planes should be considered. For the simulation and plotting purposes, there are two options. To keep one angle either (θ or ϕ, in Fig.6.12) fixed and plotting the RCS against the other angle variations. This approximation is based on the work reported by Ross [79]

corresponding to equation (6.1). It should be noted that this approximation is only valid for aspect angles up to 20°-30°. However, this approximation is not dependent on the polarization. This method could also be found in [18]. Equation (6.1) represents the radar cross section approximation. In Fig.6.12, 'a' is the longest side of the flat plate. It is equal to 20 cm for the illuminated length of the bars. 'b' is the height of the bar corresponding to different layers of paint.

$$\sigma = \frac{4\pi a^2 b^2}{\lambda^2}\left(\cos\theta\right)^2 \bullet \left(\frac{\sin(ak\sin\theta\cos\phi)}{ak\sin\theta\cos\phi} \bullet \frac{\sin(bk\sin\theta\sin\phi)}{bk\sin\theta\sin\phi}\right)^2 \tag{6.1}$$

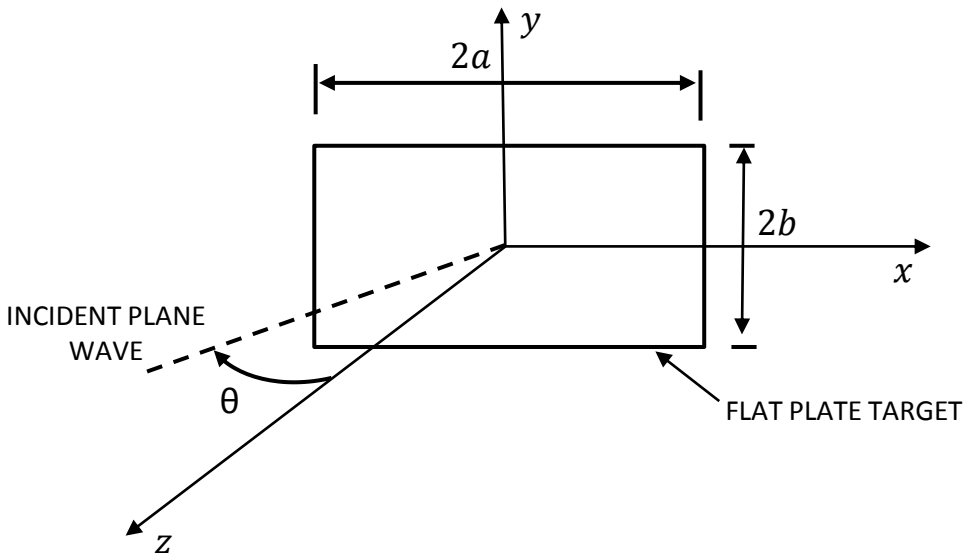

Figure 6.12: Rectangular flat plate orientation and aspect angle

Fig. 6.13 shows a plot of the RCS when the depression angle is fixed at 6° with a changing Line of Sight (LOS). If the target is tilted by 15°, it is the same as changing the LOS by 15°. Therefore, the angle between the LOS and the rectangle is 75 °. Consequently, in Fig.6.14, values at 15° for different heights are marked. These values are plotted against the normalised received power values shown in Fig.6.15.

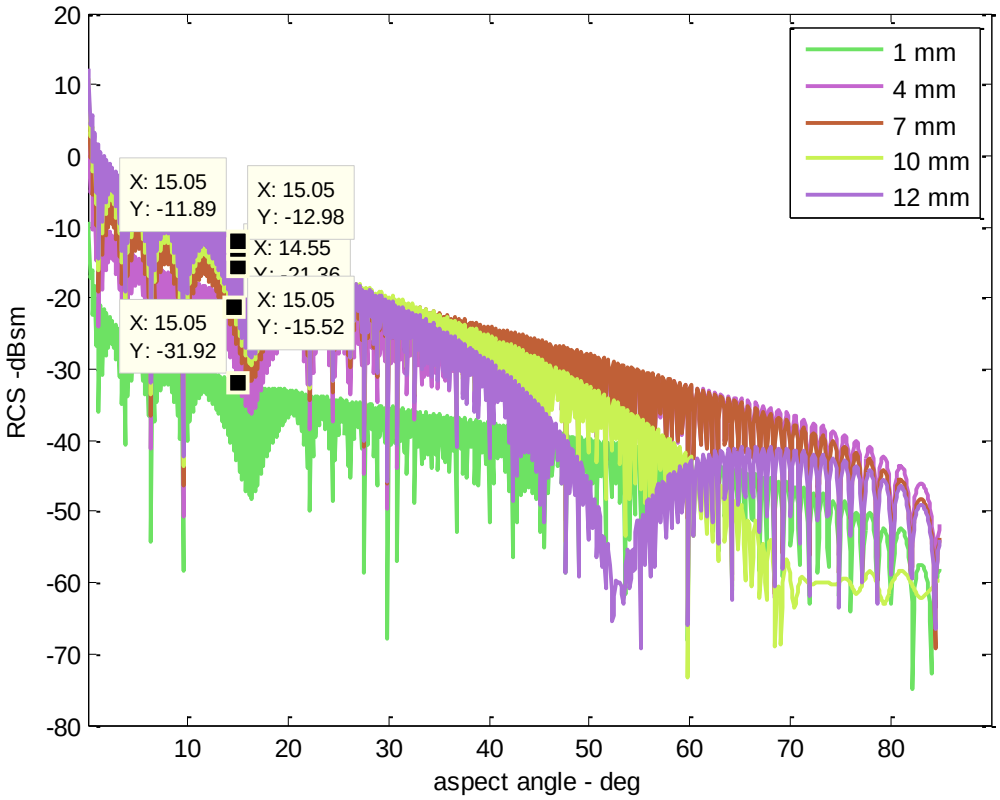

Figure 6.13: RCS estimation of rectangular flat plate with the fixed depression angle of 6 ° and plotting it according to changes in line of sight with normal(scanning angle), the 15 ° is chosen as the stripes orientation is 15°.

Fig. 6.14 shows the resulting images; the purpose made stripes are visible in all four images. The normalised received power at four different heights is plotted in Fig.6.15, and is compared to the analytical RCS approximation at 150 GHz. The received power is adjusted to minimum power in Fig.6.9 (-30 dB) in order to demonstrate the decrease in the power of reflections from the stripes.Several conclusions can be made here: (1) the strips with the smallest height (4 mm) are still visible; (2) reflection from each strip is coming from three consecutive resolution cells corresponding to the strip width. This indicates the sensitivity of the 2 mm wavelength to the difference in roughness of the floor and the material of the strip; (3) the analytical results at 30 GHz show that the reflection from the stripe's reflective facet/edge is reduced by approximately 14 dB. This decreases the visibility of the stripe dramatically. None of the strips (different heights) were visible when illuminated by 30 GHz in the reference measurements.

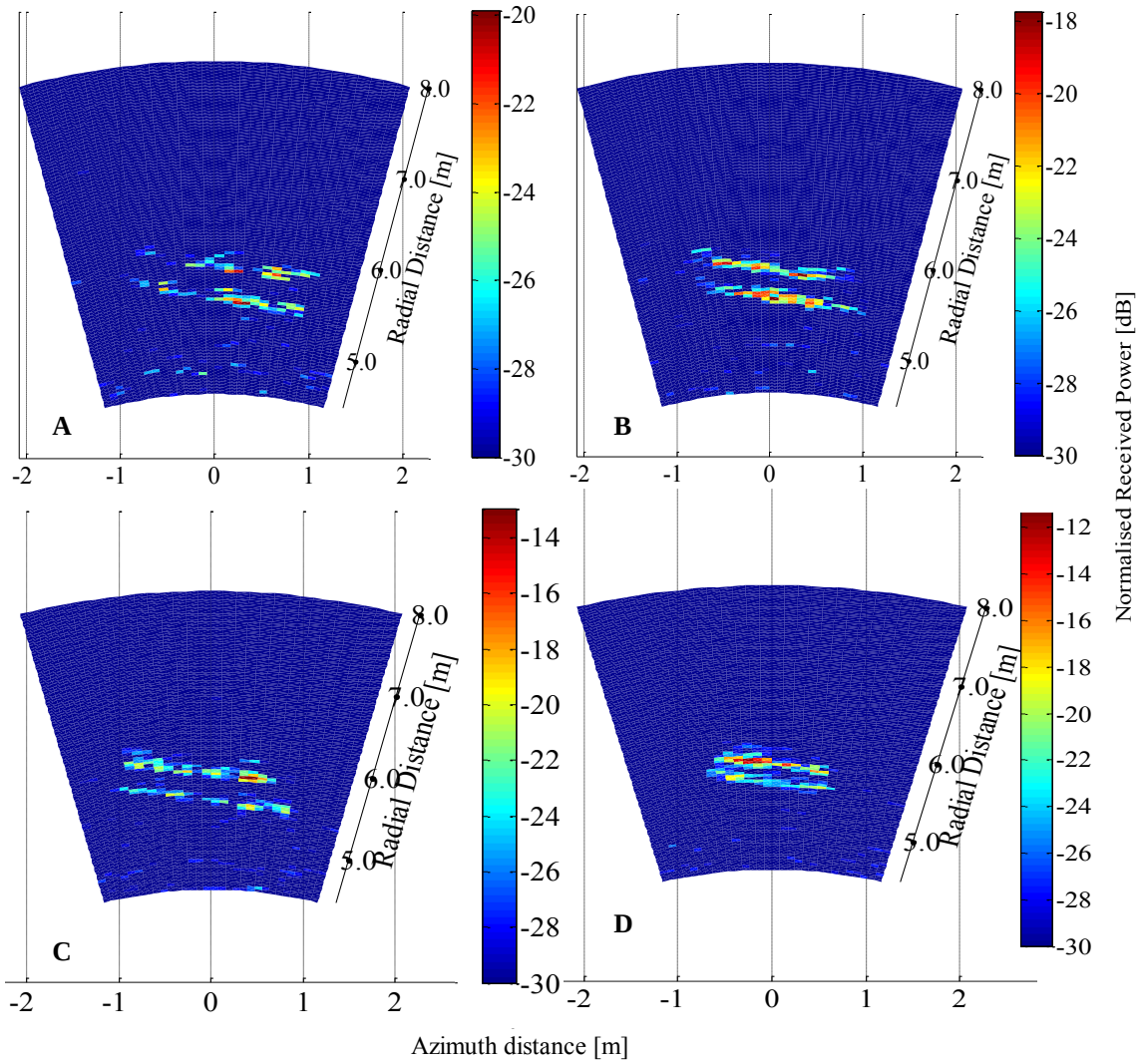

Figure 6.14: 150 GHz images of the rumble bar pairs with four different heights. (a) 4 mm (b) 7 mm (c) 10 mm and (d) 12 mm.

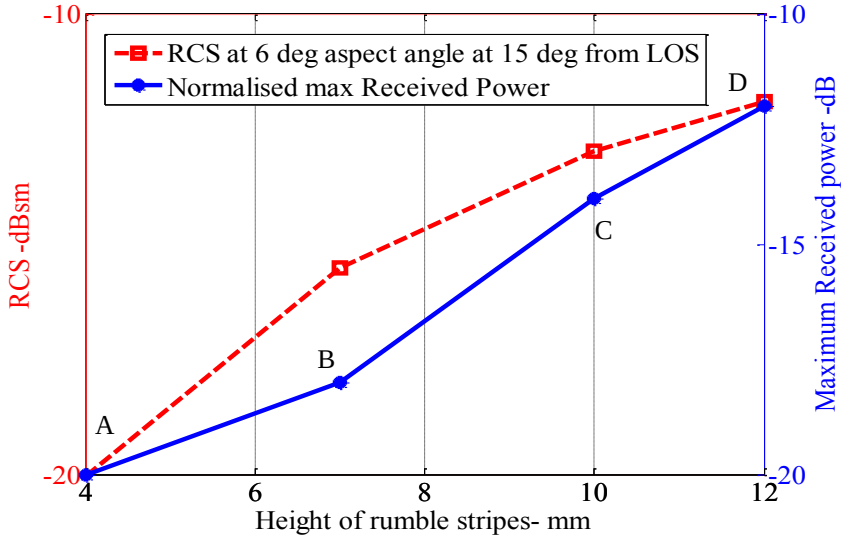

Figure 6.15: Normalised received power from rumble bars with four different heights of Fig. 6.8. The PO RCS approximation of the rumble bar with 6° depression angle of the antennas and 15 ° degree tilt of the rumble bars corresponding to radar's line of sight (LOS).

It is noteworthy that the mock rumble strips experiments took place on the top level of car park which has a relatively smooth surface compared to standard road asphalt. This is visible in a close up phot in Fig. 6.11. As a result, the background clutter from the floor creates less diffused backscattering in comparison to rough asphalt, resulting in a higher Signal to Clutter Ratio (SCR).

6.6 Pothole on the road

Fig. 6.16 shows a scene with a 5 cm deep pothole at about 6 m from the radar antennas. There are two curved walls leading to a narrow road at the distance of 12 m from the antennas. The road is scanned from -30° to +30° clockwise with 1°. The radar image made by the 150 GHz radar is shown in Fig. 6.17.

On the image shown in Fig. 6.17(a), the pothole, two curved walls indicate a pathway and the edge of Armco barriers on the far left hand side of the scene are visible. The wall is recognisable as a continuous feature at 12 m with the maximum specular backscattering at the normal incident resulting in a high intensity pixel area on the image. The Armco barrier has a large RCS because of its shape and material. It therefore appears as two high intensity points on the left hand side of the image. The pothole appears as the area of low backscattering which can be called as shadow area. This is because the depth of the pothole is not illuminated. Shadowing is briefly explained in chapter 2 in section 2.2.5. The shape and length of the pothole is identifiable from the radar image. This can be seen more clearly in the zoomed in version of the image (time gated image) shown in Fig. 6.17 (b), where a threshold has been applied to the image of Fig.17 (a). The high intensity backscattering from Armco barrier and the wall is gated out in order to represent an image with higher contrast between the background and the shadow area (pothole).

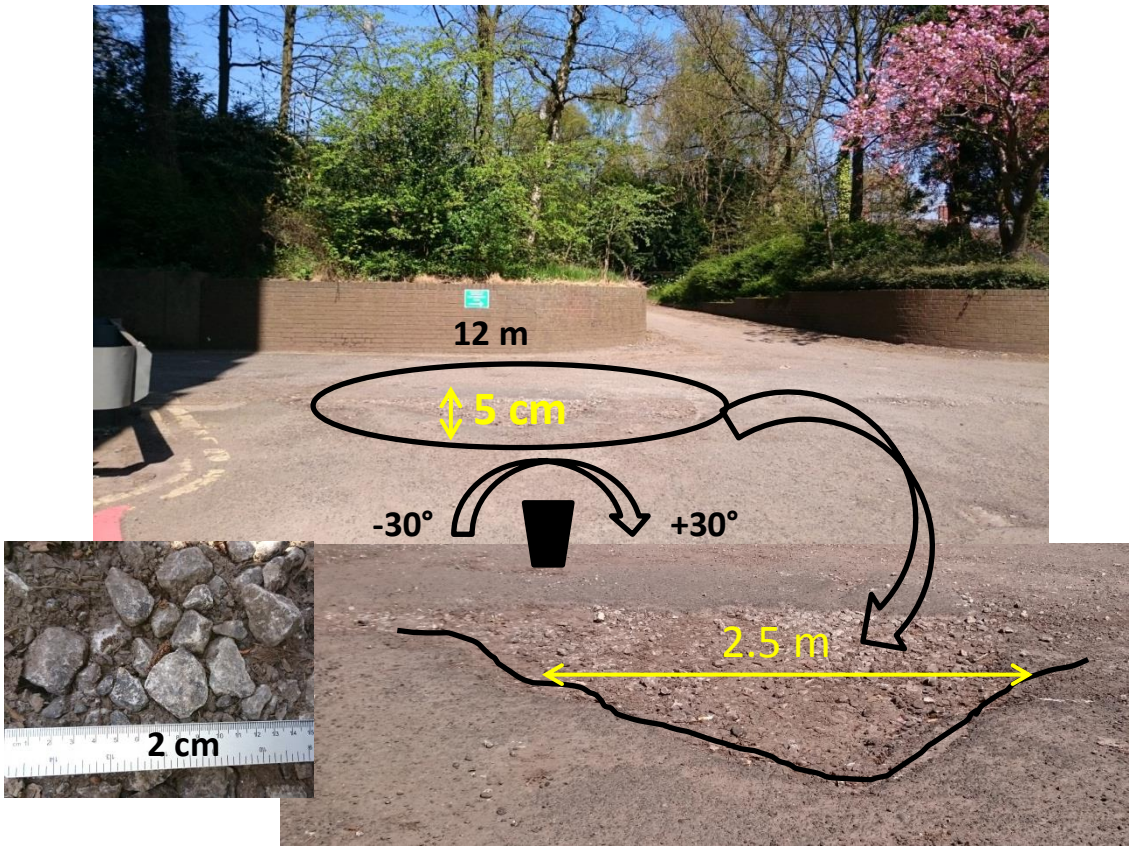

Figure 6.16: Scenario with a 5 cm deep pothole on the campus of the University of Birmingham.

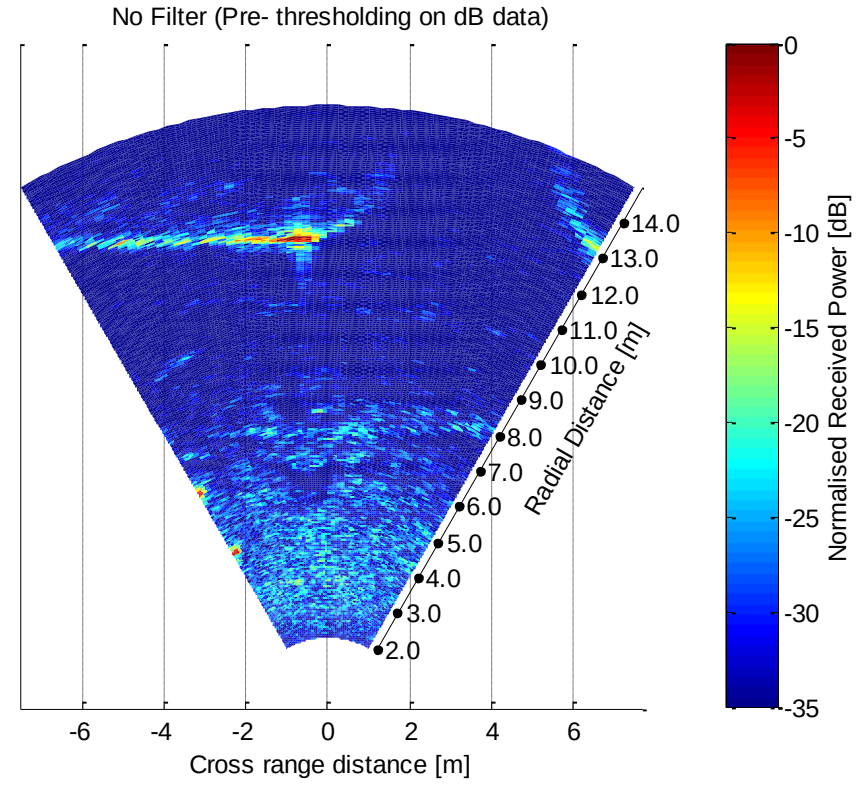

(a)

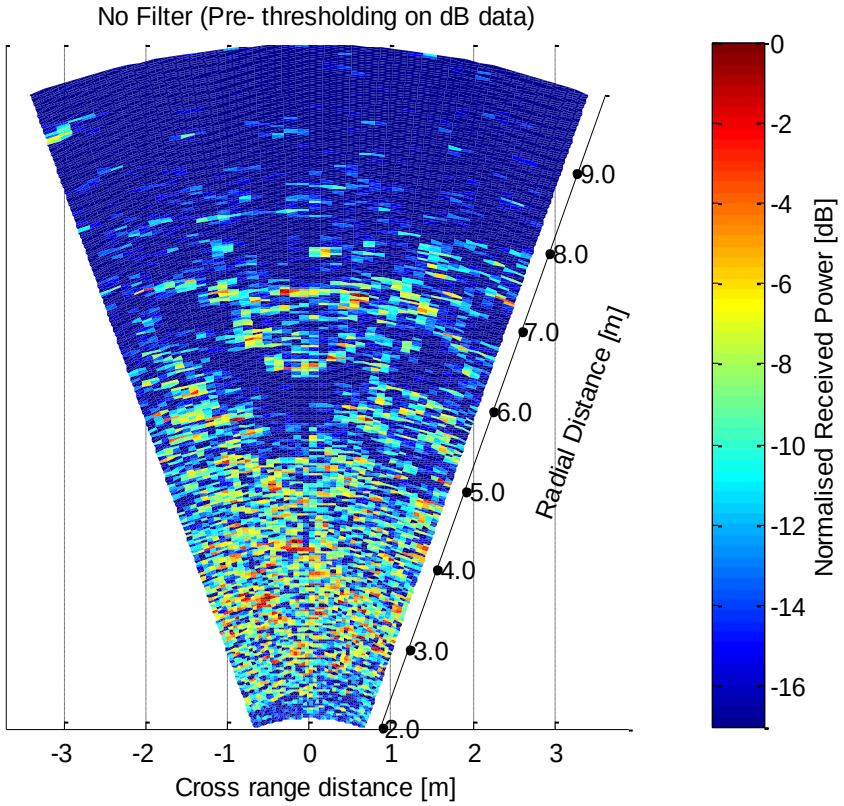

(b)

Figure 6.17: Images of the scene of Fig. 6.16. (a) Image of the full scenario (b)A threshold applied to the image (a) (zoomed in version).

6.7 Countryside (Off road) Scenarios

6.7.1 Scenario I

Fig. 6.18 shows an uneven countryside road with a ditch on the left. The photo was taken from the side of the road, while the radar has been positioned in the middle of the road, scanning over 20° on each side.

The arrows indicate profile slope changes: positive and negative angles show ascending and descending areas in respective directions along the road and the ditch. A tilted T-shaped pothole (insert) filled with water was present at the time of the radar signal acquisition between 5 and 7.5 m from the radar. Images made at 150 GHz and 30 GHz are shown in Fig. 6.19 (a) and (b), respectively. Both images clearly show road edges. However, the 150 GHz image is significantly more continuous due to a smaller range resolution and a larger diffused return.

At both frequencies, the ditch on the side of the road appears as the area of low reflectivity between the road edge and the fence. This is easily identified as the shadow region by the uniformity of the colour. It is more identifiable in the 150 GHz image.

The T-shape water filled pothole is also visible in both images as a low reflectivity area (due to specular reflection from the water surface away from radar). However, the 150 GHz image quality is significantly better and the image interpretation is easier. Identification of concave and convex objects, potholes and bumps, is the next stage of the research.

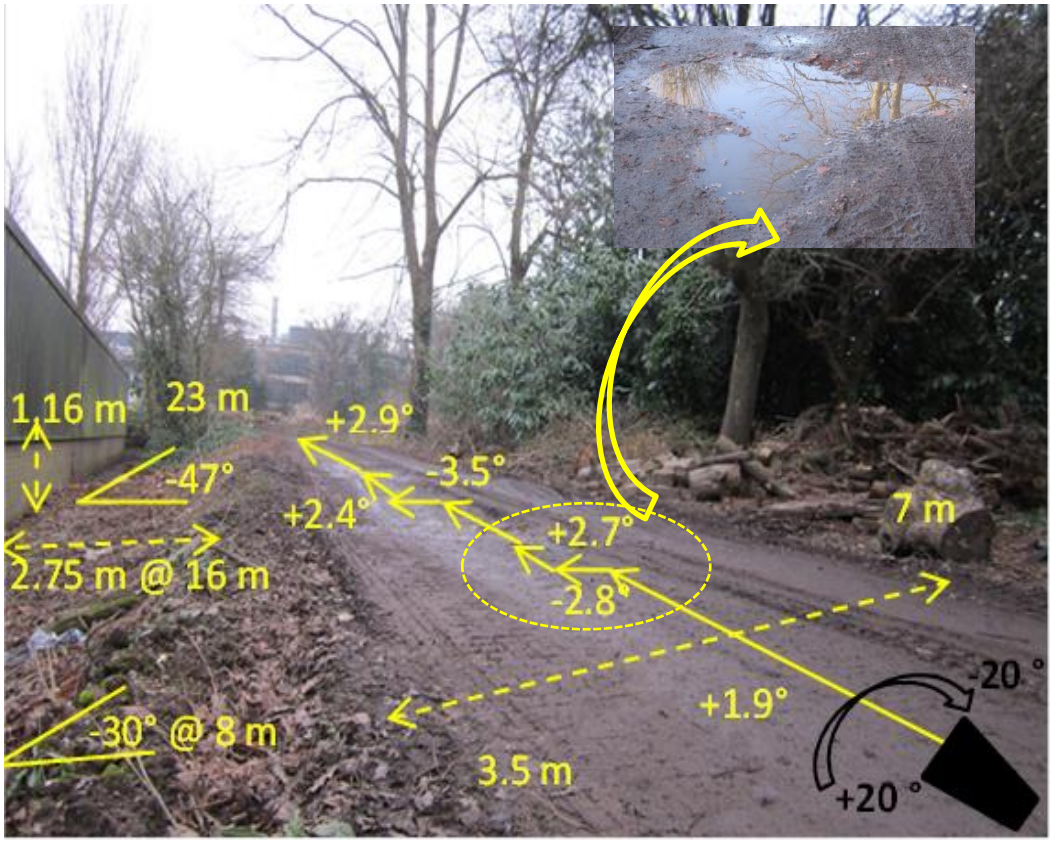

Figure 6.18: Off-Road imaged scenario

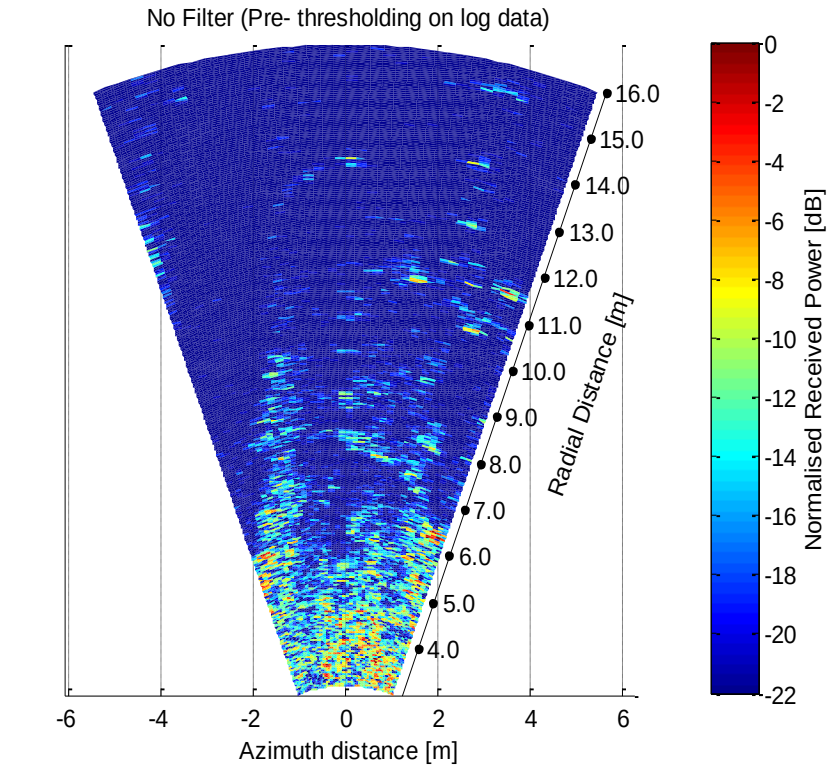

(a)

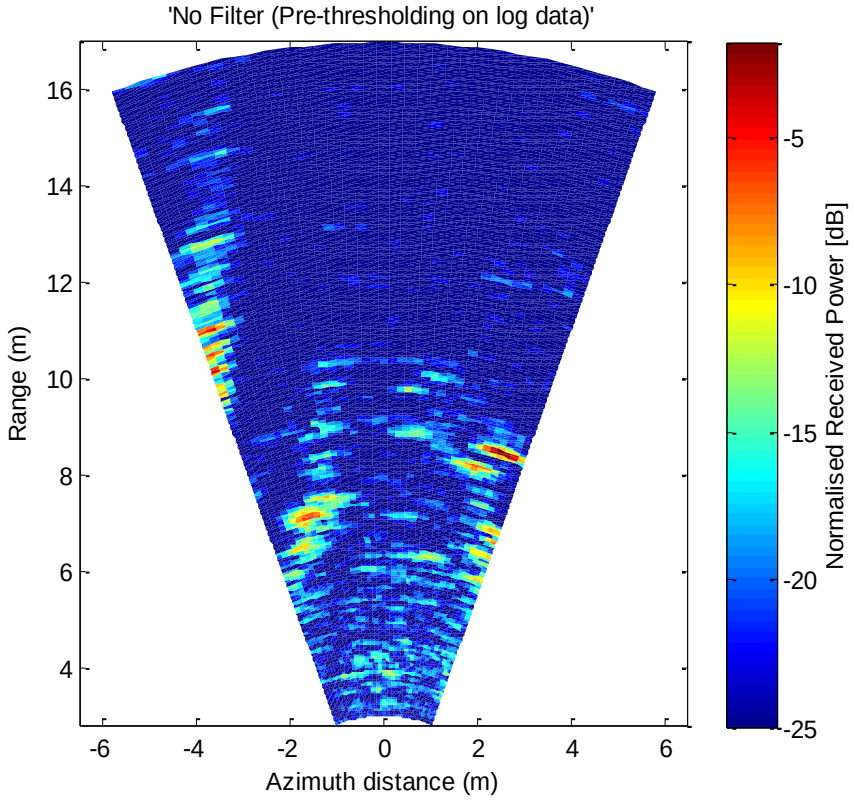

(b)

Figure 6.19: Images of the road scenario of Fig.6.18 by (a) 150 GHz FMCW radar; (b) 30 GHz stepped frequency radar

6.7.2 Scenario II

Fig. 6.20 shows an example of a countryside track. The tractor's tyre print on the muddy surface of the road creates shapes that are comparable to small corner reflectors. This results in high intensity reflections on the image at the distances of 2 m to 8 m corresponding to the reference plane of the transceiver. The 20 cm deep pothole starting from 6 m and extending to 8 m ahead of the scanning radar is the main reason this particular off-road scene is chosen for imaging. The road is scanned from -25° to +25° clockwise with 1° steps using the 150 GHz FMCW radar. The insert photo in Fig. 6.20 is an attempt to capture this relatively deep pothole with a optical camera. However, in Fig. 6.21 which shows the 150 GHz radar image corresponding to the scene of Fig.6.20, the pothole is clearly visible. The pothole is detectable as a shadow area on the radar image. The shape of the pothole is outlined as it is an extended object and occupies several resolution cells on the image. Moreover, the edges of the road are visible in the image.

Figure 6.20: Off-road imaged scenario with a pothole of 20 cm deep from 6-8 m ahead of the tranceiver

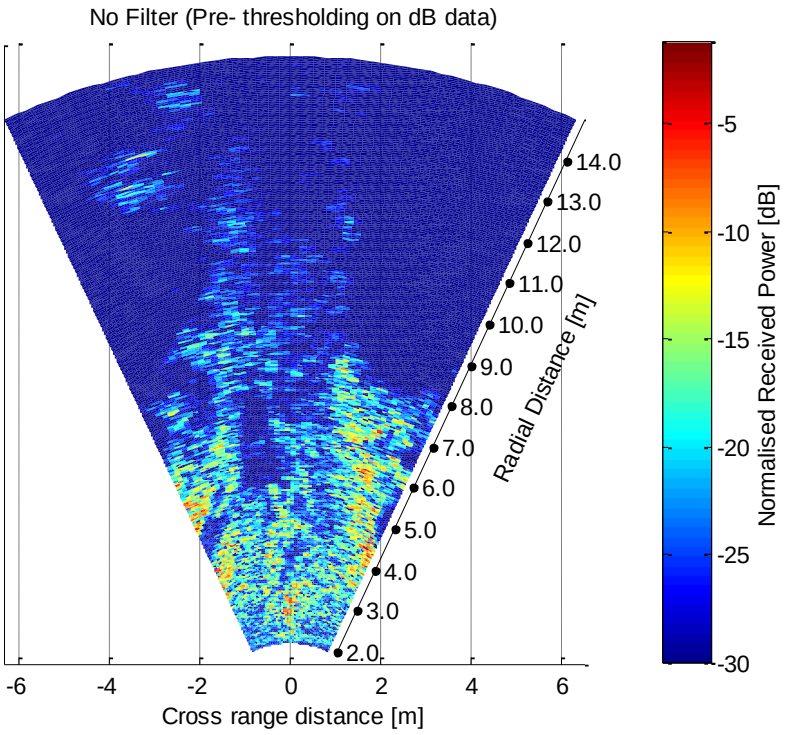

Figure 6.21: Image corresponding to the scene of Fig. 6.20. The pothole is clearly visible as a shadow area on the image.

6.8 Resolution, Precision and Accuracy of measurements

In order to quantify the imaging capabilities of the 150 GHz radar system under study, the range and azimuth Resolution, range accuracy and range Precision of the 150 GHz measurements are presented in the following section.

6.8.1 Range Resolution

In order to measure the range resolution of the 150 GHz radar for the comparison to the calculated value of 3 cm using equation (2.4), a set of measurements has been devised. Two corner reflectors (7 cm) with the RCS of 14 dBsm at 150 GHz (see Table 6.2), has been used for the purpose of these experiments. Fig. 6.22 shows the experimental setup which has been kept the same as the experiments discussed in chapter 6. The antenna elevation H is around

80 cm. The height is measured to the midpoint of Tx and Rx antennas. The grazing angle or antenna tilt angle is around 5°. The floor between the radar and target was covered with Persian carpet as well as the wall behind the target to minimize the clutter. The mid-point of the two corner reflectors is at the distance of 6.6 m from the transceiver. The corner reflectors have been placed at the distance of 50 cm apart in range and they have been moved closer in range up to 3 cm to determine the range resolution of the measurements. The measurement results with corner reflectors at the distances of 50 cm, 20 cm, 10 cm, 5 cm and 3 cm apart are presented in Fig 6.23-Fig.6.27 respectively.

(a)

(b)

Figure 6.22: (a) Measurement set up for range resolution measurements (b) two corner reflectors have been placed at 50 cm distance apart in range and they have been moved closer to each other up to 3 cm to determine the range resolution. The mid-point of the two corner reflectors is at the distance of 6.6 m from the transceiver

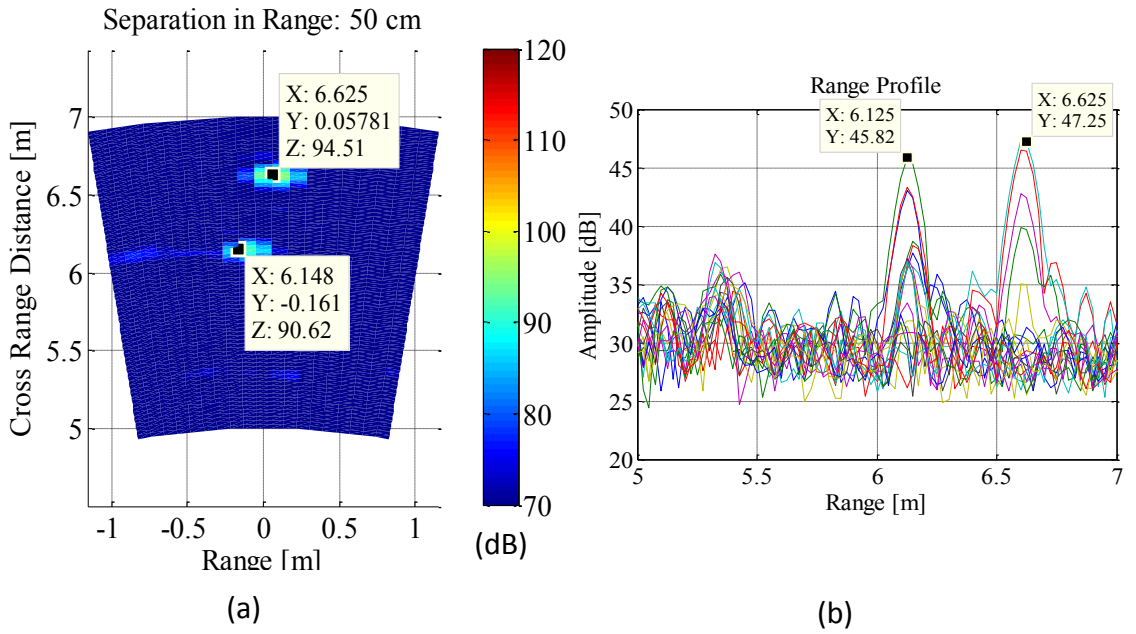

Figure 6.23: Two Corner reflectors imaged when 50 cm apart in range (a) image map (b) range profile

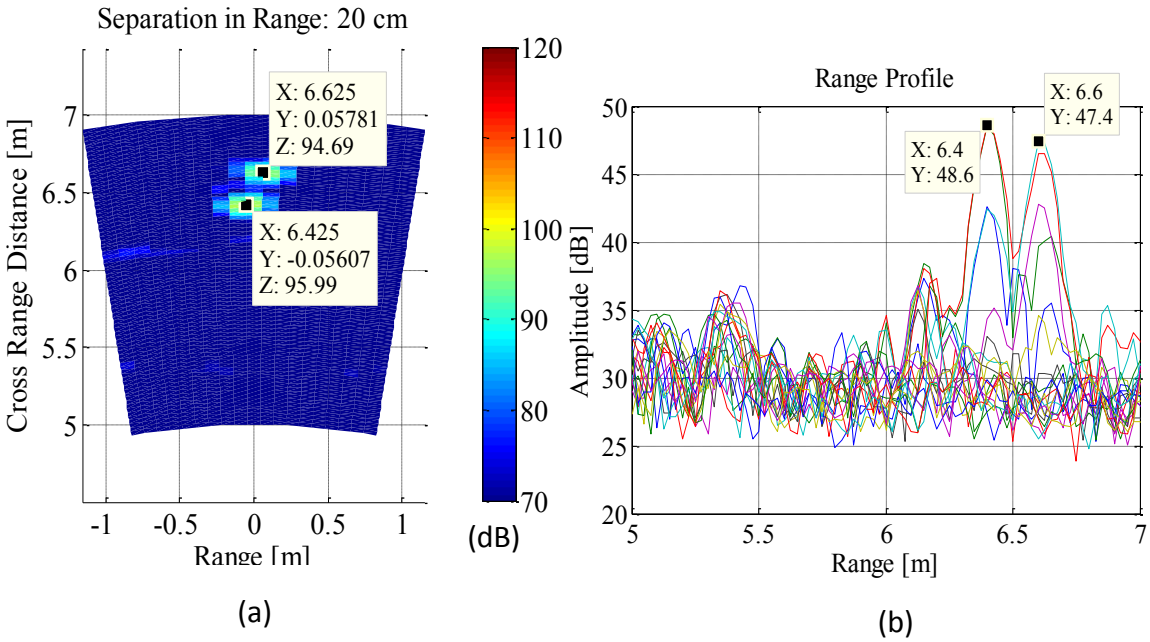

Figure 6.24: Two Corner reflectors imaged when 20 cm apart in range (a) image map (b) range profile

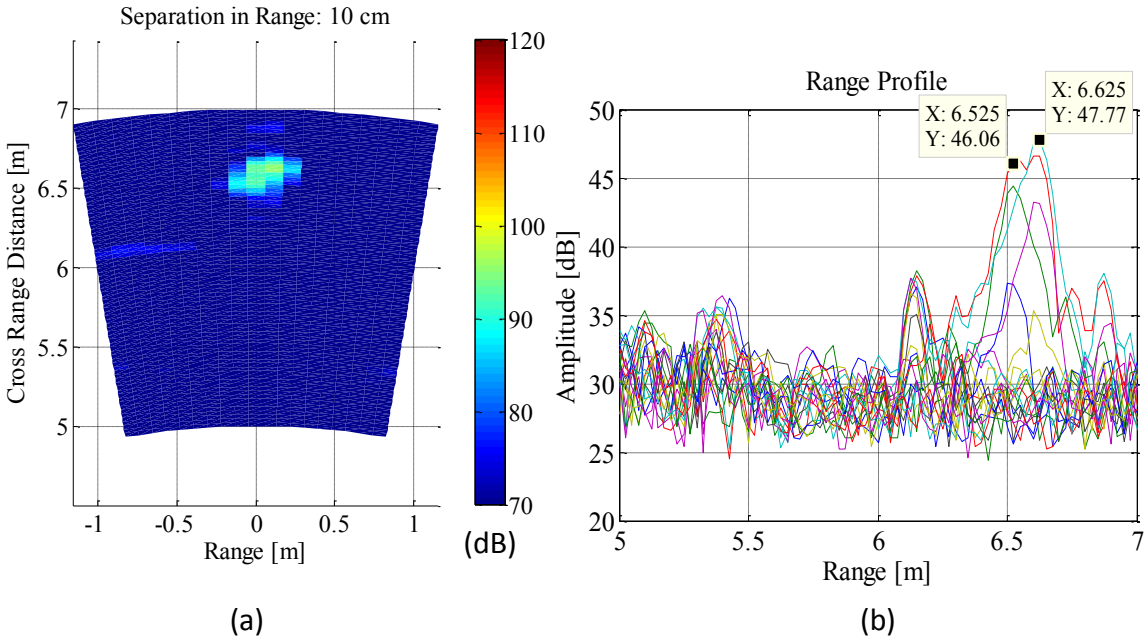

Figure 6.25: Two Corner reflectors imaged when 10 cm apart in range (a) image map (b) range profile

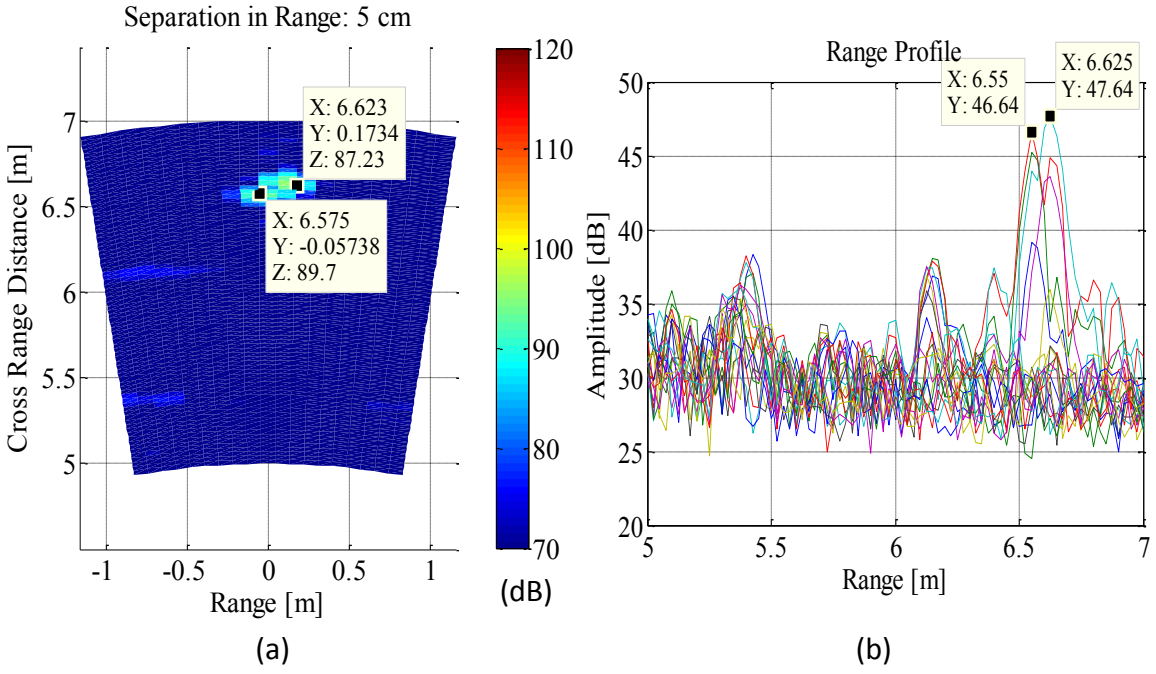

Figure 6.26: Two Corner reflectors imaged when 5 cm apart in range (a) image map (b) range profile

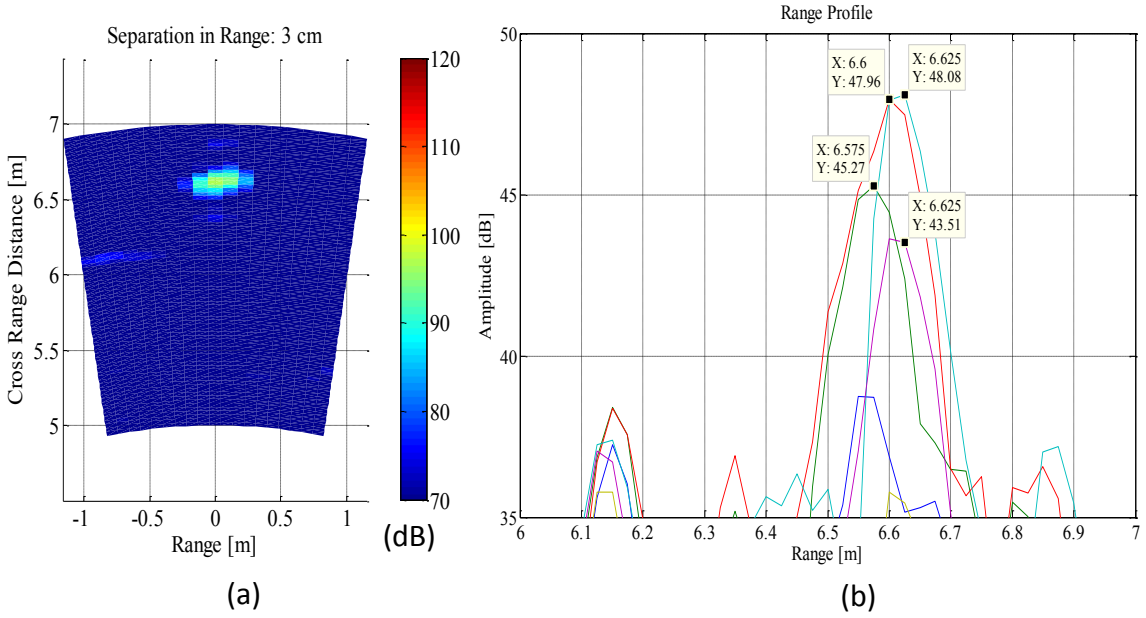

Figure 6.27: Two Corner reflectors imaged when 3 cm apart in range (a) image map (b) range profile

It can be concluded that at the range distance of 3 cm the two corner reflectors are seen as one target and are not resolved in range as two separate targets. Therefore the measured range resolution of the 150 GHz radar is larger than 3 cm (about 5 cm). The discrepancy between the calculated range resolution of 3 cm and measured value of about 5 cm is due to the fact that the range side lobes from the response from one corner reflector overlaps and masks the peak response of the other corner reflector coming from a separate range bins. The range resolution can be enhanced by using super resolution technique and applying a matched filter to the measured results. However, this is beyond the scope of this discussion as the aim is to demonstrate the imaging performance of the radar system before further processing.

6.8.2 Range Accuracy

The range accuracy is how correct the range to a single target can be determined. Accuracy can be defined as the amount of uncertainty in a measurement with respect to an absolute standard. Fig. 6.28 shows the accuracy of range measurements from a sphere with the radius of 38 mm. The range varied and was measured from 0.84 m to 14 m to the transceiver. In

each position, the actual distance measured with a tape measure and plotted against the range measured by the 150 GHz radar. One measurement was recorded by using quadrature (I and Q) data before the IF amplification stage using Picoscope to record the measurement in MATLAB for further processing (see Fig 5.8). The second set of measurements was taken after the IF amplification stage via an Ethernet cable and recorded in MATLAB. The graph of Fig. 6.28 is a comparison between the actual distance and measured distance before and after IF amplification stage. The discrepancy in the measured data after IF amplification stage is due to non-linearities of the IF amplifier observed in Fig. 5.11. It is evident from Fig. 6.28 that the measurement error in the data measured after the IF amplification increases with range while I and Q data shows a good accuracy and stability.

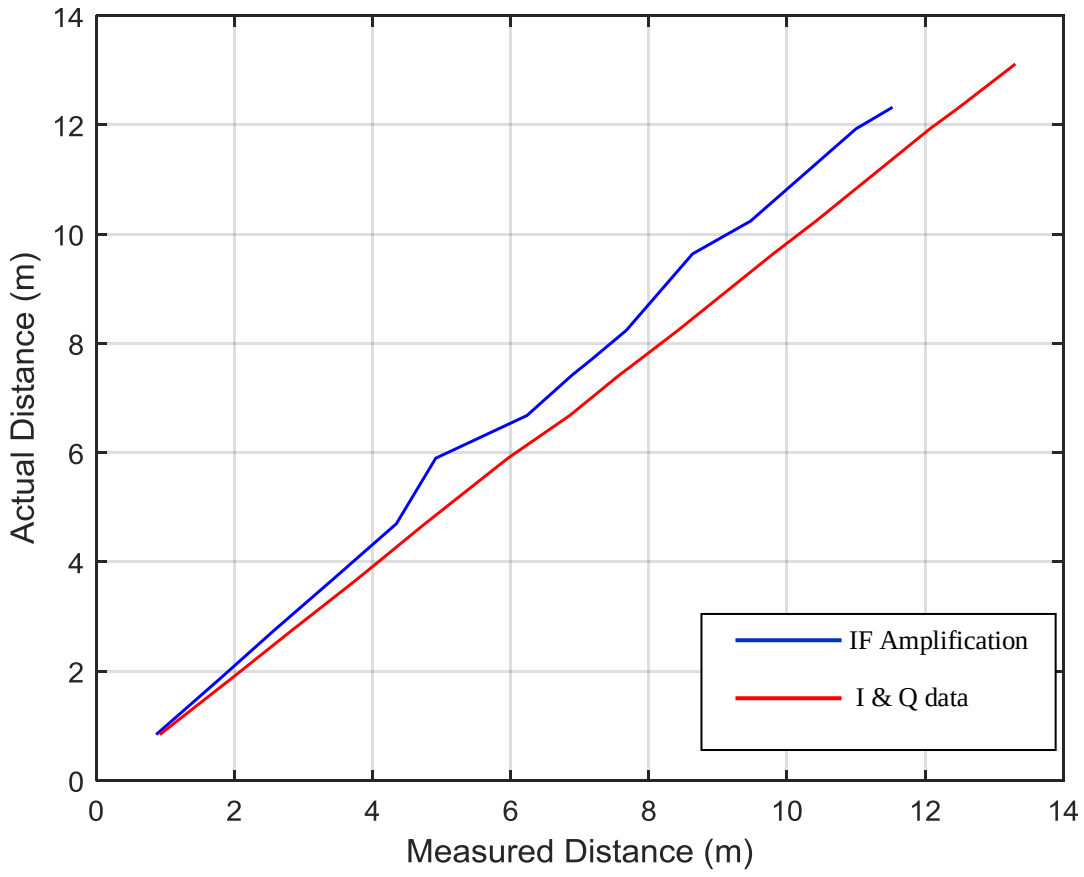

Figure 6.28: Plot of range measurements from a corner reflector using 150 GHz I and Q data extracted via Picoscope device and recorded in MATLAB is shown in red . The range measured using data recorded after IF amplification stage using Ethernet cable shown in blue. Both measurements have been plotted against the actual distance.

6.8.3 Precision (repeatability) in Range

Precision describes the reproducibility of a measurement. Fig. 6.29 shows the plot of one thousand overlaid measurements of range profiles of a corner reflector at the distance of about 5 m from the transceiver. Quadrature (I and Q) data (before the IF amplification stage) was extracted using Picoscope device and logged and processed in MATLAB. Fig. 6.29 demonstrates a very good precision in the range measurements at 5 m using the 150 GHz radar system. As can be seen, responses from the entire one thousands measurements of the corner reflector at 5 m are perfectly overlapping.

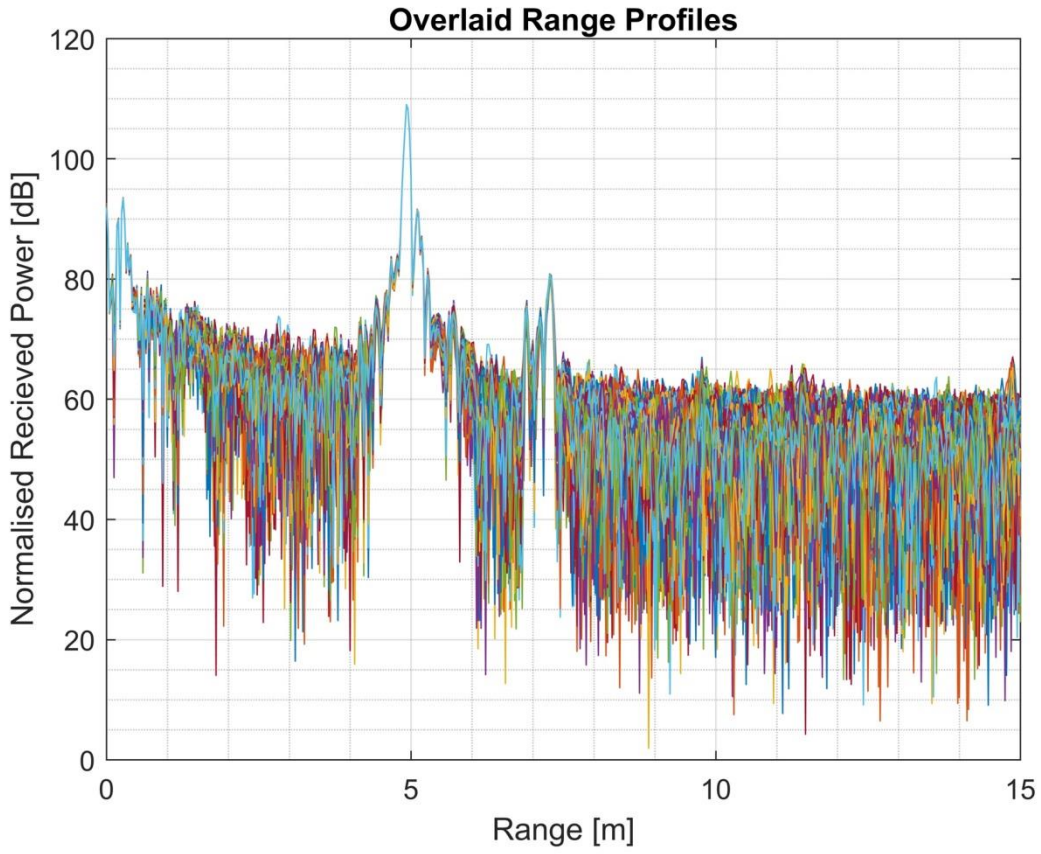

Figure 6.29: Overlaid one thousand range profile of a corner reflector at 5 m from the transceiver shows the repeatability of the range measurements

6.8.4 Azimuth Resolution and Accuracy

In order to measure the azimuth resolution of the 150 GHz radar for the comparison to the calculated value of 25 cm at 6.6 m, the following set of measurements has been done. Two corner reflectors (7 cm) with the RCS of 14 dBsm at 150 GHz (see Table 6.2) has been placed at different azimuth distances apart from one another, starting at 100 cm. They have been moved closer in azimuth to one another in order to determine the azimuth resolution. Fig. 6.30 shows the experimental setup which has been kept the same as the experiments discussed in chapter 6. The floor between the radar and target was covered with Persian carpet as well as the wall behind the target to minimize the clutter. The mid-point of the two corner reflectors is at the distance of 6.6 m from the transceiver. Measurements with corner reflectors at azimuth separation of 100 cm, 60 cm, 40 cm and 30 cm at the range of 6.6 m has been measured and presented in Fig.31 - Fig.34 respectively. The accuracy of each measurement is determined by measuring the actual distance between the two corner reflectors in azimuth measured using a tape measure and comparing it to the measured value of the 150 GHz.

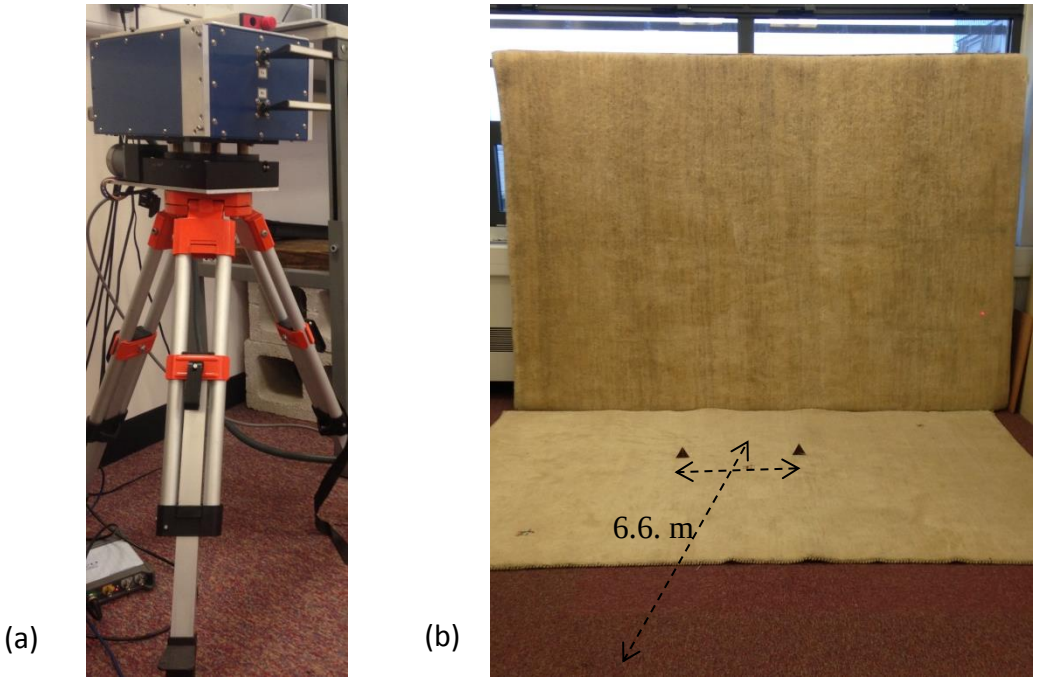

Figure 6.30: Measurement setup for azimuth resolution measurements

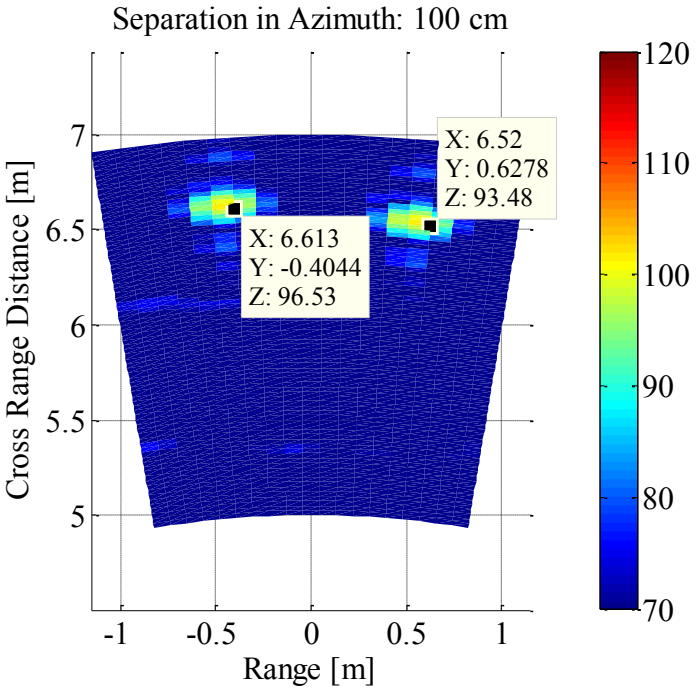

Figure 6.31: Two Corner reflectors imaged at the range of 6.6 m with azimuth separation of 100 cm

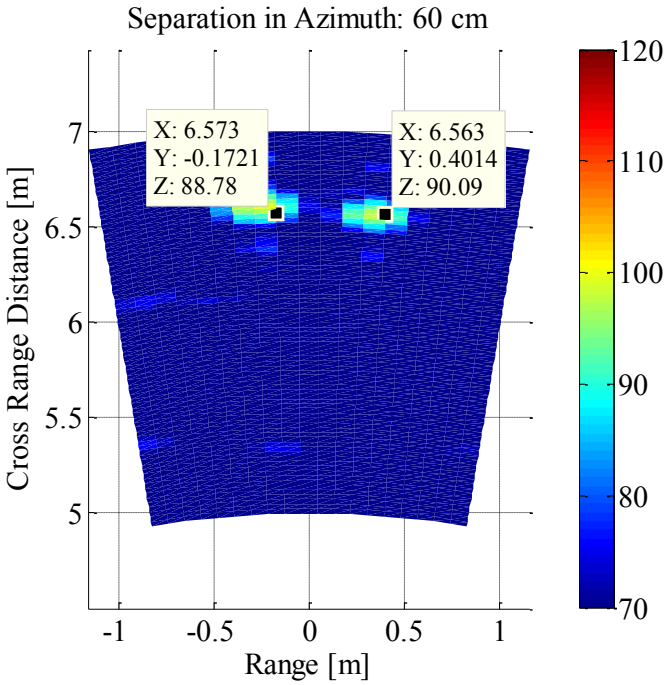

Figure 6.32: Two Corner reflectors imaged at the range of 6.6 m with azimuth separation of 60 cm

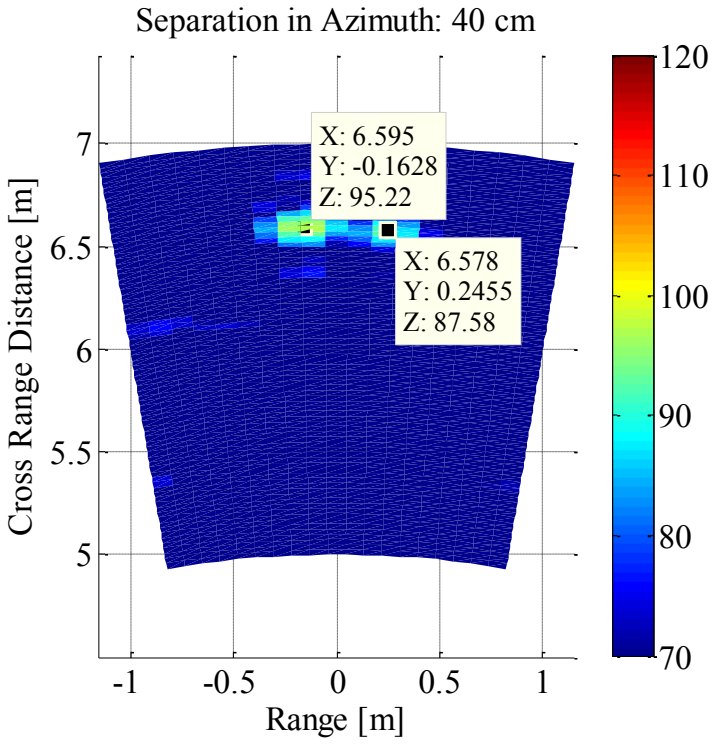

Figure 6.33: Two Corner reflectors imaged at the range of 6.6 m with azimuth separation of 40 cm

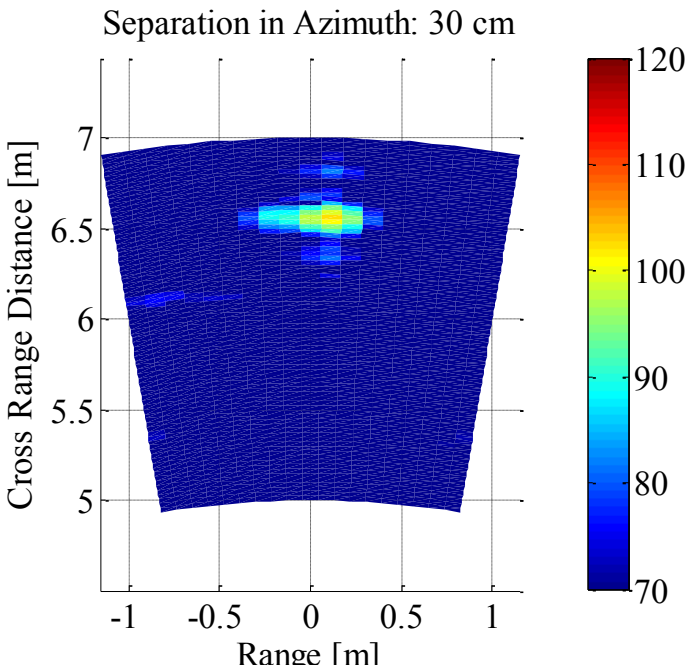

Figure 6.34: Two Corner reflectors imaged at the range of 6.6 m with azimuth separation of 30 cm

It can be concluded that the two corner reflectors are not resolved at the azimuth distance of 30 cm and therefore the azimuth resolution is larger than 30 cm at 6.6 m, as opposed to the calculated value of 25 cm. The discrepancy between the measured and calculated value is due to the measurements error, inaccurate measurements of the antenna two way azimuth beam width in range and the overlap in the sidelobes of the antenna patterns.

The accuracy of the measurements shown in Fig. 31-Fig. 34 can be defined by the amount of the measurement error in each measurement. The overall accuracy of measurements is found by averaging the measurement error for each of the measurements which is found to be 22 mm for the measurements taken in this experiment. Ideally, to define the accuracy, a large number of measurements at different distances are required.

6.9 Conclusions and Summary

1. The detection of road features and texture depends on the Signal to Clutter Ratio (SCR) and the contrast of different pixel areas of the image to the adjacent clusters. Fig. 6.35 describes the profile of an arbitrary road with bumps, potholes and flat sections. In Fig.6.35, only the shape of the road profile is taken into account and the effect of material and texture is neglected. For a fixed antenna elevation and grazing angle, it can be concluded that raised features and objects possess a large value of RCS and therefore they result in high intensity of reflection on the image. In this case, the flat road is the background or clutter with average strength of backscattering. The areas of very low reflection caused by potholes, ditches and puddles are recognised as low return areas or shadow areas on the image as described in section 2.2.5.

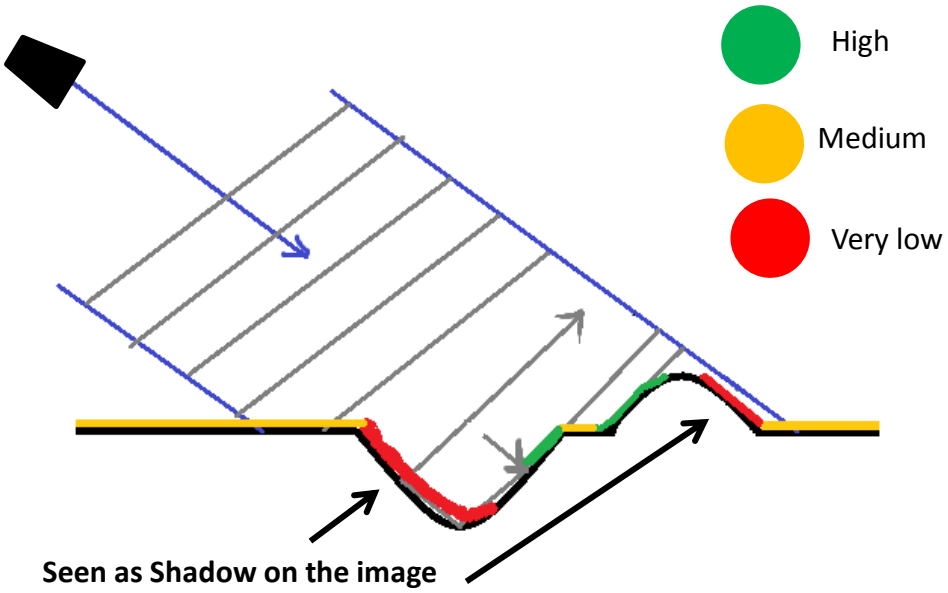

Figure 6.35: Simplified profile of an arbitrary road. Detecting features by the intensity of return on the image

2. The depth of potholes or height of the raised features can be estimated by deploying interferometric techniques using a third receiver and phase information which is the subject of future work [3].
3. Distinguishing low return areas from one another remains a challenge in the context of the 150 GHz imaging radar. In the radar images presented in this chapter, the pothole, ditch and puddle (water filled pothole) are identified as areas of low reflection. In the case of the ditch and the potholes, this is owing to a lack of illumination. For the puddle, the mirror-like surface of the still water is causing the specular reflection away from the transceiver; thus resulting in low return.
4. In order to quantify the imaging capabilities of the 150 GHz radar system under study the range and azimuth resolution, range accuracy and range precision of the 150 GHz measurements were demonstrated in section 6.8. The measured range accuracy at 150 GHz demonstrates that the measurement error in the data measured after the IF amplification stage increases with range while directly recorded quadrature signals (I and Q data) shows a good accuracy and stability. The measurements presented in this study are recorded after IF amplification stage. The range repeatability measurements demonstrate a very good precision in the range measurements using the 150 GHz radar system.

7. Conclusions and Future work

7.1 Conclusions

A comparison of experimental images of on-road and off- road scenarios made by a 150 GHz FMCW radar and a reference 30 GHz stepped frequency radar is made, and their performance is analysed.

The initial 150 GHz experimental results demonstrate the potential of a low-THz radar sensor to deliver high resolution images of the road environment, owing to its sensitivity even to slight roughness and texture of imaged objects. The texture sensitivity of the radar under study makes the proposed front end sensor technology feasible to be used for surface identification and classification in on-road and off- road environments [80].

The imaging results demonstrate an enhancement to the quality of the radar images with the increase of frequency from microwaves towards the optical region. Moving from microwave frequencies (30 GHz) to low –THz band (150 GHz), results in a decrease of the wavelength (by five times from 10 mm to 2 mm). This leads to stronger diffused backscattering and therefore increased texture sensitivity. It was demonstrated that the radar images produced by a radar system operating at 150 GHz are unlike typical radar images and they resemble an optical image.

As stated in the introduction chapter, the main aim of developing radar systems operating at low-THz frequencies is to collect more information from the road environment. It was demonstrated that the 150 GHz images provide more information about features and objects of interest. After comparing the 30 GHz and 150 GHz images, it can be concluded that in the 150 GHz images, the extended objects are outlined more clearly than in the low-frequency images. The extended objects and lines are seen as continuous. For example the curvature of

the kerb is measureable, whereas in the 30 GHz radar image, it appeared as scattered spots, which is to be expected from a classical radar image.

Table 6.1 summarises the key parameters of the 150 GHz and 30 GHz radar systems, while additional parameters are presented in Table 5.1 and table 4.3, respectively. In order to evaluate the effect of each parameter on imaging capabilities of two radar systems under comparison, all except parameter under investigation should be set the same. Therefore in the case of the radar systems under study, the images produced by both radar systems cannot be directly compared to one another due to differences in several key parameters such as bandwidth and antenna beam widths, which cannot be changed for the designed systems. However, it can be concluded that the 150 GHz radar images owe their enhancement in comparison to 30 GHz radar images to the following factors:

1. Enhanced angular resolution achieved by using slightly narrower antenna beam in azimuth [see equation (2.5)].

2. Enhanced range resolution achieved by larger measurement bandwidths [see equation (2.4)].

3. Higher texture sensitivity as a result of an increase in diffuse scattering from surfaces due to shorter wavelengths enhancing sensitivity to small surface irregularities [see equation (2.1)]. This is because of shorter wavelengths of transmitted signals (2 mm at 150 GHz as opposed to 10 mm at 30 GHz).

According to equation (5.1), other parameters such as transmit power, Tx and Rx antenna gain can increase the intensity of the received power and therefore increase the instrumental range of the radar. However, they wouldn't play a part in defining the imaging capabilities of a radar system.

7.2 Future research and development

By going up to the doubled frequency bands of 300 GHz and 670 GHz in the next stage of this research, the resolution and texture sensitivity of the images are expected to increase further. Such frequency bands are selected because they fall in the area of low attenuation between two absorption peaks in the spectrum (see Fig. 2.4). However, the signal attenuation through different media should be investigated thoroughly [5] [34]. This is the subject of research work taking place at the University of Birmingham THz Laboratory where, the influence of contamination on the sensor radome is investigated for outdoor environments, by taking various weather (rain, snow, fog, etc.) and road conditions into account. Characterising the attenuation of low-THz signal through the radome covered with different materials such as mud, water droplets, wet leaves and etc. is a pre-requisite for the development of Low-THz radar sensors for practical automotive use [81] .

Azimuth refinement

In the measurement results presented in this thesis, the objects of interest were placed at distances of up to 20 m where azimuth resolution is about 0.8 m in regards to the transceiver reference plane. Therefore, the images were time gated to suit the desirable display range. However, as defined in chapter 1, the required maximum operational range for the medium range imaging radar intended for automotive applications is up to 100 m. The azimuth resolution of the current prototype antennas at 100 m is about 4 m, which should be compared to the width of a lane. In order to maintain the fine azimuth resolution at further distances to the transceiver, azimuth refinement methods such as digital beam sharpening should be explored. This is the subject of future research work [3] .

- After few attempts at different grazing angles and radar platform heights, detecting road humps still remains a challenge at 150 GHz; because there is no significant

reflective edge or texture contrast of the hump in comparison to the flat road. The gradual increase of the surface height over the range which peaks at the crest of the hump (maximum 10 cm) does not result in high amplitude values of the backscattered signal. Therefore, an interferometric approach should be investigated to obtain information about the height of objects and road features.

- In chapter 6, it was demonstrated that the rumble strips are detectable using the 150 GHz FMCW radar owing to the height and material of the layer of the thermoplastic paint. The feasibility of imaging the road markings at operating frequencies of around 300 GHz should be explored. ISAR imaging of road markings at the frequency of 300 GHz over a few hours of integration time for mobile mapping applications has been published recently [82, 83]. Although the results are encouraging and demonstrate the capabilities of the front end sensor, the ISAR imaging technique is not applicable to forward looking radars for automotive applications. Moreover, such a long integration time is not possible for automotive applications.
- This thesis is concerned with image formation. The next step after obtaining the images is image interpretation by applying image processing algorithms for classifying objects and road features. A vast legacy of image processing algorithms used for processing of optical images can be explored for feature extraction. For instance the Hough transform is a method that is used for linear feature detection, for example detecting the road edges [2].

Although pedestrian detection and classification has been studied extensively at conventional automotive frequencies [84], they have not been explored at the Low-THz frequency band of 150 GHz and 300 GHz. This is a subject of further study which is taking place as a PhD project at the THz laboratory, University of Birmingham.

Appendix A. Publications

Journal papers

D. Jasteh, E. G. Hoare, M. Cherniakov, and M. Gashinova, "Experimental Low-Terahertz Radar Image Analysis for Automotive Terrain Sensing," *IEEE Geoscience and Remote Sensing Letters*, vol. 13, pp. 490-494, 2016.

G. Kun-Yi, E. G. Hoare, **D. Jasteh**, S. Xin-Qing, and M. Gashinova, "Road Edge Recognition Using the Stripe Hough Transform From Millimeter-Wave Radar Images," *Intelligent Transportation Systems, IEEE Transactions on*, vol. 16, pp. 825-833, 2015.

Conference papers

D. Jasteh, E. G. Hoare, M. Cherniakov, and M. Gashinova, "Experimental Low-Hz radar image analysis for automotive terrain sensing," *IEEE Geoscience and Remote Sensing Letters*, 2015. **Presented in THz session of the 16th International Radar Symposium [Dresden, June 2015].**

D. R. Vizard, M. Gashinova, E. G. Hoare, **D. Jasteh**, L. Daniel, M. Cherniakov, T. Y. Tran, and N. Clarke, "Antenna range evaluations of low THz imagers for automotive applications," in *Antenna Measurements & Applications (CAMA), 2014 IEEE Conference on*, 2014, pp. 1-4.

References

[1] E. NCAP. (2016, 21 May). *The European New Car Assessment Programme (Euro NCAP)* Available: http://www.euroncap.com/en

[2] G. Kun-Yi, E. G. Hoare, D. Jasteh, S. Xin-Qing, and M. Gashinova, "Road Edge Recognition Using the Stripe Hough Transform From Millimeter-Wave Radar Images," *Intelligent Transportation Systems, IEEE Transactions on*, vol. 16, pp. 825-833, 2015.

[3] P. G. M. Gashinova, M. Cherniakov, "TASCC: Pervasive low-TeraHz and Video Sensing for Car Autonomy and Driver Assistance (PATH CAD)," ed. University of Birmingham: EPSRC, 2015.

[4] D. Jasteh, E. G. Hoare, M. Cherniakov, and M. Gashinova, "Experimental Low-Terahertz Radar Image Analysis for Automotive Terrain Sensing," *IEEE Geoscience and Remote Sensing Letters*, vol. 13, pp. 490-494, 2016.

[5] F. Norouzian, F. Qi, B. Willetts, M. Gashinova, C. Constantinou, P. Gardner, E. Hoare, and M. Cherniakov, "Characterisation of attenuation at low THz frequencies in radar sensors," in *Radar Conference (EuRAD), 2015 European*, 2015, pp. 101-104.

[6] P. Laboratory of Terahertz Spectroscopy. (2014, 20 July). Available: http://lts.fzu.cz/en/intro.htm

[7] R. Rasshofer and K. Gresser, "Automotive radar and lidar systems for next generation driver assistance functions," *Advances in Radio Science*, vol. 3, pp. 205-209, 2005.

[8] T. Denton. (2015). *Stereo Video Camera*. Available: http://www.automotive-technology.co.uk/?p=2376

[9] S. Yamano, H. Higashida, M. Shono, S. Matsui, T. Tamaki, H. Yagi, and H. Asanuma, "76GHz millimeter wave automobile radar using single chip MMIC," *Fujitsu Ten Tech. J*, pp. 12-19, 2004.

[10] A. Jenkins, "Remote Sensing Technology for Automotive Safety-Development and deployment of millimeter-wave-based technology for remote sensing applications in vehicles," *Microwave Journal; International ed*, vol. 50, p. 24, 2007.

[11] D. R. Vizard, M. Gashinova, E. G. Hoare, and M. Cherniakov, "Low THz automotive radar developments employing 300–600 GHz frequency extenders," in *2015 16th International Radar Symposium (IRS)*, 2015, pp. 209-214.

[12] D. R. Vizard, M. Gashinova, E. G. Hoare, D. Jasteh, L. Daniel, M. Cherniakov, T. Y. Tran, and N. Clarke, "Antenna range evaluations of low THz imagers for automotive applications," in *Antenna Measurements & Applications (CAMA), 2014 IEEE Conference on*, 2014, pp. 1-4.

[13] C. Caraffi, S. Cattani, and P. Grisleri, "Off-Road Path and Obstacle Detection Using Decision Networks and Stereo Vision," *Intelligent Transportation Systems, IEEE Transactions on*, vol. 8, pp. 607-618, 2007.

[14] T. Kato, Y. Ninomiya, and I. Masaki, "An obstacle detection method by fusion of radar and motion stereo," in *SICE 2003 Annual Conference*, 2003, pp. 689-694.

[15] M. Siegel and R. MacLachlan, "Radar obstacle detection: finding moving targets in noisy range data," in *Instrumentation and Measurement Technology Conference, 2002. IMTC/2002. Proceedings of the 19th IEEE*, 2002, pp. 145-150 vol.1.

[16] M. I. Skolnik, *Introduction to radar systems*, 2nd ed. ed. New York ; London: McGraw-Hill, 1980.

[17] P. White, "Radar Waveforms for A&D and Automotive Radar White Paper."

[18] M. I. Skolnik, *Radar handbook*, 3rd ed. ed. Maidenhead: McGraw-Hill Professional, 2008.

[19] G. W. Stimson, *Introduction to airborne radar*, 2nd ed. ed. Mendham, N.J.: SciTech Pub, 1998.
[20] M. Jankiraman, *Design of multi-frequency CW radars*: SciTech Publishing, 2007.
[21] A. G. Stove, "Linear FMCW radar techniques," *Radar and Signal Processing, IEE Proceedings F*, vol. 139, pp. 343-350, 1992.
[22] T. S. Rappaport, *Wireless communications : principles and practice*, 2nd ed. ed. Upper Saddle River, N.J. ; [Great Britain]: Prentice Hall PTR, 2002.
[23] M. A. e. Richards, J. e. Scheer, W. A. e. Holm, and W. L. e. Melvin, *Principles of modern radar*.
[24] J. A. Richards, *Remote sensing with imaging radar*. Heidelberg: Springer, 2009.
[25] A. E. Fuhs, *Radar cross section lectures*: American Institute of Aeronautics and Astronautics, 1984.
[26] I. Harre, "RCS in radar range calculations for maritime targets," *Bremen, Germany, available online at http://www. mar-it. de/Radar/RCS/RCS_xx. pdf*, 2004.
[27] B. R. Mahafza and A. Elsherbeni, *MATLAB simulations for radar systems design*: CRC press, 2003.
[28] K. B. Cooper, R. J. Dengler, N. Llombart, B. Thomas, G. Chattopadhyay, and P. H. Siegel, "THz Imaging Radar for Standoff Personnel Screening," *Terahertz Science and Technology, IEEE Transactions on*, vol. 1, pp. 169-182, 2011.
[29] D. R. Wehner, *High-resolution radar*, 2nd ed. ed. Boston, Mass. ; London: Artech House, 1995.
[30] J. Fritz, L. Scally, A. J. Gasiewski, and Z. Kun, "A sub-terahertz real aperture imaging radar," in *Radar Conference, 2014 IEEE*, 2014, pp. 1165-1169.
[31] R. W. McMillan, "TERAHERTZ IMAGING, MILLIMETER-WAVE RADAR," in *Advances in Sensing with Security Applications*. vol. 2, J. Byrnes and G. Ostheimer, Eds., ed: Springer Netherlands, 2006, pp. 243-268.
[32] P. H. Siegel, "Terahertz technology," *Microwave Theory and Techniques, IEEE Transactions on*, vol. 50, pp. 910-928, 2002.
[33] H. B. Wallace, "Analysis of RF imaging applications at frequencies over 100 GHz," *Applied Optics*, vol. 49, pp. E38-E47, 2010/07/01 2010.
[34] A. Stove, "Potential Applications for Low-Tera-Hetz Radar " presented at the IRS-International Radar Symposium Dresden, Germany, 2015.
[35] R. Appleby and H. B. Wallace, "Standoff Detection of Weapons and Contraband in the 100 GHz to 1 THz Region," *Antennas and Propagation, IEEE Transactions on*, vol. 55, pp. 2944-2956, 2007.
[36] Y. Yihong, M. Mandehgar, and D. R. Grischkowsky, "Broadband THz Signals Propagate Through Dense Fog," *Photonics Technology Letters, IEEE*, vol. 27, pp. 383-386, 2015.
[37] H. Sherry, R. Al Hadi, J. Grzyb, E. Ojefors, A. Cathelin, A. Kaiser, and U. R. Pfeiffer, "Lens-integrated THz imaging arrays in 65nm CMOS technologies," in *Radio Frequency Integrated Circuits Symposium (RFIC), 2011 IEEE*, 2011, pp. 1-4.
[38] F. Friederich, W. von Spiegel, M. Bauer, M. Fanzhen, M. D. Thomson, S. Boppel, A. Lisauskas, B. Hils, V. Krozer, A. Keil, T. Loffler, R. Henneberger, A. K. Huhn, G. Spickermann, P. H. Bolivar, and H. G. Roskos, "THz Active Imaging Systems With Real-Time Capabilities," *Terahertz Science and Technology, IEEE Transactions on*, vol. 1, pp. 183-200, 2011.
[39] B. M. Fischer, H. Helm, and P. U. Jepsen, "Chemical Recognition With Broadband THz Spectroscopy," *Proceedings of the IEEE*, vol. 95, pp. 1592-1604, 2007.

[40] B. E. C. Ruth M Woodward, Vincent P Wallace, Richard J Pye, Donald D Arnone, Edmund H Linfield and Michael Pepper, "Terahertz pulse imaging in reflection geometry of human skin cancer and skin tissue," *Phys. Med. Biol.*, vol. 47, 2002.
[41] M. Rangwala, W. Feinian, and K. Sarabandi, "Study of Millimeter-Wave Radar for Helicopter Assisted-Landing System," *Antennas and Propagation Magazine, IEEE*, vol. 50, pp. 13-25, 2008.
[42] M. Moallem and K. Sarabandi, "Polarimetric Study of MMW Imaging Radars for Indoor Navigation and Mapping," *Antennas and Propagation, IEEE Transactions on*, vol. 62, pp. 500-504, 2014.
[43] D. Jasteh, E. G. Hoare, M. Cherniakov, and M. Gashinova, "Experimental Low-Hz radar image analysis for automotive terrain sensing," *IEEE Geoscience and Remote Sensing Letters*, 2015.
[44] M. Caris, S. Stanko, A. Wahlen, R. Sommer, J. Wilcke, N. Pohl, A. Leuther, and A. Tessmann, "Very high resolution radar at 300 GHz," in *European Radar Conference (EuRAD), 2014 11th*, 2014, pp. 494-496.
[45] J. Dickmann, J. Klappstein, M. Hahn, M. Muntzinger, N. Appenrodt, C. Brenk, and A. Sailer, ""Present research activities and future requirements on automotive radar from a car manufacturer??s point of view"," in *Microwaves for Intelligent Mobility (ICMIM), 2015 IEEE MTT-S International Conference on*, 2015, pp. 1-4.
[46] H. H. Meinel and J. Dickmann, "Automotive Radar: From Its Origins to Future Directions," *Microwave Journal*, vol. 56, pp. 24-+, 2013.
[47] M. Schneider, "Automotive radar–status and trends," in *German microwave conference*, 2005, pp. 144-147.
[48] A. G. Stove, "Obstacle detection radar for cars," *Electronics & Communication Engineering Journal*, vol. 3, pp. 232-240, 1991.
[49] J. Wenger, "Automotive mm-wave radar: status and trends in system design and technology," in *Automotive Radar and Navigation Techniques (Ref. No. 1998/230), IEE Colloquium on*, 1998, pp. 1/1-1/7.
[50] E. Hoare, "Understanding Millimetre-wave Automotive Radar, Theory,Practice and current Developments," University of Birmingham17th- 19th May 1999.
[51] K. L. Fuller. (1974, Solid state radar. *Electronics & Power 20(3)*, 100-101. Available: http://digital-library.theiet.org/content/journals/10.1049/ep.1974.0068
[52] E. G. Hoare and R. Hill, "System requirements for automotive radar antennas," in *Antennas for Automotives (Ref. No. 2000/002), IEE Colloquium on*, 2000, pp. 1/1-111.
[53] G. Kühnle, D.-I. F. H. Mayer, H. Olbrich, W. Steffens, and D.-I. H.-C. Swoboda, "Low-cost long-range radar for future driver assistance systems," *AutoTechnology*, vol. 3, pp. 76-80, 2003.
[54] J. Hasch, "Driving towards 2020: Automotive radar technology trends," in *Microwaves for Intelligent Mobility (ICMIM), 2015 IEEE MTT-S International Conference on*, 2015, pp. 1-4.
[55] E. Musk. (2015). *Tesla 'almost ready' to go driverless*. Available: https://twitter.com/elonmusk?ref_src=twsrc%5Egoogle%7Ctwcamp%5Eserp%7Ctwgr%5Eauthor
[56] U. Franke, D. Pfeiffer, C. Rabe, C. Knoeppel, M. Enzweiler, F. Stein, and R. G. Herrtwich, "Making Bertha See," in *Computer Vision Workshops (ICCVW), 2013 IEEE International Conference on*, 2013, pp. 214-221.
[57] L. Laursen. (2014, 28 May). Google Is Building Its Own Self-Driving Car Prototypes. Available: http://spectrum.ieee.org/cars-that-think/transportation/self-driving/google-is-building-selfdriving-car-prototypes

[58] D. Braid, A. Broggi, and G. Schmiedel, "The TerraMax Autonomous Vehicle concludes the 2005 DARPA Grand Challenge," in *Intelligent Vehicles Symposium, 2006 IEEE*, 2006, pp. 534-539.
[59] C. Urmson, "How a driverless car sees the road," in *TED Talks*, Google, Ed., ed, 2015, p. 15:29.
[60] Delphi. (2015, 31 July). *Delphi Drive: We've reached our destination!* Available: http://www.delphi.com/delphi-drive
[61] G. Mazzaro and F. Koenig, "Introduction to Stepped-Frequency Radar," *US ARMY RDECOM ALC*, vol. 204, 2013.
[62] G. a. S. Gill, "II High-Resolution Step. Frequency Radar," *Ultra-wideband radar technology*, p. 303, 2001.
[63] D. Rytting, "ARFTG 50 year network analyzer history," in *ARFTG Microwave Measurement Conference, 2008 71st*, 2008, pp. 1-8.
[64] D. M. Pozar, *Microwave engineering*: John Wiley & Sons, 2009.
[65] B. R. Phelan, M. A. Ressler, G. J. Mazzaro, K. D. Sherbondy, and R. M. Narayanan, "Design of spectrally versatile forward-looking ground-penetrating radar for detection of concealed targets," in *SPIE Defense, Security, and Sensing*, 2013, pp. 87140B-87140B-10.
[66] H. P. Stern and S. Mahmoud, *Communication systems: analysis and design*: Prentice-Hall, Inc., 2003.
[67] M. Gashinova, V. Djigan, L. Y. Daniel, and M. Cherniakov, "Adaptive calibration in UWB radar," in *Radar Conference, 2008. RADAR '08. IEEE*, 2008, pp. 1-6.
[68] L. Milstein and P. Das, "An Analysis of a Real-Time Transform Domain Filtering Digital Communication System - Part I: Narrow-Band Interference Rejection," *IEEE Transactions on Communications*, vol. 28, pp. 816-824, 1980.
[69] C. A. Balanis, *Antenna theory: analysis and design* vol. 1: John Wiley & Sons, 2005.
[70] "IEEE Standard for Safety Levels with Respect to Human Exposure to Radio Frequency Electromagnetic Fields, 3 kHz to 300 GHz," *IEEE Standard for Safety Levels with Respect to Human Exposure to Radio Frequency Electromagnetic Fields, 3 kHz to 300 GHz*, p. 1.
[71] R. E. Fields, "Evaluating Compliance with FCC Guidelines for Human Exposure to Radiofrequency Electromagnetic Fields," 1997.
[72] *ELVA-1 Millimetre Wave Division*. Available: http://www.elva-1.com/
[73] High Range-Resolution Techniques [Online]. Available: http://www.acfr.usyd.edu.au/pdfs/training/sensorSystems/11%20High%20Range-Resolution%20Techniques.pdf
[74] R. Poisel, *Electronic warfare target location methods*: Artech House, 2012.
[75] K. B. Baltzis, "Calculation of the Half-Power Beamwidths of Pyramidal Horns With Arbitrary Gain and Typical Aperture Phase Error," *Antennas and Wireless Propagation Letters, IEEE*, vol. 9, pp. 612-614, 2010.
[76] M. Q. Qi, W. X. Tang, H. F. Ma, B. C. Pan, Z. Tao, Y. Z. Sun, and T. J. Cui, "Suppressing Side-Lobe Radiations of Horn Antenna by Loading Metamaterial Lens," *Scientific Reports*, vol. 5, p. 9113, 2015.
[77] Y. Huang and K. Boyle, *Antennas: from theory to practice*: John Wiley & Sons, 2008.
[78] D. Jasteh, M. Gashinova, E. G. Hoare, T.-Y. Tran, N. Clarke, and M. Cherniakov, "Low-THz Imaging Radar for Outdoor Applications " presented at the IRS-International Radar Symposium, Dresden, Germany 2015.
[79] R. A. Ross, "Radar cross section of rectangular flat plates as a function of aspect angle," *Antennas and Propagation, IEEE Transactions on*, vol. 14, pp. 329-335, 1966.

[80] A. Bystrov, M. Abbas, E. Hoare, T. Y. Tran, N. Clarke, M. Gashinova, and M. Cherniakov, "Analysis of classification algorithms applied to road surface recognition," in *2015 IEEE Radar Conference (RadarCon)*, 2015, pp. 0907-0911.

[81] F. Norouzian, R. Du, M. Gashinova, E. Hoare, C. Constantinou, M. Lancaster, P. Gardner, and M. Cherniakov, "Signal reduction due to radome contamination in low-THz automotive radar," in *2016 IEEE Radar Conference (RadarConf)*, 2016, pp. 1-4.

[82] S. Palm, R. Sommer, M. Caris, N. Pohl, A. Tessmann, and U. Stilla, "Ultra-high resolution SAR in lower terahertz domain for applications in Mobile Mapping," in *2016 German Microwave Conference (GeMiC)*, 2016, pp. 205-208.

[83] S. Palm, R. Sommer, A. Hommes, N. Pohl, and U. Stilla, "MOBILE MAPPING BY FMCW SYNTHETIC APERTURE RADAR OPERATING AT 300 GHZ," *Int. Arch. Photogramm. Remote Sens. Spatial Inf. Sci.*, vol. XLI-B1, pp. 81-87, 2016.

[84] J. Fortuny-Guasch and J.-M. Chareau, "Radar Cross Section Measurements of Pedestrian Dummies and Humans in the 24/77 GHz Frequency Bands: Establishment of a Reference Library of RCS Signatures of Pedestrian Dummies in the Automotive Radar Bands," 9279282301, 2013.